To the Graduate Council:

I am submitting herewith a dissertation written by Amal Kumar Dutta entitled "Mechanical Properties of Granular Materials Using Nanoindentation and Modeling with Distinct Element Method." I have examined the final electronic copy of this dissertation for form and content and recommend that it be accepted in partial fulfillment of the requirements for the degree of Doctor of Philosophy, with a major in Civil Engineering.

Dayakar Penumadu
Major Professor

We have read this dissertation
and recommend its acceptance:

Eric C. Drumm

George M. Pharr

Roberto S. Benson

Acceptance for the Council:

Anne Mayhew
Vice Chancellor and
Dean of Graduate Studies

(Original signatures are on file with official student record)

MECHANICAL PROPERTIES OF GRANULAR MATERIALS USING NANOINDENTATION AND MODELING WITH DISTINCT ELEMENT METHOD

A Dissertation
Presented for the
Doctor of Philosophy Degree
The University of Tennessee, Knoxville

Amal Kumar Dutta
August 2006

Copyright © 2006 by Amal Kumar Dutta
All rights reserved

DEDICATION

This dissertation is dedicated to my wife Pampa and our son Arpam, since without their support, love, patience, encouragement and sacrifices this work would have not been possible.

This dissertation is also dedicated to my parents whose love and support have made all my endeavors possible.

ACKNOWLEDGEMENT

I want to take this opportunity to express my most sincere respect and gratitude to all the people who helped to make this work possible. First, I want to thank my advisor, Dr. Dayakar Penumadu, for his guidance, wisdom, encouragement and providing me the flexibility throughout the entire research. It has been an honor to be a part of your research group.

I would also like to thank my committee members: Dr. George M. Pharr, Dr. Eric C. Drumm and Dr. Roberto S. Benson. Thank you all for your timely insights and willingness to share in this research.

I would also want to express my gratitude to my wife Pampa and my son Arpam for their patience, love and encouragement through all these time. Without their consistent support and help, earning my Ph.D. degree would not have been possible. I would also like to thank my parents for their faith in me, their support and to help me be the professional that I am now.

I also gratefully acknowledge the SHaRE User Program of Oak Ridge National Laboratory for sponsoring part of my research work. The assistance of Dr. George M. Pharr, Jamie Lamanna, Dr. Andrei Rar, Dr. Shim SangHoon and Erik G. Herbert of MTS Nanoinstrument during the initial design and nanoindentation testing is very much

appreciated. I would also like to acknowledge the involvement and support of Dr. B. Files of NASA/Johnson space center and Dr. Jason.T DeJong, UC, Davis.

I would like to extend my appreciation to my colleagues and friends, Ken Thomas, Dr. Amit Prashant, Dr. Han Lin, Xin Luo, Mathew Kant, Akawut Siriruk, Raghul Gunasekaran, Chandradevi Ulaganathan, Randy Rainwater, Sharon Hale, Dr. Ajanta Sachan, Michael Parham, Alex Davis-Smith, Feng Chen, Indranil Sen, Angie Benson for their help and friendship.

ABSTRACT

The mechanics of granular material is an important issue that governs many geotechnical engineering applications. Two types of particles having similar particle size, but different shape are used in this research to evaluate the role of particle morphology on the physical properties of its assemblage. Experimentation of 1-D compression behavior at constant axial strain rate under laterally confined conditions is performed for these two particulate materials and the behavior of the stress path is analyzed in relation to the initial material packing and physical characteristics of the granules.

The behavior of granular assemblages under imposed loading conditions are also evaluated by analyzing the macro and micro level morphological changes (in terms of shape and size distribution) resulting from 1-D compression tests. Various experimental procedures and techniques are employed for characterizing the size and shape aspect of these particles. The mechanical properties (hardness, modulus, and time dependent creep parameters) of the individual particles are determined and analyzed using nanoindentation technique. Nanoindentation has emerged recently as a powerful tool for precise measurements of mechanical properties of materials. Considering its potential applicability in the broad area of micromechanics associated with granular materials, an in-depth study of its application is performed. Since a rigorous study of the nanoindentation technique for finite size particles has not been done to date, initial testing for developing appropriate experimental and interpretation procedures required testing reference material such as fused quartz and novel composite materials to gain additional insight and experience. For this reason, besides granular materials, the changes in

mechanical properties for structured materials (blended single wall carbon nanotube-epoxy composite specimens) are also included in this research

The micromechanical analysis of granular assembly using computer simulation through the program PFC^{2D} (2-Dimensional Particle Flow Code), an application of Distinct Element Method (DEM) is also performed. The material micro-properties such as particle shear stiffness and normal stiffness values are assigned from the nanoindentation test results for the two granular materials. The particle contact behavior, nature of force chain structure, and uniformity of deformation associated with 1-D compression on granular materials having different shape and mechanical properties are analyzed.

TECHNICAL ABSTRACT

The mechanics of granular material is an important issue that governs many geotechnical engineering applications. The principal governing factors that control the behavior of such granular media are grain size and shape, morphology, mechanical properties of individual particles, the inter particle force distribution, micro-structure of material assemblage, nature of contacts during initial deposition, and its evolution under imposed loading conditions. Two types of particles having similar particle size, but different shape are used in this research to evaluate the role of particle morphology on the physical properties of its assemblage. Experimentation of 1-D compression behavior at constant axial strain rate under laterally confined conditions is performed for these two particulate materials and the behavior of the stress path is analyzed in relation to the initial material packing and physical characteristics of the granules.

The behavior of granular assemblages under imposed loading conditions are also evaluated by analyzing the macro and micro level morphological changes (in terms of shape and size distribution) resulting from 1-D compression tests. Various experimental procedures and techniques are employed for characterizing the size and shape aspect of these particles. The mechanical properties (hardness, modulus, and time dependent creep parameters) of the individual particles are determined and analyzed using nanoindentation technique. Nanoindentation has emerged recently as a powerful tool for precise measurements of mechanical properties of materials. It has the potential to play a significant role in elucidating the mechanisms associated with many particulate mechanics issues of relevance to geotechnical engineering. Considering its potential

applicability in the broad area of micromechanics associated with granular materials, an in-depth study of its application is performed in this research. Since a rigorous study of the nanoindentation technique for finite size particles has not been done to date, initial testing for developing appropriate experimental and interpretation procedures required testing reference material such as fused quartz and novel composite materials to gain additional insight and experience. For this reason, besides granular materials, the changes in mechanical properties for structured materials (blended single wall carbon nanotube-epoxy composite specimens) are also included in this research

The micromechanical analysis of granular assembly using computer simulation through the program PFC^{2D} (2-Dimensional Particle Flow Code), an application of Distinct Element Method (DEM) is also performed. The material micro-properties such as particle shear stiffness and normal stiffness values are assigned from the nanoindentation test results for the two granular materials. The particle contact behavior, nature of force chain structure, and uniformity of deformation associated with 1-D compression on granular materials having different shape and mechanical properties are analyzed. The goal of the distinct element method is not to match the macroscopic experimental response, but use fundamental properties of particles to predict the behavior of its assembly, and evaluate basic mechanisms contributing to the strength and deformation behavior of particulate system.

TABLE OF CONTENTS

PART 1. INTRODUCTION 1

INTRODUCTION 2

REFERENCES 8

PART 2. THEORY AND BACKGROUND 12

MEASUREMENT OF HARDNESS AND ELASTIC MODULUS USING DEPTH SENSING NANOINDENTATION 13

PARTICLE FLOW CODE (PFC2D) USING DISTINCT ELEMENT METHOD(DEM) 21

REFERENCES 27

PART 3. EVOLUTION OF PARTICLE MORPHOLOGY DURING 1-D LOADING INDUCED CRUSHING OF SANDS 29

ABSTRACT 30

INTRODUCTION 31

RESEARCH SCOPE 33

MORPHOLOGICAL ANALYSIS TECHNIQUES 35

RESULTS AND DISCUSSION 41

CONCLUSION 60

REFERENCES 62

PART 4. MECHANICAL PROPERTIES OF BLENDED SINGLE WALL CARBON NANOTUBE COMPOSITES 65

ABSTRACT 66

INTRODUCTION 67

EXPERIMENTAL 69

RESULTS AND DISCUSSION 71

CONCLUSION 78

REFERENCES 79

PART 5. NANOINDENTATION TESTING FOR EVALUATING MODULUS AND HARDNESS OF SINGLE-WALLED CARBON NANOTUBE REINFORCED EPOXY COMPOSITES 82

ABSTRACT 83

INTRODUCTION 84

SPECIMEN PREPARATION PROCEDURE 86

EXPERIMENTAL PROCEDURE AND RESULTS 87

CREEP BEHAVIOR OF NANOTUBE-REINFORCED EPOXY COMPOSITES 94

SUMMARY AND CONCLUSIONS 100

REFERENCES 101

PART 6. MECHANICAL BEHAVIOR OF INDIVIDUAL SAND PARTICLES USING NANOINDENTATION AND THE EFFECT OF STRESS LEVEL 104

ABSTRACT 105
INTRODUCTION 106
MATERIALS AND EXPERIMENTAL METHODS 107
RESULTS AND DISCUSSION 114
CREEP BEHAVIOR OF OTTAWA AND Q-ROK SAND PARTICLES 123
SUMMARY AND CONCLUSION 138
REFERENCES 139

PART 7. EVOLUTION OF MICROMECHANICS ASSOCIATED WITH 1-D GRANULAR COMPRESSION USING DISTINCT ELEMENT METHOD 147
ABSTRACT 148
INTRODUCTION 149
CALIBRATION OF NUMERICAL CODE AND PARTICLE PARAMETERS 151
RESULTS AND DISCUSSION 166
CONCLUSION 181
REFERENCES 183

PART 8. CONCLUSION AND FUTURE RESEARCH 186
CONCLUSION 187
FUTURE RESEARCH 192

Vita 194

LIST OF TABLES

Table 3.1 Summary of number based and volume based mean diameter and standard deviation based on three repeatability tests by FPIA and laser diffraction on Ottawa and Q-Rok sand finer particles (particle diameter below 75 μm through dry sieve) at intermediate and higher stress 56

Table 3.2 Summary of shape analysis (circularity based) by image processing through FPIA on Ottawa and Q-Rok sand finer particles (particle diameter below 75 μm through dry sieve) at intermediate and higher stress 59

Table 5.1 Results from tensile test data 88

Table 6.1 Summary of Sand Properties 109

Table 6.2 Mean modulus and hardness results from indentation test 121

Table 7.1 Summary of Ottawa sand properties 154

APPENDICES

Appendix 6A U.S. Silica Product data sheet for Ottawa sand 145

Appendix 6B U.S. Silica Product data sheet for Q-Rok sand 146

LIST OF FIGURES

Figure 2.1 Schematic of the Nanoindenter 14

Figure 2.2 Schematic diagram showing contact depth and total depth of indentation.....14

Figure 2.3 Schematic representation of indentation load (*P*) against displacement (*h*) for one cycle of loading and unloading 16

Figure 2.4 Continuous stiffness measurement (CSM) technique – imposing a small dynamic oscillation on the primary loading signal.....19

Figure 2.5 Schematic of nanoindentation system with each component representing the simple harmonic oscillator model.....19

Figure 2.6 Calculation cycle in PFC^{2D}.....23

Figure 2.7 Schematic representation showing (a) ball-ball contact and (b) ball-wall contact 24

Figure 3.1 Plot of volumetric strain and void ratio versus vertical stress response for Ottawa sand loaded to 55 and 100 MPa and Q-Rok sand loaded to 20 and 100 MPa. All specimens prepared at an initial relative density of 65% 35

Figure 3.2 Comparison of size distribution of Q-Rok and Ottawa sand at different applied stress using sieve analysis.....42

Figure 3.3 Comparison of particle shape analysis (roundness based) of (a) Ottawa sand and (b) Q-Rok sand samples at zero stress and 100 MPa stress. 44

Figure 3.4 SEM images for Ottawa and Q-Rok sand particles at different stress 45

Figure 3.5 Distribution for finer particles (below 75μm based on sieve analysis) of Ottawa 100 and 55 MPa samples by digital image analysis using FPIA (a) plot showing number based percent frequency against size (b) number based cumulative

under percent against size (c) volume based percent frequency against size and (d) volume based cumulative under percent against size. 47

Figure 3.6 Distribution for finer particles (below 75µm based on sieve analysis) of Q-Rok sample at stress level 100MPa and 20 MPa by digital image analysis using FPIA (a) plot showing number based percent frequency against size (b) number based cumulative under percent against size (c) volume based percent frequency against size and (d) volume based cumulative under percent against size. 48

Figure 3.7 Plot showing circularity of particles (below 75µm based on sieve analysis) at different applied stresses by digital image analysis using FPIA for (a) Ottawa sand and (b) Q-Rok sand samples 49

Figure 3.8 Comparative grain size distribution for Ottawa sand and Q-Rok sand at 100MPa applied stress for particle sizes below 75µm (based on sieve analysis) analyzed by digital image analysis using FPIA (a) number based percent frequency against size (b) number based cumulative under percent against size (c) volume based percent frequency against size (d) volume based cumulative under percent against size and (e) circularity plot. 51

Figure 3.9 Typical images of Ottawa sand and Q-Rok sand particles as observed using FPIA (a) Ottawa 100 MPa; size range: 10 – 20µm (b) Ottawa 55 MPa; size range: 10 – 20µm (c) Ottawa 100 MPa; size range: 5 – 10µm (d) Ottawa 55 MPa; size range: 5 – 10µm (e) Q-Rok 100 MPa; size range: 10 – 20µm (f) Q-Rok 20 MPa; size range: 10 – 20µm (g) Q-Rok100 MPa; size range: 5 – 10µm (h) Q-Rok 20 MPa; size range: 5 – 10µm 52

Figure 3.10 Comparative grain size distribution for Ottawa sand at different applied stress for finer particles (diameter <75μm through sieve) analyzed through laser diffraction (a) volume based percent frequency against size (b) number based percent frequency against size (c) volume based cumulative under percent against size (d) number based cumulative under percent against size 54
Figure 3.11 Comparative grain size distribution for Q-Rok sand at different applied stress for finer particles (diameter <75μm through sieve) analyzed through laser diffraction (a) volume based percent frequency against size (b) number based percent frequency against size (c) volume based cumulative under percent against size (d) number based cumulative under percent against size 55
Figure 3.12 Comparative grain size distribution analysis for Ottawa and Q-Rok sand finer particles (diameter <75μm through sieve) at 100 MPa stress analyzed through laser diffraction (a) volume based and (b) number based 56
Figure 4.1 Compression Mold 70
Figure 4.2 Dog Bone Specimens 70
Figure 4.3 Data from Tensile Tests 72
Figure 4.4 Load-Displacement relationship used for Nano-Indentation.....73
Figure 4.5 Modulus versus Depth of Indentation for varying SWCNT content and loading rate) 74
Figure 4.6 Modulus increase with increasing SWCNT content 75
Figure 4.7 SEM images of 5%SWCNT composite (a) small magnification, (b) large magnification.....76

Figure 5.1 Load versus deformation for 1% by weight SWNT-reinforced epoxy composites 90
Figure 5.2 Effect of increasing carbon nanotube content on the load versus deformation behavior (mean values from 10 indents) 90
Figure 5.3 Effect of increasing carbon nanotube content on mean modulus values with depth of indentation.....91
Figure 5.4 Effect of increasing SWNT content on mean hardness values with depth of indentation 93
Figure 5.5 Typical indent shape in epoxy specimen showing minimal pile-up or sink-in. 93
Figure 5.6 Results from indentation creep tests showing the influence of increasing SWNT on time-dependent deformation properties.....97
Figure 5.7 Variation of creep displacement under constant load of 50 mN indicates the improvement in time-dependent deformation properties with increasing SWNT.....97
Figure 5.8 Variation of indentation strain rate with hardness for increasing carbon nanotube content 98
Figure 5.9 SEM images on the broken (by tensile force) surface of 0.5% SWNT composite 99
Figure 6.1 SAMPL-KUP Mounting Cups 109
Figure 6.2 SEM image of (a) sub-rounded Ottawa sand and (b) sub-angular Q-Rok sand before applied stress 111
Figure 6.3 Typical sample specimen for nanoindentation on sand particles 111

Figure 6.4 SEM image of (a) sub-rounded Ottawa sand and (b) sub-angular Q-Rok sand subjected to 100 MPa stress after final polishing 113
Figure 6.5 Load versus deformation for (a) unstressed Ottawa sand particles and (b) unstressed Q-Rok sand particles 115
Figure 6.6 (a) Load versus deformation and (b) Elastic modulus versus deformation for fused silica 116
Figure 6.7 Mean modulus with depth of indentation for Ottawa and Q-Rok sand particles subjected to 100 MPa stress 116
Figure 6.8 Mean hardness with depth of indentation for Ottawa and Q-Rok sand particles subjected to 100 MPa stress 117
Figure 6.9 Mean modulus with depth of indentation for unstressed and 100 MPa stressed Ottawa and Q-Rok sand particles 118
Figure 6.10 Mean hardness with depth of indentation for unstressed and 100 MPa stressed Ottawa and Q-Rok sand particles 118
Figure 6.11 SEM image of typical indentation shape in sand specimen showing minimal pile-up or sink-in 123
Figure 6.12 Plot showing load versus time for the creep experiment 124
Figure 6.13 Results from indentation creep tests showing the influence of stress on time dependent deformation properties for (a) Ottawa sand unstressed and 100 MPa stressed particle along with fused silica (b) QRok sand unstressed and 100 MPa stressed particle along with fused silica 125

Figure 6.14 The repeatability results of three tests performed on Q-Rok 100 MPa stressed particles (a) Load versus displacement response and (b) Displacement versus time response for the load hold segment of three tests 127
Figure 6.15 Variation of creep displacement during load hold segment for unstressed and stressed (100 MPa) Ottawa and Q-Rok sand, and fused silica 127
Figure 6.16 Variation of indentation strain rate with hardness (a) Ottawa sand unstressed, (b) Ottawa sand subjected to 100 MPa , (c) unstressed Q-Rok sand, (d) Q-Rok sand subjected to 100 MPa and (e) amorphous fused silica 130
Figure 6.17 (a) Experimental and fitted creep curves for Ottawa unstressed particle, and (b) corresponding log strain rate versus log stress plot 132
Figure 6.18 (a) Experimental and fitted creep curves for Ottawa sand particle subjected to 100MPa vertical stress, and (b) corresponding log strain rate versus log stress plot 132
Figure 6.19 (a) Experimental and fitted creep curves for Q-Rok unstressed particle, and (b) corresponding log strain rate versus log stress plot 133
Figure 6.20 (a) Experimental and fitted creep curves for Q-Rok sand particle subjected to 100MPa vertical stress, and (b) corresponding log strain rate versus log stress plot 133
Figure 6.21 (a) Experimental and fitted creep curves for fused quartz, and (b) corresponding log strain rate versus log stress plot 134
Figure 6.22 Variation of creep stress exponent with error bars for Ottawa and Q-Rok sand unstressed and 100 MPa of stress particles.....136

Figure 6.23 Variation of log (strain rate) versus log (stress) for fused silica and Ottawa and Q-Rok sand unstressed and 100 MPa stressed particle.....137
Figure 6.24 Variation of indentation strain rate versus time for fused silica and Ottawa and Q-Rok sand unstressed and 100 MPa stressed particles 137
Figure 7.1 Photograph of the 19 mm diameter specimen cell 152
Figure 7.2 (a) Photograph of the MTS 858 Table Top System with the Series 359 Axial-Torsional Load Unit, (b) photograph of the enlarged view of the specimen cell....152
Figure 7.3 SEM image of Ottawa sand particles 154
Figure 7.4 Schematic diagram of two particle clump with aspect ratio 1.25 157
Figure 7.5 Schematic diagram showing a disc and a two ball clump (aspect ratio 1.25) with same area 159
Figure 7.6 Comparison of numerical data with experimental results on Ottawa sand at loose packing state (with equivalent porosity of 37.13%). For numerical analysis Ottawa sand was represented using a 2-ball-clump logic with aspect ratio of 1.25. 167
Figure 7.7 Plot showing stress-strain behavior for three repeatability tests performed on Ottawa sand (porosity, n_i = 37.13%) using specimen dimension 19 mm by 19 mm with load applied through MTS 858 under deformation control.....168
Figure 7.8 Behavior of contact force distribution for 2-ball clump (aspect ratio 1.25) particle assembly at loose state (PFC^{2D} porosity 22%) with different applied stress level; (a) 5 MPa stress, (b) 9 MPa stress, (c) 25 MPa stress, (d) 50 MPa stress, (e) 75 MPa stress and (f) 100 MPa stress.....170

Figure 7.9 Comparison of numerical data with experimental results on Ottawa sand at dense packing state (with equivalent porosity of 35.66%). For numerical analysis Ottawa sand was represented by 2-ball-clump particle assembly with particle aspect ratio 1.25 171

Figure 7.10 Behavior of contact force distribution for 2-ball clump (aspect ratio 1.25) particle assembly at Dense state (PFC^{2D} porosity 20%) with different applied stress level; (a) 1 MPa stress, (b) 5 MPa stress, (c) 25 MPa stress, (d) 50 MPa stress, (e) 75 MPa stress and (f) 100 MPa stress.....173

Figure 7.11 Variation of average coordination number at different applied vertical stress level for the loose and dense assembly of the clump particles with particle aspect ratio of 1.25.....175

Figure 7.12 Variation of Stress-Strain distribution through numerical analysis on a (a) dense and (b) a comparatively loose particle assembly with particle aspect ratios of 1.0, 1.25 and 1.50.....177

Figure 7.13 Variation of average coordination number at different applied vertical stress level for the loose and dense assembly with (a) circular particle (aspect ratio of 1.0), (b) particle aspect ratio of 1.25 and (c) particle aspect ratio of 1.50 179

Figure 7.14 Variation of average coordination number at dense and loose state of circular particle assembly (Particle aspect ratio 1.00) at the applied vertical stress of 5MPa and 75MPa. The error bars shown here incorporates the ±0.05% porosity variation around the respective dense and loose state of assembly 180

PART 1: INTRODUCTION

INTRODUCTION

There are many geotechnical engineering situations where high stresses may occur in granular materials such as pile end bearing, high earth or rock fill dams, or foundations of offshore gravity structures. These high stresses can lead to particle breakage for even the strongest minerals. Thus, for the consideration of wider range of geotechnical situations, it is of utmost importance to quantify and analyze the nature of particle force distribution for evaluating the mechanical response such as crushing, reorientation and settlement. Many factors can affect the amount of particle crushing in soil aggregates [1–3]. The amount of particle crushing is affected by the stress level, its magnitude as well as the past stress history. The grain size and shape also have an important bearing on the force transfer at particle scale, since particle size and shape determines granular assembly. The reason being, bigger particles may arrange differently and contain defects/flaws, having higher probability for breaking. Similarly, increasing angularity increases the particle crushing as the stress concentration along their narrow dimension causes asperity breakage. Moreover, the arrangement of granules in an aggregate by way of its nature of compaction and contacts between particles also governs the force structures within the assembly.

Researchers have studied the granular assembly and analyzed the particle crushing in relation to the primary specimen conditions such as the particle properties, applied stress level, void ratio, initial grain size distribution, shape etc. Several criteria and methods have been proposed by various researchers [2, 4–7] to quantify the amount and extent of particle crushing during loading. In all of the past studies, the nature of

particle breakage was evaluated by quantifying the changes between pre and post test grain size distribution. Thus, proper characterization of particle size distribution is of paramount importance from the view point of many geotechnical engineering situations. The classical method for measuring grain size distribution is by sieving. However, measuring grain size distribution through traditional sieve analysis can provide information on macro scale (up to a scale of 200mesh ~ 75 micron) and very little information is available on particle information at micro level. Further, the normal sieve analysis only gives a rough measure of the width of particles and does not provide relevant data for good characterization. Moreover, particle morphology has an indirect but important effect on particle size measurement and thus measuring and quantifying the shape aspect of particles should be considered while characterizing the particles. The recent advances in instrumentation and technologies are filling the need for improved particle size and shape characterization methods. Over the past ten years, the field of particle size distribution characterization and measurements experienced a renaissance in many fields of engineering where researchers [8-13] utilized different new procedures/techniques like image processing, static and dynamic light scattering, laser diffraction, 3D-laser scanning etc. to characterize and analyze the particle shape and size distribution. In this research, one of our goals is to perform several careful investigations on the particle crushing and characterization of size and shape of particles both pre and post test at macro and micro level using different techniques.

To understand the true behavior of granular material in an assembly, it is also very important to accurately measure the mechanical properties including hardness,

elastic modulus and creep behavior at the particle level. However, due to the lack of proper instrumentation available until recently, there was no such study in the published literature where the mechanical properties at the particle level have been measured accurately and implemented for use in modeling and analysis of behavior of granular material. During the last decade, there was a revolutionary development in the field of depth-sensing nanoindentation technique, by which mechanical properties of small volumes of material can now be determined accurately. In this technique, an indenter probe of appropriate geometry is placed in contact with the sample surface and then pushed into it. The resistance to indentation and the indent depth are continuously monitored throughout the experiment, and by analyzing the load-displacement curve, both hardness and elastic modulus of the material can be measured directly and more precisely. Nanoindentation technique is now an accepted and proven technique for mechanical characterization of micro and nanoscale materials in a wide variety of disciplines [14-23]. A detail description of the theory and background of nanoindentation technique is presented in Part 2 of this dissertation. In this research, an extensive study is performed to analyze the characteristics of the mechanical properties like hardness, modulus and time dependent creep properties of different types of materials using depth sensing nanoindentation instrumentation technique. Instrumented indentation testing used to evaluate the mechanical properties of individual grains of different mineralogy and morphology (viz. Ottawa, Qrok sand etc). Considering this new technique of instrumented nanoindentation has tremendous potentiality in its application in many cases of geotechnical engineering material characterization and analysis, an in depth study of this technique and its applicability is also investigated through this research. For this

purpose, besides the individual granular particles, the same technique also applied extensively to characterize and evaluate the changes in mechanical properties of a structured material, e.g. blended single wall carbon nanotube-epoxy composite specimens.

The behavior of granular media is of fundamental importance related to many problems in geotechnical engineering. Traditionally, numerical methods, such as finite element or finite difference methods are commonly used to model and assess the response of granular materials under an imposed load or changed boundary conditions. These are continuum methods, where the granular packing close to mechanical equilibrium are modeled with elastoplastic constitutive laws [24, 25], i.e. incremental stress-strain relations. However, such laws, despite their practical success, were never clearly related to grain level mechanics. Nowadays, it is well established that a better understanding of such granular material behavior may be achieved by a micromechanical analysis using distinct-element method (DEM) introduced by Cundall and Strack [26-29]. The DEM keeps track of the motion of individual particles and updates contacts with neighboring elements by using a constitutive contact law. In this research, the micromechanics associated with 1-D compression on granular materials with different shape and material properties, is simulated and analyzed by the two dimensional discontinuum program PFC^{2D} [30]. The PFC^{2D} is a program developed by Itasca consulting Group, Inc. by using the concept of distinct element method and the theory behind this coding is presented in Part 2.

The primary objectives of this dissertation are as follows:

I. Evaluating the nature of particle crushing by characterizing macro and micro scale analysis of particle shape and size distribution using various techniques:

(a) digital image analysis using Particle Shape Distribution Analyzer (PSDA)

(b) Imaging Analysis - Flow Particle Imaging Analyzer (FPIA),

(c) Laser Diffraction (Mastersizer S, Malvern Instruments Ltd.)

II. Measurement of Hardness and elastic modulus using depth sensing nanoindentation on

(a) Different types of silica sand samples (e.g. Q-Rok and Ottawa sand) and

(b) Hybrid composite material made with varying percentage of single walled carbon nanotube (SWCNT) – reinforced epoxy composites.

III. Study of time dependent creep effect on the different sand samples at particle level and on SWCNT – reinforced epoxy composites.

IV. Simulation and analysis as applied to the micromechanical behavior associated with 1-D compression on granular materials with different shape, using distinct element method.

In Part 3, characterization of particles at both the macro and micro levels has been performed using several techniques/processes. The crushed particles generated from two different granular types (Q-Rok and Ottawa sand) subjected to high-stress levels in 1-D

compression testing has been analyzed in terms of the particle morphology, shape and size distribution. Part 4 and 5 presents the extensive application of instrumented nanoindentation technique to characterize and evaluate the changes in mechanical properties of a structured material, e.g. blended single wall carbon nanotube-epoxy composite specimens. The improvement/variation in mechanical properties such as hardness and elastic modulus of blended nanocomposites prepared using a low-viscosity, liquid epoxy resin and purified single-wall carbon nanotubes (SWCNTs) was evaluated and the macroscopic tensile stress–strain behavior for hybrid materials made with varying amounts of SWCNT was determined. Time dependent creep properties for these nanocomposites were also evaluated. In Part 6, the mechanical properties of Ottawa and Q-Rok sand at particle level were studied using instrumented nanoindentation, and the effect of mechanical property changes due to the application of 100 MPa of confined compressive stress were analyzed. This research explored nanoindentation technique for measuring the mechanical properties of micrometer-sized individual particles and introduced appropriate experimental and interpretation procedure as well as sample preparation technique. Part 7 presents compressibility in confined compression for an assemblage of particles with specified initial state of packing, and the novel use of non-continuum based distinct element method for modeling the mechanical behavior of granular material. For simulation purposes, the actual particle level mechanical properties (hardness, stiffness and modulus) as obtained from the nanoindentation technique were used.

REFERENCES

1. Hardin, B.O., *"Crushing of soil particles"*, J. of Geotec.Engrg., ASCE, 1985, 111(10), 1177-1192.
2. Lee, K.L. and Farhoomand, I., *"Compressibility and crushing of granular soils in anisotropic triaxial compression"*, Can. Geotech. J., Ottawa, Canada, 1967, 4(1), 68-86.
3. Lo, K.Y. and Roy,M., *"Response of particulate materials at high pressures"*, Soils and found.,Tokyo, Japan, 1973, 13(1), 1-14.
4. Marsal, R.J., *"Large scale testing of rockfill materials"*, J. of Soil Mech. and Found. Div., ASCE, 1967, 93(2), 27-43.
5. Leslie, D.D., *"Large scale triaxial tests on gravelly soils"*, Proc. of the 2nd Pananerican conf. on soil mech. and found. Engr., 1963, 1, 183-202.
6. Leslie, D.D., *"Shear strength of rockfill"*, Physical properties engineering study No. 526, US Army Corps of Engineering, 1975, 124.
7. Lade, P.V.; Yamamuro, J. A.; Bopp, P. A., *"Significance of particle crushing in granular materials"*, J. of Geotechnical Engineering, 1996, April, 309-316.
8. Lanaro, F.; Tolppanen, P., *"3D characterization of coarse aggregates"*, Engineering Geology, 2002, 65, 17–30.
9. Provder, T., *"Challenges in particle size distribution measurement past, present and for the 21st century"*, Progress in Organic Coatings, 1997, 32, 143-153.
10. Xu, R. ; Guida, O. A. D., *"Comparison of sizing small particles using different technologies"*, Powder Technology, 2003, 132, 145 – 153.

11. Pons, M.N.; Vivier, H.; Belaroui, K.; Bernard, M. B.; Cordier, F.; Oulhana, D.; Dodds, J.A., *"Particle morphology: from visualisation to measurement"*, Powder Technology, 1999, 103, 44–57.

12. Pellegrin, D. V. D.; Stachowiak, G. W., *"Assessing the role of particle shape and scale in abrasion using 'sharpness analysis'Part I. Technique development"*, Wear, 2002, 253, 1016–1025.

13. Zhang, P.-C.; Liu, J.; Chew, C.H.; Gan, L.M.; Li, S.F.Y., *"AFM imaging and characterization of latex particles formed by copolymerization of styrene and poly(ethylene oxide) macromonomer"*, Talanta, 1998, 45, 767–773.

14. Camerucci, M.A.; Urretavizcaya, G.; and Cavalieri, A.L., "*Mechanical behavior of cordierite and cordierite-mullite materials evaluated by indentation techniques"*, J. of the Euro. Ceramic Soc., 2001, 21, 1195-1204.

15. Ahn, H; Klimek, K.S.; Rie, K.T., "*BCN coatings by RF PACVD at low temperature",*. Surf. and Coat. Technol., 2003, 174-175, 1225-1228.

16. Mencík, J.; Munz, D.; Quandt, E.; Weppelmann, E. R.; Swain, M., "*Determination of elastic modulus of thin layers using nanoindentation"*, J. of Mate. Res., 1997, 12(9), 2475-2484.

17. Lim,Y. Y.; Chaudhri, M. M., "*The effect of the indenter load on the nanohardness of uctile metals: an experimental study on polycrystalline work-hardened and annealed oxygen-free copper"*, Philosophical Magazine A, 1999, 79(12), 2979 - 3000.

18. Tsui, T. Y.; Pharr, G. M., *"Substrate effects on nanoindentation mechanical property measurement of soft films on hard substrates"*, J. of Mater. Res., 1999, 14(1), 292-301.

19. Saha, R.; Nix, W.D., *"Effects of the substrate on the determination of thin film mechanical properties by nanoindentation"*, Acta Mater, 2002, 50(1), 23-38.

20. Hayes, S.A.; Goruppa, A.A.; and Jones, F.R., *"Dynamic nanoindentation as a tool for the examination of polymer materials"*, J. Mater. Res., 2004, 19(11), 3298-3306.

21. Wang, W. and Lu, K., *"Nanoindentation measurement of hardness and modulus anisotropy in Ni3Al single crystals"*, J. Mater. Res., 2002, 17(9), 2314-2320.

22. Vriend, N. M. and Kren, A.P., *"Determination of the viscoelastic properties of elastomeric materials by the dynamic indentation method", P*olymer testing, 2004, 23, 369-375.

23. Schuh, C.A. and Nieh, T.G., *"A survey of instrumented indentation studies on metallic glasses"*, J. Mater. Res., 2004, 19(1), 46-57.

24. Herrmann, H.J.; Hovi, J.-P.; and Luding, S., *"Physics of dry granular media"*, 1998, Balkema, Dordrecht.

25. Wood, D.M., "*Soil behaviour and critical state soil mechanics*", 1990, Cambridge University, Cambridge, England.

26. Cundall, P.A. and Strack, O.D.L., *"The development of constitutive laws for soil using the distinct element method"*, Numerical methods in geomechanics, 1979, 1, 289-317.

27. Cundall, P.A. and Strack, O.D.L., *"A discrete numerical model for granular assemblies"*, Geotechnique, 1979, 29, 47-65.

28. Cundall, P.A., "*Formation of a three-dimentional distinct element model-part I.A scheme to detect and represent contacts in a system composed of many polyhedral blocks"*, Int. J. Rock Mech. Min. Sci. Geomech Abstr, 1988, 25(3), 107-116.

29. Hart, R.; Cundall, P.A.; Lemos, J., "*Formulation of a three-dimentional distinct element model-Part II. Mechanical calculations for motion and interaction of a system composed of many polyhedral blocks"*, Int. J. Rock Mech. Min. Sci. Geomech Abstr, 1988, 25(3), 117-125.

30. Itasca Consulting Group Inc. PFC2D (Particle flow code in 2 dimension), Version 3.1, Minneapolis, MN, 2004.

PART 2: THEORY AND BACKGROUND

MEASUREMENT OF HARDNESS AND ELASTIC MODULUS USING DEPTH SENSING NANOINDENTATION

The depth sensing indentation instrument principally consists of three basic components consisting of an indenter of specific geometry, a force actuator, and a displacement sensor as shown in Figure 2.1. It consists of an indenter of specific geometry that is mounted on a rigid column through which the force is transmitted. For present testing, a Berkovich indenter (a three-sided pyramid) [1] was used. The force is imposed on the indenter by passing current through a coil that sits within a circular magnet. The indenter displacement is measured by the voltage difference of the capacitive plate arrangement of the displacement sensing system as shown in Figure 2.1. The plate-and-indenter assembly is supported by two leaf springs that are designed to have very low stiffness in the vertical direction and very high stiffness in horizontal directions.

The theoretical force and displacement resolution of the system is 50 nN and <0.01 nm respectively. The material hardness (H) and the elastic modulus (E) are two important mechanical properties most frequently measured with depth sensing indentation technique. A schematic of the indentation process is shown in Figure 2.2. As the indenter head is pushed into the sample material, both elastic and plastic deformations occur that results in the formation of a hardness impression conforming to the shape of the indenter to some contact depth h_c. Once the indenter is withdrawn, only the elastic portion of the displacement is recovered and it is this recovery that allows one to determine the elastic properties of a material.

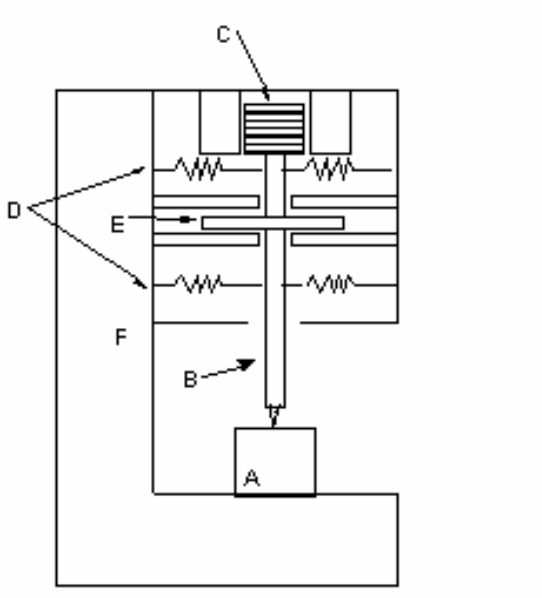

Figure 2.1: Schematic of the Nanoindenter: (A) Sample; (B) Indenter Column; (C) Load Application Coil; (D) Indenter Support Spring; (E) Capacitive Displacement Gauge; (F) Load Frame.

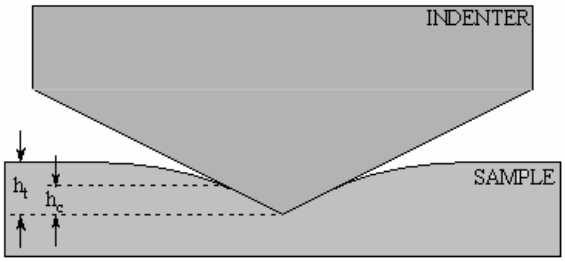

Figure 2.2: Schematic diagram showing contact depth and total depth of indentation.

Figure 2.3 shows typical representation of indentation load (P) versus displacement (h) for one cycle of loading and unloading. Here, P_{max}, h_{max} and h_f represent the peak load, peak displacement and residual depth after unloading respectively. $S = dP/dh$ is the slope of the initial portion of the unloading curve and represents the elastic stiffness of the contact and is called the contact stiffness.

Hardness is defined as shown in Equation 2.1.

$$H = \frac{P}{A} \tag{2.1}$$

Where, P is the applied load and A is the projected contact area at that load. The elastic modulus (E) of the sample is determined from the reduced modulus E_r which is defined by the Equation 2.2 below as per Oliver-Pharr method [2].

$$E_r = \frac{\left(\sqrt{\pi}.S\right)}{2\beta\sqrt{A}} \tag{2.2}$$

Here, β is a constant that depends on the indenter geometry. For a Berkovich indenter, β = 1.034 [3]. The elastic modulus (E) of the test material is then calculated by using Equation 2.3.

$$\frac{1}{E_r} = \frac{\left(1-\nu^2\right)}{E} + \frac{\left(1-\nu_i^2\right)}{E_i} \tag{2.3}$$

Where, ν is the Poisson's ratio of the material being tested, E_i and ν_i are the elastic modulus and Poisson's ratio, respectively of the indenter. For present testing with diamond indenter, the value of E_i is 1,141GPa and ν_i is 0.07 [2, 4].

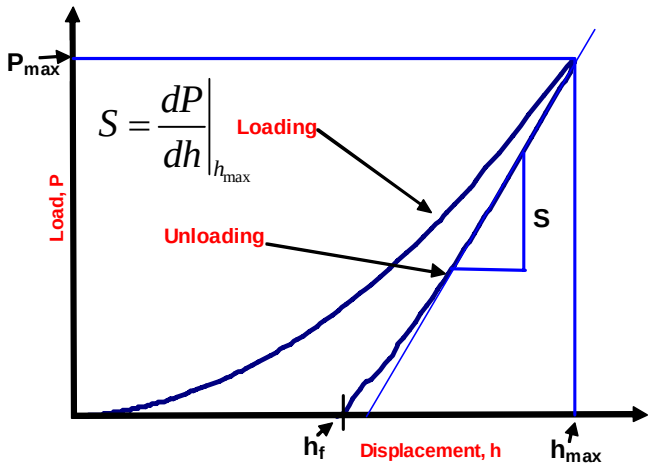

Figure 2.3: Schematic representation of indentation load (*P*) against displacement (*h*) for one cycle of loading and unloading.

It is observed from Equations 2.1 and 2.2 that for precise calculation of hardness and modulus, it is important to calculate the contact stiffness (*S*) and projected contact area (*A*) under load very accurately. According to Oliver and Pharr [2], the data analysis procedure begins by fitting the load-displacement data acquired during unload to the power-law relation as shown in Equation 2.4.

$$P = BA\left(h - h_f\right)^m \tag{2.4}$$

Here, P is the applied load, h is resulting displacement, B and m are empirically determined parameters, and h_f is the displacement after complete unloading. Using the result from the analytical differentiation of Equation 2.4, the unloading stiffness is estimated by evaluating at the maximum depth of penetration, $h = h_{max}$ as below:

$$S = \left(\frac{dP}{dh}\right)_{h=h_{\max}} = Bm\left(h_{\max} - h_f\right)^{m-1} \tag{2.5}$$

However, as stated by Oliver and Pharr, Equation 2.5 does not always provide adequate description of the entire unloading curve and thus it is a prudent practice to determine contact stiffness by fitting only the upper portion of the unloading data.

The contact depth h_c which is generally different from the total penetration depth is calculated using Equation 2.6.

$$h_c = h_{\max} - \varepsilon \frac{P_{\max}}{S} \tag{2.6}$$

Where, ε is a constant which depends on the indenter geometry, and for Berkovich indenter its empirical value is 0.75.

The projected contact area (A) is calculated by evaluating an empirically determined area function at the contact depth h_c, such that

$$A = f(h_c) \tag{2.7}$$

A general form of area function is

$$A = \sum_{n=0}^{8} C_n \left(h_c\right)^{2-n} \tag{2.8}$$

Here, $C_0 \ldots\ldots C_8$ are the constants determined by using a curve fitting procedure [5, 6]. The tip function for the ideal Berkovich tip is

$$A = 24.56 h_c^2 \tag{2.9}$$

Traditionally, the measurement of stiffness (S) is determined from the unloading slope of the load-displacement data as defined before, and in such calculation, it only allows one to determine S (as well as E and H) at the maximum penetration depth.

An important alternative is to use continuous stiffness measurement (CSM) technique, in which stiffness is measured continuously during the loading of the indenter by imposing a small dynamic oscillation on the primary loading signal (Figure 2.4) and analyzing the resulting response of the system by means of a frequency-specific amplifier [2, 6-8].

In CSM option with continuous measurement of stiffness, one can obtain hardness and elastic modulus values as a continuous function of the surface penetration depth, and not just at the point of initial unload. In the nanoindenter system, all the motion is restricted to one dimension so that it can be modeled by a simple harmonic oscillator as shown in Figure 2.5. Here, the force summation on the indenter mass can be represented by the ordinary differential Equation 2.10.

$$m\ddot{z} + D\dot{z} + Kz = F(t) \tag{2.10}$$

Where, K is an equivalent stiffness that includes the stiffness at the contact (S), the load frame stiffness(K_f) and support spring stiffness (K_s), such that

$$K = \left(S^{-1} + K_f^{-1}\right)^{-1} + K_s \tag{2.11}$$

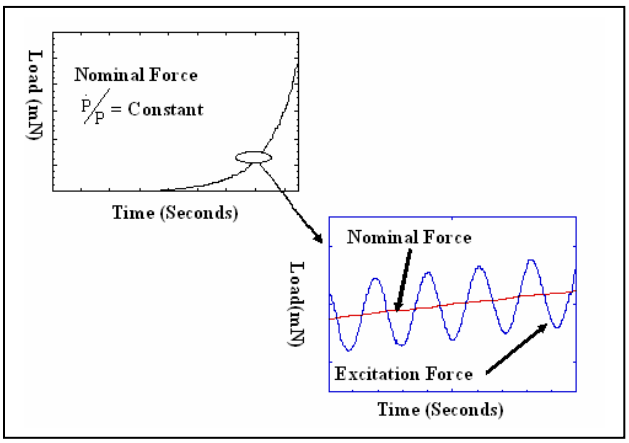

Figure 2.4: Continuous stiffness measurement (CSM) technique – imposing a small dynamic oscillation on the primary loading signal.

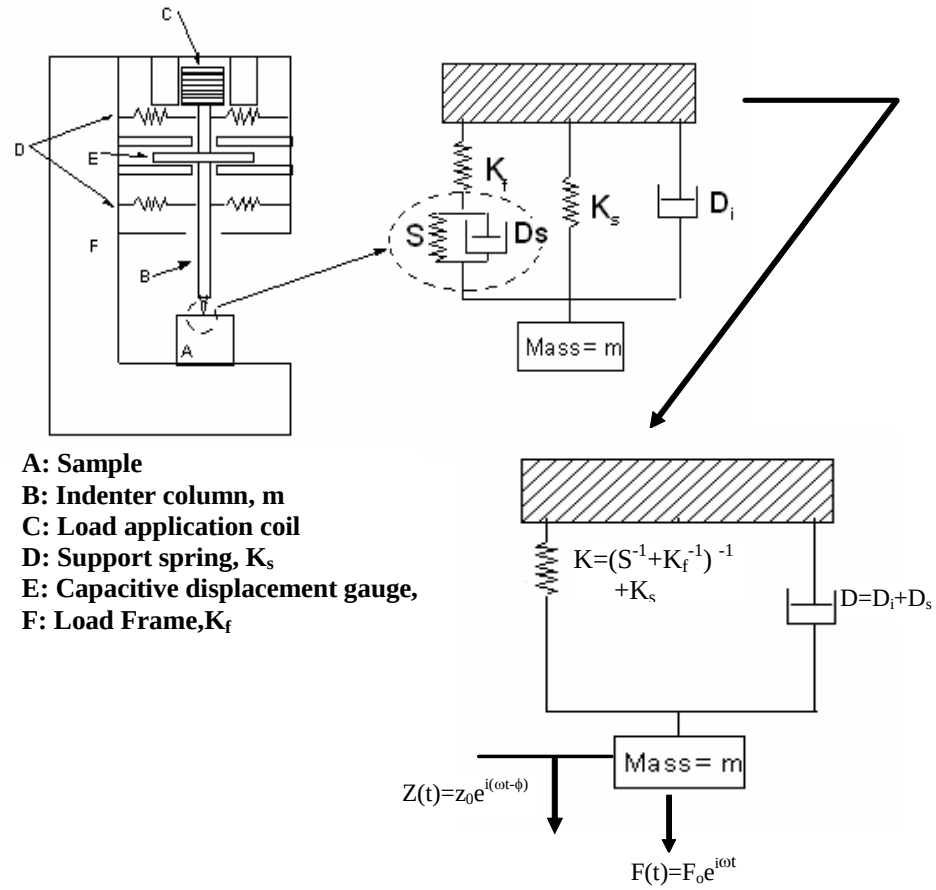

A: Sample
B: Indenter column, m
C: Load application coil
D: Support spring, K_s
E: Capacitive displacement gauge,
F: Load Frame,K_f

Figure 2.5: Schematic of nanoindentation system with each component representing the simple harmonic oscillator model.

D is an equivalent dashpot for damping in the indenter head and in the sample, i.e.

$$D = D_i + D_s \tag{2.12}$$

For a force function of the form of Equation 2.13, the resulting displacement can be expressed by Equation 2.14. Equation 2.14 also defines that the displacement oscillates at the same frequency (ω) as the force, but lags by a phase angle, ϕ.

$$F(t) = F_0 e^{i\omega t} \tag{2.13}$$

$$z(t) = z_0 e^{i(\omega t - \phi)} \tag{2.14}$$

On substitution of Equation 2.14 into Equation 2.10 gives

$$\left|\frac{F_0}{z_0}\right| = \sqrt{\left(K - m\omega^2\right)^2 + \left(\omega D\right)^2} \tag{2.15}$$

and

$$\tan\phi = \frac{\omega D}{K - m\omega^2}. \tag{2.16}$$

Finally, by solving Equations 2.15 and 2.16, the stiffness of the contact is calculated as

$$S = \left[\frac{1}{\frac{F_0}{z_0}\cos\phi - \left(K_s - m\omega^2\right)} - \frac{1}{K_f}\right]^{-1}. \tag{2.17}$$

Here, in CSM option, we set the excitation frequency,ω, and measure the excitation amplitude (F_0), displacement amplitude (z_0) and phase angle (ϕ). The contact stiffness is then calculated based on the Equation 2.17 with known machine parameters K_f, m, *and* K_s. Once the stiffness is measured, the hardness and elastic modulus are then calculated as a continuous function of penetration depth using equations as defined before.

PARTICLE FLOW CODE (PFC^{2D}) USING DISTINCT ELEMENT METHOD (DEM)

Traditionally, finite-element or finite-difference methods are commonly used in geo-mechanics to model the responses of granular media. In these methods, the material is idealized as a continuum that obeys some constitutive (stress-strain) relationship. However, an appropriate stress-strain law for granular material to realistically model the macroscopic assemblage behavior does not exist, and the existing formulations are often plagued by the complexity with many obscure model parameters without the ability to quantitatively describe them in a rational framework. Moreover, granular material behaves in complicated ways for specialized loading conditions such as liquefaction commonly observed in loose sands under dynamic loading conditions, and it is necessary to model such behavior accurately. This mechanism, and many others, depends on the particulate nature of sand, the packing of grains as well as the nature of contacts formed in an assembly. It is recently proposed that a better understanding of such granular media may be achieved by replacing continuum methods with distinct element or discrete particle based approach. With these recently evolving non-continuum methods, assemblies of discrete particles appear to capture the complicated behavior under realistic loading conditions with simple assumptions and few parameters to describe constitutive behavior between two particles or between a particle and a boundary at the element level. The distinct element method (DEM) as described by Cundall and Strack [9-12] is a particular implementation of such discrete-element methods that allow finite displacements and rotations of discrete bodies, including complete detachment, and recognize new contacts automatically as the calculation progresses. Through the coding

in PFC^{2D}, which is developed on the concept of distinct element method (DEM), the movement and interaction of circular particles can be modeled.

In PFC^{2D}, the particles are assumed to be circular rigid bodies and their mechanical interaction is characterized by using the so-called soft-contact approach. In this approach, although the particles are assumed as rigid bodies for the purpose of shape definition, elastic deformation is allowed to take place at the contacts. In addition to circular particles, referred as “balls” or “discs”, the PFC^{2D} also includes “walls”. Walls allow one to apply velocity boundary conditions to assemblies of balls for the purposes of compaction and confinement. The balls/discs and walls interact with one another via the forces that arise at contacts. In PFC^{2D}, though the particles are considered as circular, the arbitrary shaped particles can be generated either by bonding together several particles or by using its clump logic.

The calculations performed in the DEM alternate between the application of Newton’s second law to the particles and a force-displacement law at the contacts (Figure 2.6). Newton’s second law is used to determine the motion of each particle arising from the contact and body forces acting upon it, while the force-displacement law is used to update the contact forces arising from the relative motion at each contact. Contacts, which may exist between two balls or between a ball and a wall, are formed and broken automatically during the course of a simulation.

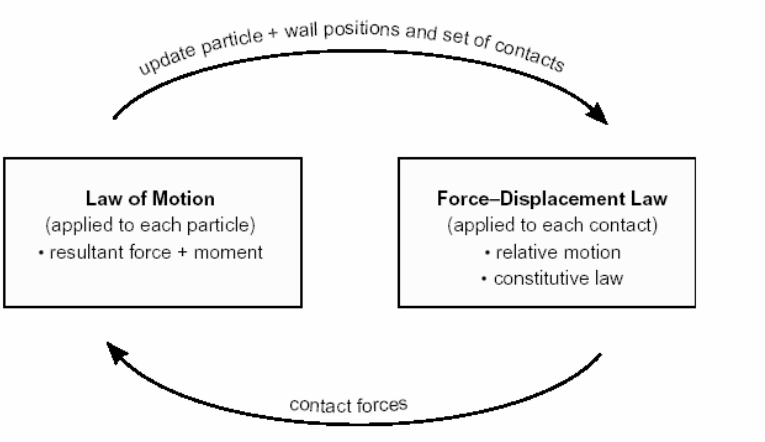

Figure 2.6: Calculation cycle in PFC^{2D}

The equations of motion are satisfied for each ball. The presence of walls in PFC^{2D} requires only that the force-displacement law account for ball-wall contacts. Newton's second law is not applied to walls, since the wall motion is specified by the user and remains constant regardless of the contact forces acting upon it. Also, contacts may not form between two walls. Thus, contacts are either ball-ball or ball-wall.

The force-displacement law operates at a contact and can be described in terms of a contact point, $x_i^{[C]}$, lying on a contact plane that is defined by a unit normal vector, n_i. Here, n_i lies in the plane of the PFC^{2D} model and the contact point is within the interpenetration volume of the two entities. For ball-ball contact (Figure 2.7a), the normal vector is directed along the line between ball centers. For ball-wall contact (Figure 2.7b),

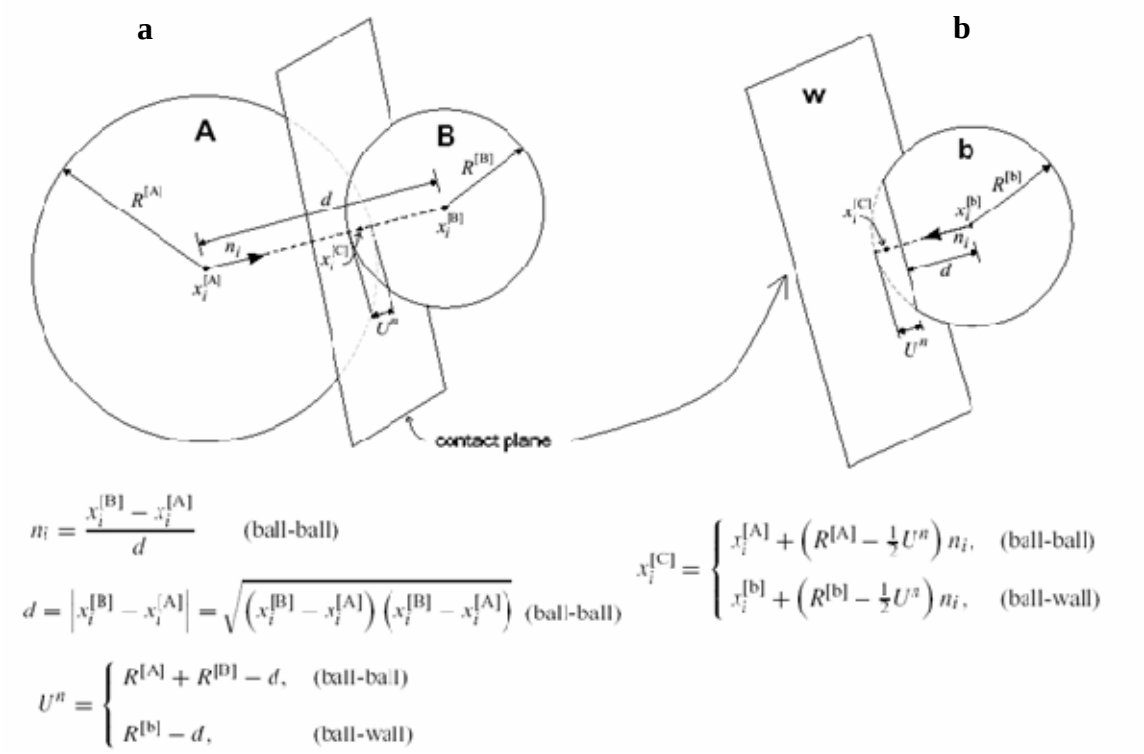

Figure 2.7: Schematic representation showing (a) ball-ball contact and (b) ball-wall contact.

the normal vector is directed along the line defining the shortest distance between the ball center and the wall. The contact force (F_i) is decomposed into a normal component (F_i^n)acting in the direction of the normal vector and a shear component (F_i^s) acting in the contact plane.

The shear component also lies in the plane of the PFC^{2D} model.

$$F_i = F_i^n + F_i^s \tag{2.18}$$

The magnitude of the normal contact force is calculated by

$$F^n = K^n U^n, \tag{2.19}$$

where, U^n is the overlap and K^n is the normal stiffness [force/displacement] given by

$$K^n = \frac{k_n^{(A)} k_n^{(B)}}{k_n^{(A)} + k_n^{(B)}}, \tag{2.20}$$

with $k_n^{(A)}$ and $k_n^{(B)}$ being the particle normal stiffness.

The shear force is computed in an incremental fashion such that

$$\Delta F^s = -k^s \Delta U^s. \tag{2.21}$$

When the contact is formed, F^s is initialized to zero and each subsequent relative shear-displacement increment, ΔU^s, produces an increment of elastic shear force ΔF^s, that is added to F^s (after F^s has been rotated to account for motion of the contact plane).

Here, k^s is the contact shear stiffness given by

$$k^s = \frac{k_s^{(A)} k_s^{(B)}}{k_s^{(A)} + k_s^{(B)}}. \tag{2.22}$$

The constitutive contact law used for simulation in this research consists of two parts: the stiffness model – providing a linear elastic relation between contact force and contact relative displacement in normal and shear directions as shown above- and a slip model – which is defined by the friction coefficient (μ) at the contact, where μ is taken to be the minimum friction coefficient of the two contacting entities. For the slip model, the criterion of no-normal strength is enforced by checking whether the overlap (U^n) is less than or equal to zero. If it is, then both the normal and shear contact forces are set to zero. The contact is checked for slip conditions by calculating the maximum allowable shear contact force

$$F_{\max}^s = \mu \left| F_i^n \right|. \tag{2.23}$$

If $\left| F_i^s \right| > F_{\max}^s$, then slip is allowed by setting the magnitude of F_i^s equal to $F_{\max}^s$ via

$$F_i^s \leftarrow F_i^s \left(F_{\max}^s \Big/ \left| F_i^s \right| \right). \tag{2.24}$$

In DEM, the particles interaction is treated as a dynamic process with states of equilibrium developing whenever the internal forces balance. By tracing the movements of the individual particles, the contact forces and displacements of a stressed assembly of particles are determined. Movements result from the propagation through the particle system of disturbances caused by specified wall and particle motion and/or body forces.

In PFC^{2D}, the dynamic behavior is represented numerically by an explicit time-stepping algorithm by using a central-difference scheme to integrate accelerations and velocities. The central idea in DEM is that the timestep chosen to be so small that, during a single timestep, disturbances produced can not propagate from any further than its immediate neighbors. Thereby, at all times, the forces acting on any particle are determined exclusively by its interaction with the neighboring particles that are in contact.

REFERENCES

1. Hay, J.L.; Pharr, G.M., *"Instrumented Indentation Testing"*, ASM Handbook 8(ASM International, OH, 2000), 232-243.
2. Oliver, W.C.; Pharr, G.M., *"An improved technique for determining hardness and elastic modulus using load and displacement sensing indentation experiments"*, J. Mater. Res., June, 1992, 7(6), 1564-1583.
3. King, R.B., *"Elastic analysis of some punch problems for a layered medium"*. Int. J. Solids Struct., 1987, 23, 1657-1664.
4. Simmons, G.; Wang, H., *"Single crystal elastic constants and calculated aggregate properties", A handbook, 2nd edition, The M.I.T. Press*, 1971.
5. Oliver, W.C.; Pharr, G.M., *"Measurement of hardness and elastic modulus by instrumented indentation: Advances in understanding and refinement to methodology"*, J. Mater. Res., 2004, 19(1), 3-20.
6. Pharr, G.M.; Oliver, W.C.; Brotzen, F.R., *"On the Generality of the Relationship. among Contact Stiffness, Contact Area, and. Elastic Modulus"*, J. Mater. Res., 1992, 7(3), 613-617.

7. Pethica, J.B.; Oliver, W.C., *"Tip Surface Interaction in STM and AFM"*, Phys. Scr., 1987, 19, 61.

8. Pethica, J.B.; Oliver, W.C., *"Mechanical Properties of Nanometer volumes of Material: Use of the Elastic Response of Small Area Indentations, in Thin Films-Stress and Mechanical Properties"*, MRS Symp. Proc. (Materials Research Society), 1989, 130, 13-23.

9. Cundall, P.A. and Strack, O.D.L., *"The development of constitutive laws for soil using the Distinct Element Method*", Proceedings of the ICONMIG, 1979, 1, 289-298.

10. Cundall, P.A. and Strack, O.D.L., *"A discrete numerical model for granular assemblies"*, Geotechnique, 1979, 29, 47-65.

11. Cundall, P.A., *"Formation of a three-dimentional distinct element model-part I.A scheme to detect and represent contacts in a system composed of many polyhedral blocks"*, Int. J. Rock Mech. Min. Sci. Geomech Abstr, 1988, 25(3), 107-116.

12. Hart, R.; Cundall, P.A.; Lemos, J., *"Formulation of a three-dimentional distinct element model-Part II. Mechanical calculations for motion and interaction of a system composed of many polyhedral blocks"*, Int. J. Rock Mech. Min. Sci. Geomech Abstr, 1988, 25(3), 117-125.

PART 3: EVOLUTION OF PARTICLE MORPHOLOGY DURING 1-D LOADING INDUCED CRUSHING OF SANDS

This part is a slightly revised version of a paper with the same title submitted in the journal Granular Matter in 2006 by Amal K. Dutta, Dayakar Penumadu and Jason T. DeJong:

A. K. Dutta, D. Penumadu and Jason T. Dejong. "*Evolution of Particle Morphology during 1-D Loading Induced Crushing of Sands*," Granular Matter, 2006.

My primary contributions to this paper include (1) selection of the topic and development of the problem into a work relevant to my doctoral research study, (2) development of experimental setup, (3) most of the gathering and interpretation of literature, (4) performing the laboratory experiments, (5) interpretation and analysis of test results, (6) most of the writing.

ABSTRACT

Particle crushing of granular material is one of the most important phenomena that governs the engineering mechanical properties and behavior of soil. In this research, the crushed particles generated from two different granular types (Q-Rok and Ottawa sand) subjected to high-stress levels in 1-D compression testing has been analyzed in terms of the particle morphology, shape and size distribution. Using several techniques/processes, characterization of particles at both the macro and micro levels has been performed. The macro level grain size distribution by sieve analysis shows that at same stress level Q-Rok samples are subjected to more crushing than Ottawa samples. The macro level shape characterization analyzed with the Particle Shape Distribution Analyzer (PSDA) indicates that there is an increase in roundness for both types of

crushed aggregates with increasing stress level. The micro level analysis for the particles below 75 μm has been performed by digital image analysis using a Flow Particle Imaging Analyzer (FPIA) as well as by a laser light scattering technique. At the micro level it is shown that the particles are developing more angularity with increasing applied stress for both types of aggregates and that Ottawa sand produces a higher volume fraction of finer particles compared to Q-Rok sand under similar imposed stress levels. It is concluded that particle shape plays significant role in breakage behavior of granular materials.

Keywords: Particle size distribution, Shape characterization, Digital image analysis, Particle Shape Distribution Analyzer, Laser light scattering, Flow Particle Imaging analyzer, 1-D compression, sand crushing

INTRODUCTION

There are many geotechnical engineering situations where high stresses may occur in granular materials, such as pile end bearing, high earth or rock fill dams, or foundation of offshore gravity structures. These high stresses can lead to particle breakage for even the strongest minerals. Thus, for the consideration of wider range of geotechnical situations, it is important to quantify and analyze the relationship between the stress distribution at the particle level and the mechanical response (e.g. crushing, reorientation, settlement). Many factors can influence the amount of particle crushing in granular soils [1–3]. The amount of particle crushing is affected by the stress level, its magnitude as well as the past stress history. The grain size and shape also have an important bearing on the force transfer at particle scale, since particle size and shape

determines the granular assembly formation. The reason being, bigger particles may arrange differently and contain defects/flaws, having higher probability for breaking. Similarly, increasing angularity increases the particle crushing as the stress concentration along their narrow dimension causes asperity breakage. Moreover, the arrangement of granules due to the nature of compaction and contacts between particles also governs the force structures within the assembly.

Researchers have studied the granular assembly and analyzed the particle crushing in relation to the primary specimen conditions such as the particle properties, applied stress level, void ratio, initial grain size distribution, shape, etc. Several criteria and methods have been proposed by various researchers [2, 4–7] to quantify the amount and extent of particle crushing during loading. The primary parameter used for evaluating the particle breakage is quantifying the changes between pre and post test grain size distribution. Thus, proper characterization of particle size distribution is of paramount importance from the view point of many geotechnical engineering situations. The classical method for measuring grain size distribution is by sieving. However, while measuring grain size distribution through traditional sieve analysis can provide information on the macro scale (defined herein as down to a scale of ~ 75 micron corresponding to #200 sieve) and minimal information is available on particle information at the micro level (defined herein as particles nominally less than 75 μm and passing #200 sieve). Further, the conventional mechanical sieve analysis only provides an approximate measure of the particle width and does not provide rigorous data for detailed particle characterization. Moreover, particle morphology has an indirect but important

effect on particle size measurement and thus measuring and quantifying the shape aspect of particles should be considered while characterizing the particles.

Recent advances in instrumentation and technologies providing new opportunities for improved particle size and shape characterization. Over the past ten years, the field of particle size distribution characterization and measurements experienced a renaissance where researchers [8-13] utilized innovative procedures/techniques such as image processing, static and dynamic light scattering, laser diffraction, 3D-laser scanning, etc. to characterize and analyze the particle shape and size distribution. In our present work, we enumerate the results of several careful investigations on the particle crushing and characterization of size and shape of particles both at macro and micro level using different techniques/ systems.

RESEARCH SCOPE

The research herein focuses on examining the morphological evolution of two sands subjected to 1-D compression stresses of up to 100 MPa. Three specimens per sand were selected for examination from a study examining the influence of particle properties (hardness, shape) and initial specimen state (void ratio, relative density, porosity) on one-dimensional compression and hydraulic conductivity [14 -15]. A 63.5 mm diameter and 20 mm height stress oedometer was used in a stress-controlled mode for all tests. The two sands selected were Ottawa 20-30 (G_s = 2.64, D_{50} = 0.74 mm, C_u = 1.06, C_c = 1.16, e_{min} = 0.51, e_{max} = 0.74, single particle fracture strength = 125.5 MPa, Mohs scratch hardness = 6-7) and Q-Rok (G_s = 2.65, D_{50} = 0.75 mm, C_u = 1.47, C_c = 1.40,

e_{min} = 0.80, e_{max} = 1.14, single particle fracture strength = 57.1 MPa, Mohs scratch hardness = 6-7). These sands were selected due to substantial differences in particle angularity, particle hardness, and specimen behavior specifically with respect to crushing. Figure 3.1 presents the exhibited stress versus displacement of two samples of each sand prepared via air pluviation to a relative density of 65% and subjected to different stress levels. The deformation behavior differs notably. For Ottawa sand a near elastic response upon initial loading continues to a stress level over 40 MPa at which point behavior becomes distinctly non-linear. A similar, but less defined behavior is exhibited for Q-Rok, with transition to non-linear behavior begins at about 10 MPa and continues to higher stress levels. The Q-Rok sand undergoes nearly 32% volumetric strain while Ottawa undergoes about 18% when subjected to 100 MPa, corresponding to changes in void ratio of about 0.6 and 0.3, respectively.

The three specimens selected for each sand for analysis herein includes one specimen subjected to 100 MPa stress, one specimen subjected to a stress slightly higher than the stress level at which non-linear response becomes evident (55 MPa for Ottawa, 20 MPa for Q-Rok), and one specimen of untested sand representing the virgin (0 MPa) condition. It is noted that prior to testing both sand batches were pre-sieved and all material passing the #50 sieve (< 0.5 mm) was removed. As a result, no micro scale (< 75 μm) data is presented herein for the untested 0 MPa condition for each sand type.

The suite of six specimens enabled analysis of particle morphology during 1-D compression. The intermediate stress specimens (i.e. 55 MPa for Ottawa and 20 MPa for

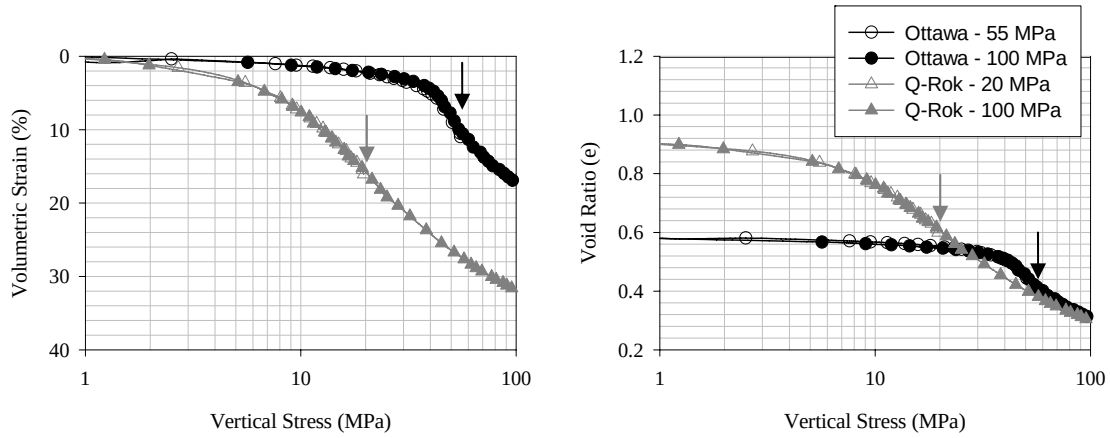

Figure 3.1: Plot of volumetric strain and void ratio versus vertical stress response for Ottawa sand loaded to 55 and 100 MPa and Q-Rok sand loaded to 20 and 100 MPa. All specimens prepared at an initial relative density of 65%.

Q-Rok) provide some insight into the stress range over which a majority of particle morphology occurs. As discussed subsequently, the study by DeJong et al. [15] was primarily limited to crushing assessment based on mechanical grain size analysis and limited image analysis of individual large particles.

The research herein presents the initial findings on the analysis of the particle morphology of the evolution of the macro (> 75 μm) as well as the micro scale (< 75 μm) particles. It is noted that to the authors knowledge no previous research on the characteristics of the fines content due to sand crushing has been performed.

MORPHOLOGICAL ANALYSIS TECHNIQUES

Various experimental procedures and techniques including Particle Shape Distribution analyzer (PSDA), Laser light scattering by Malvern Mastersizer S, image

processing through Flow Particle Imaging Analyzer (FPIA-2100), and Sieve Analysis has been used for analyzing the grain size distribution and shape characteristics. Macro level analysis was performed using dry sieve technique and particle shape characteristics were analyzed using image analysis through PSDA. Analysis of finer particles (particles nominally < 75 μm from passing #200 sieve) generated due to the applied stress of 55 and 100 MPa on Ottawa sand and 20 and 100 MPa on Q-Rok samples were performed by using image analysis through FPIA and laser light scattering through Malvern Mastersizer S.

Particle shape analysis using Particle Shape Distribution Analyzer (PSDA):

Using a digital imaging analysis technique, an automated Particle Shape Distribution Analyzer (PSDA) has been developed recently by the second author to evaluate both the particle shape and its distribution [16]. In PSDA, the particulate material is allowed to fall from a horizontal vibratory feeder in front of a remotely regulated DC lighting system, and by using a progressive scan CCD camera consecutive progressive scan digital images are captured using a high speed PCI-based frame grabber (Flash Bus MV Pro). The particle shape analysis from these 2-D images are then evaluated by using custom developed software which uses a multiple-document interface using Visual Basic, Windows API, and Image Pro Plus. Using the image processing algorithm of the software, the particles are segmented from the background and the geometric characteristics of the particles are processed and analyzed. For analysis purposes, the projected area, feret (min), feret (max), perimeter, and the roundness of each particle are obtained from these images. Feret (min) and feret (max) are the shortest

and longest caliper (feret) length, respectively, of the particle and are measured through Image Pro Plus.

A shape classification algorithm that is universally applicable must characterize the particle shape in a dimensionless manner. The PSDA utilizes roundness to classify the shape of every counted particle, defined as:

$$Roundness = \frac{P^2}{4\pi A} \tag{3.1}$$

where P is the perimeter and A is the projected area on the image plane. The PSDA system used in this study provided shape measurements for dry sand with particle sizes larger than 50 μm.

Digital image analysis using Flow Particle Imaging Analyzer (FPIA):

Flow Particle Imaging Analyzer (FPIA-2100) combines sheath flow concepts and image processing technology for characterizing particles in a slurry state for a size range of 1.5 μm to 160 μm. In this system, an aspirated suspension of particles is guided through a transparent flow cell to form a sheath flow, and a strobe back light is used to instantaneously illuminate moving particles to enable image capture. The sheath flow provides very uniform planar flow so that most images of particles are captured in focus. For every 1/30 second, a strobe light is used to illuminate the slurry sample through the flow cell for two microsecond duration, allowing the particles to be captured as a still digital image. Images of the particles are captured using a monochromatic camera and are processed in the image-processing unit. In the image-processing unit, the edge of each

particle observed is extracted for calculation of the projected area and circumference of the particle. Each particle image is stored on a square image slightly larger than the particle size, sorted according to the size of the particles, and stored in the image memory for further processing.

Three testing modes can be used with this testing system: HPF (high magnification), LPF (low magnification) and HPF-LPF (combining both high and low magnification). The particle diameter measurement for range HPF is 1.5 – 40 μm, LPF is 10 – 160 μm and for HPF-LPF is 1.5 – 160 μm.

The particle distribution is analyzed using the projected area and circumference of each particle. A circle having the same area as the projected area of the particle is assumed, and its diameter is calculated. Depending on the requirements, both the volume based and number based particle size distribution analysis can be performed through this system.

For the FPIA testing system used in this research, the maximum equivalent particle diameter is 160μm due to the type of optics used and the 250μm screen used to filter slurry with solid particles. However, the system uses a larger diameter range of 0.6 – 400 μm for plotting purposes and is divided into 226 bins to calculate frequency distribution. The larger size of 400 microns is to facilitate systems with different optics. However, due to limitations of sheath flow with increasing particle size beyond 160

microns, authors decided to characterize particles in the optimum range. To measure number based distribution, the number of particles (f_{0i}) whose circular diameter d_i are within the range of d_l to d_{l+1} is calculated, whereas for volume based distribution measurement, the overall volume of particles (f_{3i}) whose circular diameter d_i are within the range of d_l to d_{l+1} is calculated. An equivalent sphere is assumed for the volume calculation. For number based calculation, the ratio of the number of particles with circular diameters of d_i or smaller to the total number of particles is calculated to generate cumulative number frequency data. For the volume based analysis, the ratio of the volume of particles with circular diameter of d_i or smaller to the weight of the total particles is calculated to generate cumulative volume frequency data. The average diameter is calculated for number based and volume based distribution by using the following respective equations:

$$\bar{d}_0 = \frac{\sum \left(d_i \; X \; f_{0i} \right)}{\sum f_{0i}} \tag{3.2}$$

$$\bar{d}_3 = \frac{\sum \left(d_i \; X \; f_{3i} \right)}{\sum f_{3i}} \tag{3.3}$$

where, $\bar{d}_0$ is the number based average diameter, d_i is the diameter of particle of a particular size range and f_{0i} is the number based frequency of that size rage. Similarly, $\bar{d}_3$ is the volume based average diameter and f_{3i} is the volume based frequency of that size rage.

Through FPIA, the particle shape is defined by circularity, where, the circularity of the particle is measured using Equation 3.4. Regardless of the actual value, the system assumed the circularity to be always 0.4 or larger. From the equation it is clear that the smaller the circularity, the higher the irregularity in the particle shape with a resultant higher particle angularity.

$$\text{Circularity} = \frac{\text{Circumference of a circle having the same projected area as the particle}}{\text{Circumference of the projected area of the particle}} \leq 1 \quad (3.4)$$

Particle size and shape analysis using Laser Diffraction (Malvern Mastersizer S)

The particle size distribution for particles below 75μm of Ottawa sand and Q-Rok sand samples were also analyzed by commercially available system Malvern Mastersizer S, which operates on laser light scattering technique. In this system, a representative cloud or 'ensemble' of particles passes through a broadened beam of laser light that scatters the incident light onto a Fourier lens. This lens focuses the scattered light onto a detector array and, using an inversion algorithm, a particle size distribution is inferred from the collected scattered light data [17]. Using laser light scattering technique in Malvern Mastersizer S, the mean equivalent volume based diameter of particles is measured. However, in this system, the volume based size distribution can be converted to different distribution types such as number, surface, and length based distribution using:

$$X_i = \frac{100 V_i / d_i^n}{\sum V_i / d_i^n} \tag{3.5}$$

where, X_i is the transformed percentage distribution, V_i is the volume distribution result, d_i is the mean size of class i and n is the required distribution type: 1 for surface, 2 for length and 3 for number based results.

This system can measure the distribution analysis both in dry and wet form for particles. For this research the wet process with de-ionized water as the dispersant medium was used. The Malvern Mastersizer S was configured with the 300RF lens that can measure particle size ranges 0.05μm to 880 μm for this research.

RESULTS AND DISCUSSION

Macro Particle Analysis:

The grain size distribution of Q-Rok and Ottawa sand samples untested (0 MPa), at the intermediate stress level (i.e. 55 MPa, 20 MPa), and at 100 MPa using the conventional dry sieve method is presented in Figure 3.2. It may be concluded from the curves that the gradations shift toward a more well-graded condition as the applied stress increases. It is also evident that with applied intermediate and higher vertical stress, sub-angular Q-Rok sand produces higher percentage of finer particle for all size ranges as compared to the sub-rounded Ottawa sand. This implies that Q-Rok sand undergoes more particle breakage relative to Ottawa sand. As described elsewhere [15], this is due to a combined effect of particle properties (namely particle asperties and angularity) and

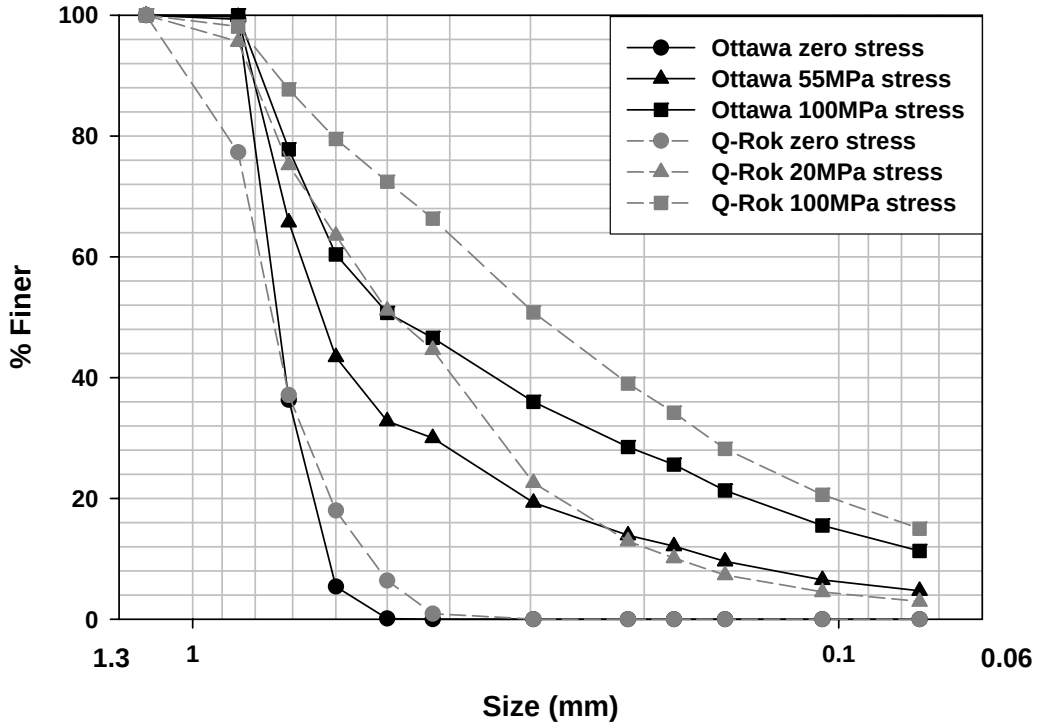

Figure 3.2: Comparison of size distribution of Q-Rok and Ottawa sand at different applied stress using sieve analysis.

specimen conditions (namely low coordination number resulting in increased stress per particle-particle contact).

The roundness based particle shape histogram for both types of sand samples at zero vertical stress and at 100 MPa vertical stress is illustrated in Figure 3.3. From Equation 3.1, it is noticed that a perfect circle will return a roundness value of 1.0, all other shapes will return values > 1.0. Here, from the shape plots it is clear that increasing stress increases the roundness of the particles (> 50 micron size) for both Ottawa and Q-Rok sand samples. The shape analysis also reveals that at 0 MPa condition 70% of Ottawa sand particles have roundness values within the range 1.0 to 1.55, whereas Q-Rok sand particles account for 66% over the same roundness range. At 100 MPa the roundness of Ottawa and Q-Rok sand particles increases by 25% and 32%, respectively, for the roundness range between 1.0 and 1.55.

Representative SEM (Scanning Electron Microscope) images of Ottawa and Q-Rok sand particle with different size ranges at various stress levels are presented in Figure 3.4. The sub-rounded nature of Ottawa sand and sub-angular shape of Q-Rok sand particles at 0 MPa stress and the morphological features of crushed particles (finer fraction) as a result of different applied stress levels are clearly evident from the images.

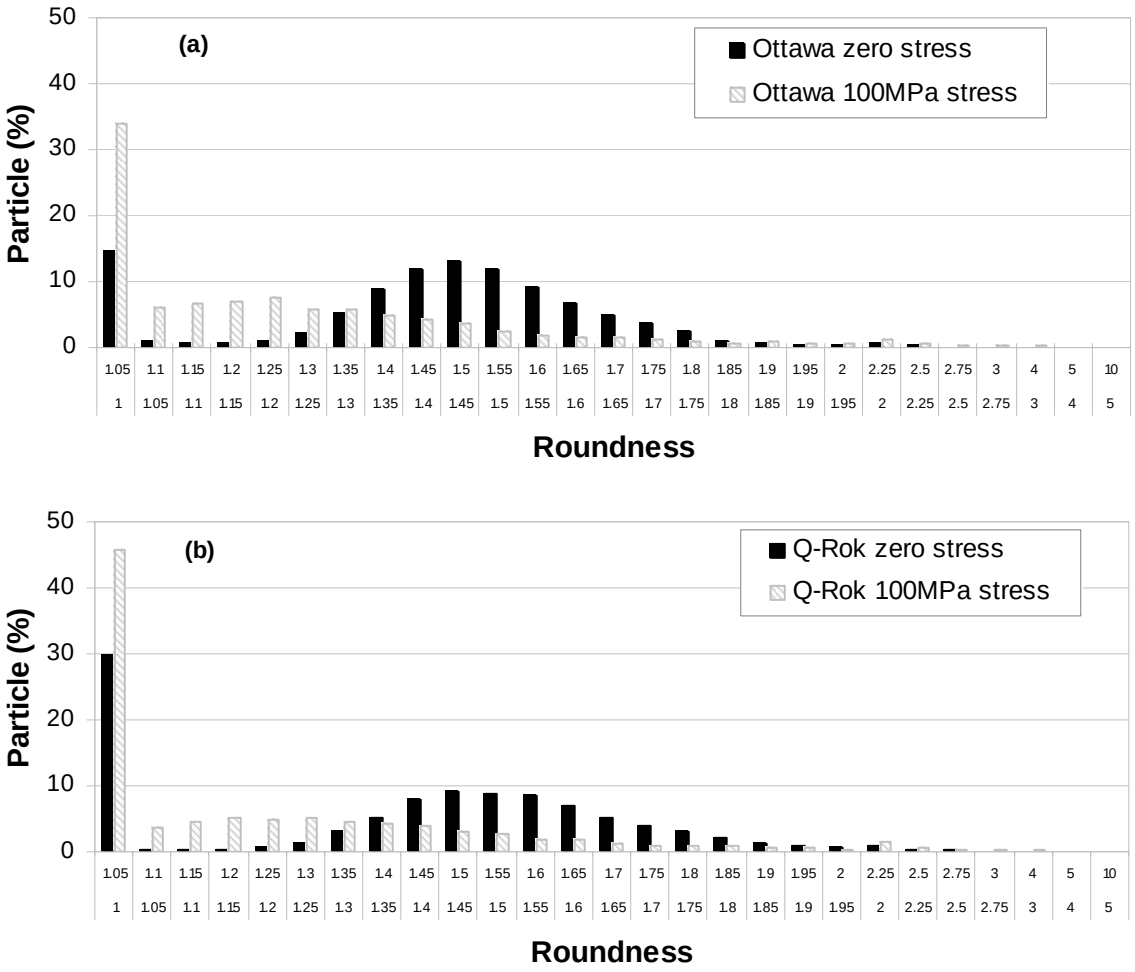

Figure 3.3: Comparison of particle shape analysis (roundness based) of (a) Ottawa sand and (b) Q-Rok sand samples at zero stress and 100 MPa stress.



Figure 3.4a: Ottawa sand before crushing.

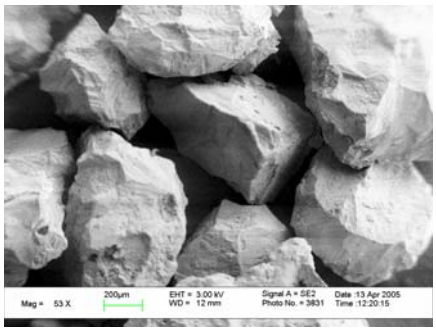

Figure 3.4b: Q-Rok sand before crushing

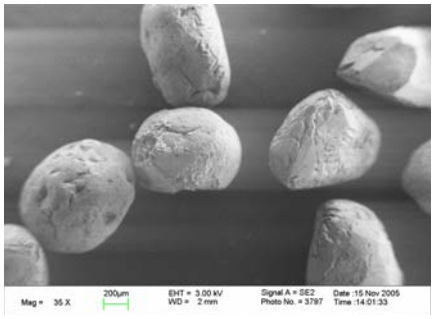

Figure 3.4c: Ottawa sand (Size >.6mm) at 55 MPa stress

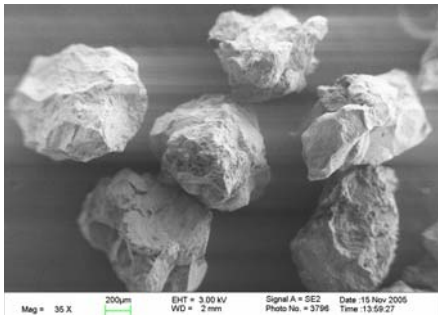

Figure 3.4d: Q-Rok sand (Size >.6mm) at 20 MPa stress

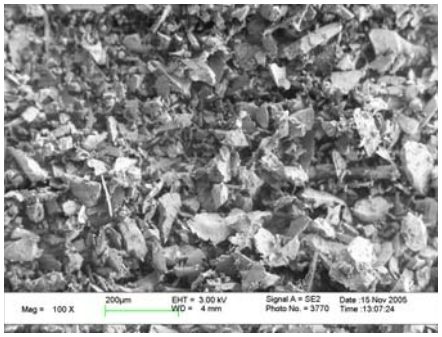

Figure 3.4e: Ottawa fines at 55 MPa stress

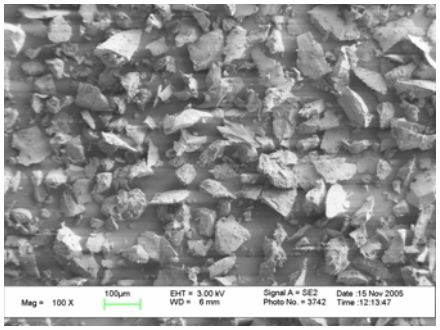

Figure 3.4f: Q-Rok fines at 20 MPa stress

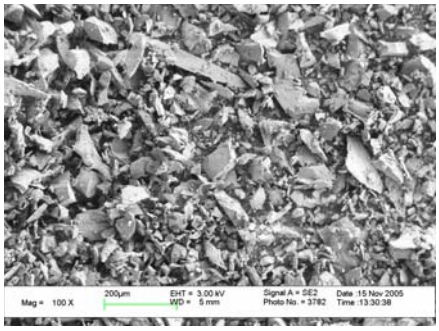

Figure 3.4g: Ottawa fines at 100 Mpa stress

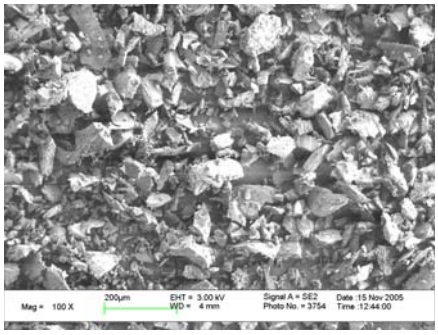

Figure 3.4h: Q-Rok fines at 100 Mpa stress

Figure 3.4: SEM images for Ottawa and Q-Rok sand particles at different stress.

Micro Particle Analysis:

Using FPIA, the analysis of shape and size for the finer samples (particle sizes below 75 μm) generated due to the applied vertical stress of 55 and 100 MPa on Ottawa sand and 20 and 100 MPa vertical stress on Q-Rok sand samples were analyzed. Again it is noted that untested specimens (0 MPa) did not have fines and therefore are not included in this analysis. Approximately 0.5 grams of representative sample was dispersed in 100 ml of de-ionized water for sample preparation and analysis through FPIA. Figures 3.5 and 3.6 present the number based and volume based distribution of particles for Ottawa sand subjected to 100 MPa and 55 MPa vertical stress and for Q-Rok sand at 100 MPa and 20 MPa vertical stress, respectively. It is seen from both the volume based and number based grain size distribution plots that the particle size distribution decreases with increasing applied stress for both types of samples, implying increased breakage of particles with increased stress level. It is also clearly evident from the analysis of finer particles (i.e. particles smaller than 75 microns passing through # 200mesh) that the percent passing based on equivalent volume of particles is higher for Ottawa sand between the intermediate and higher stress compared to Q-Rok sand. This suggests higher amount of particle breakage for finer fraction of Ottawa sand with stress level changes from 55MPa to 100MPa compared to the Q-Rok sand finer particles with stress level changes from 20MPa to 100MPa.

The corresponding circularity plots for Ottawa sand and Q-Rok sand samples are shown in Figures 3.7a and b, respectively. For Ottawa sand (Figure 3.7a) it is apparent that the circularity decreases with increasing applied stress. However, for Q-Rok sand

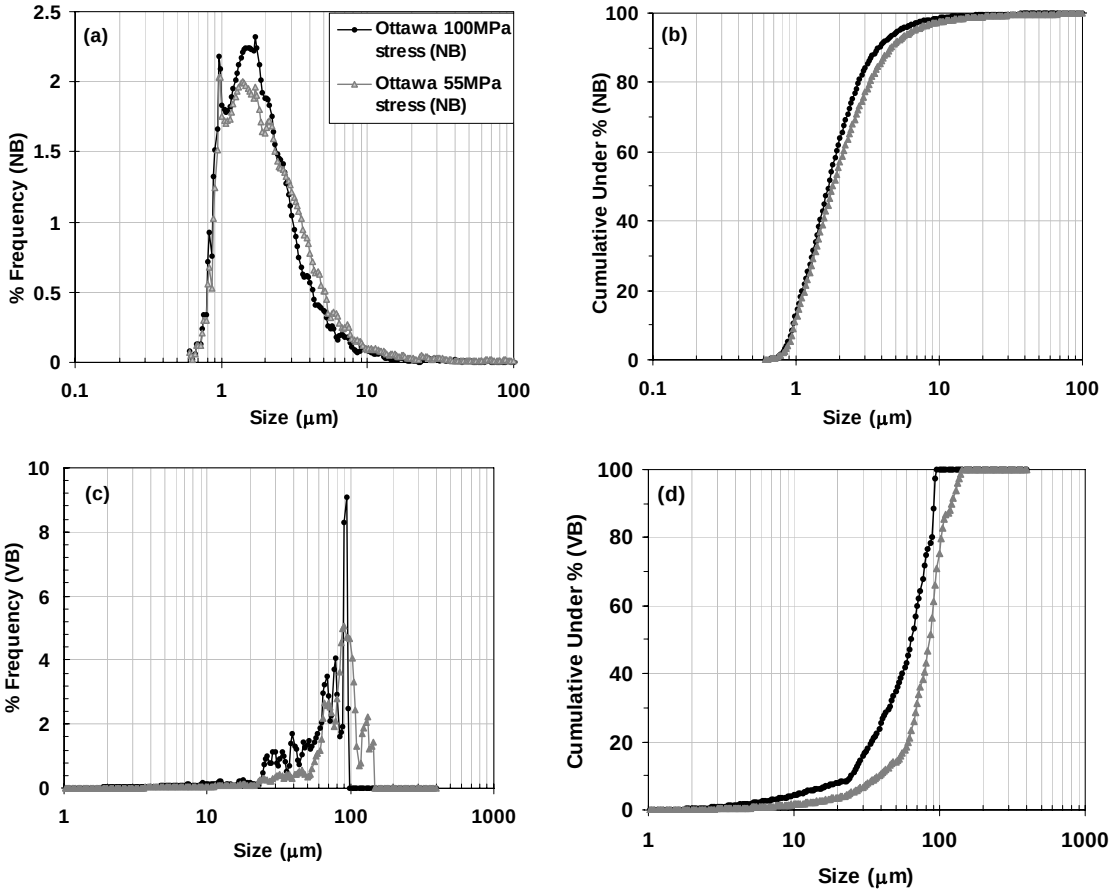

Figure 3.5: Distribution for finer particles (below 75μm based on sieve analysis) of Ottawa 100 and 55 MPa samples by digital image analysis using FPIA (a) plot showing number based percent frequency against size (b) number based cumulative under percent against size (c) volume based percent frequency against size and (d) volume based cumulative under percent against size.

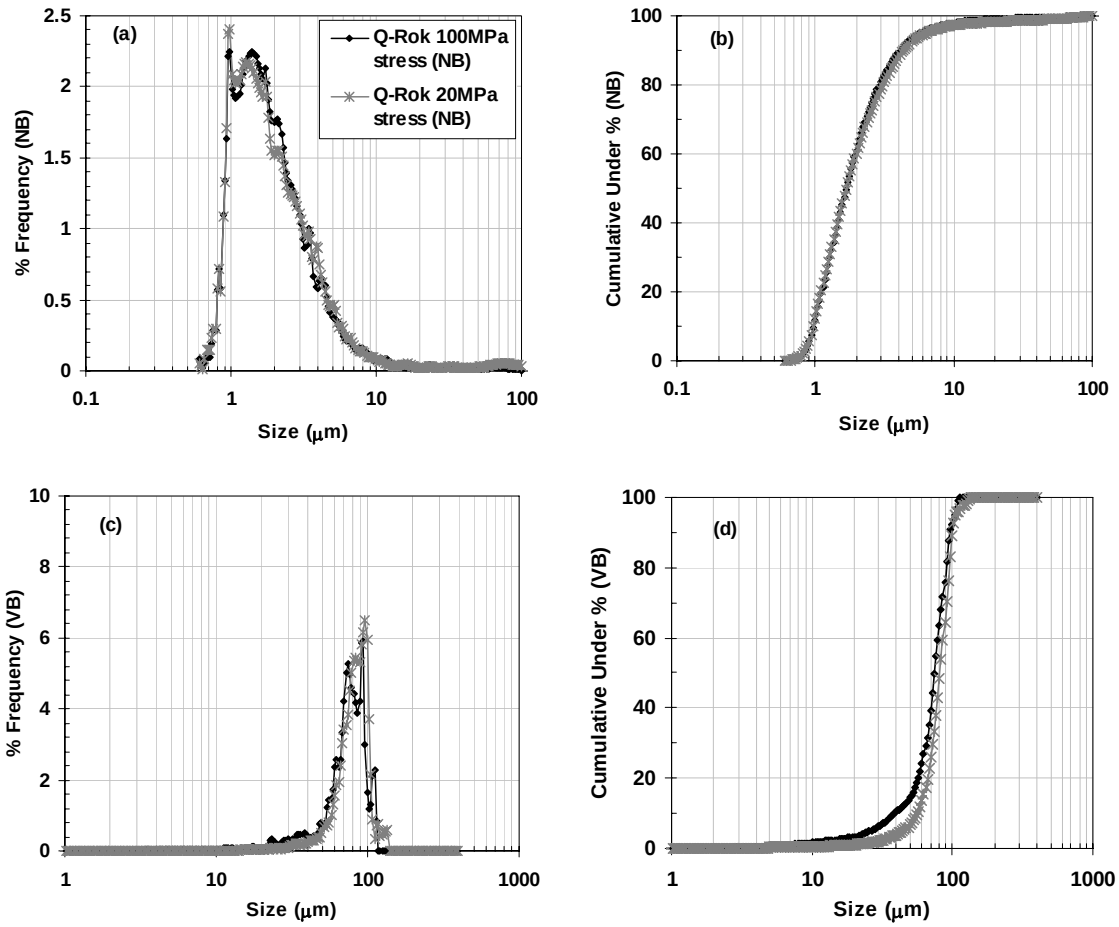

Figure 3.6: Distribution for finer particles (below 75μm based on sieve analysis) of Q-Rok sample at stress level 100MPa and 20 MPa by digital image analysis using FPIA (a) plot showing number based percent frequency against size (b) number based cumulative under percent against size (c) volume based percent frequency against size and (d) volume based cumulative under percent against size.

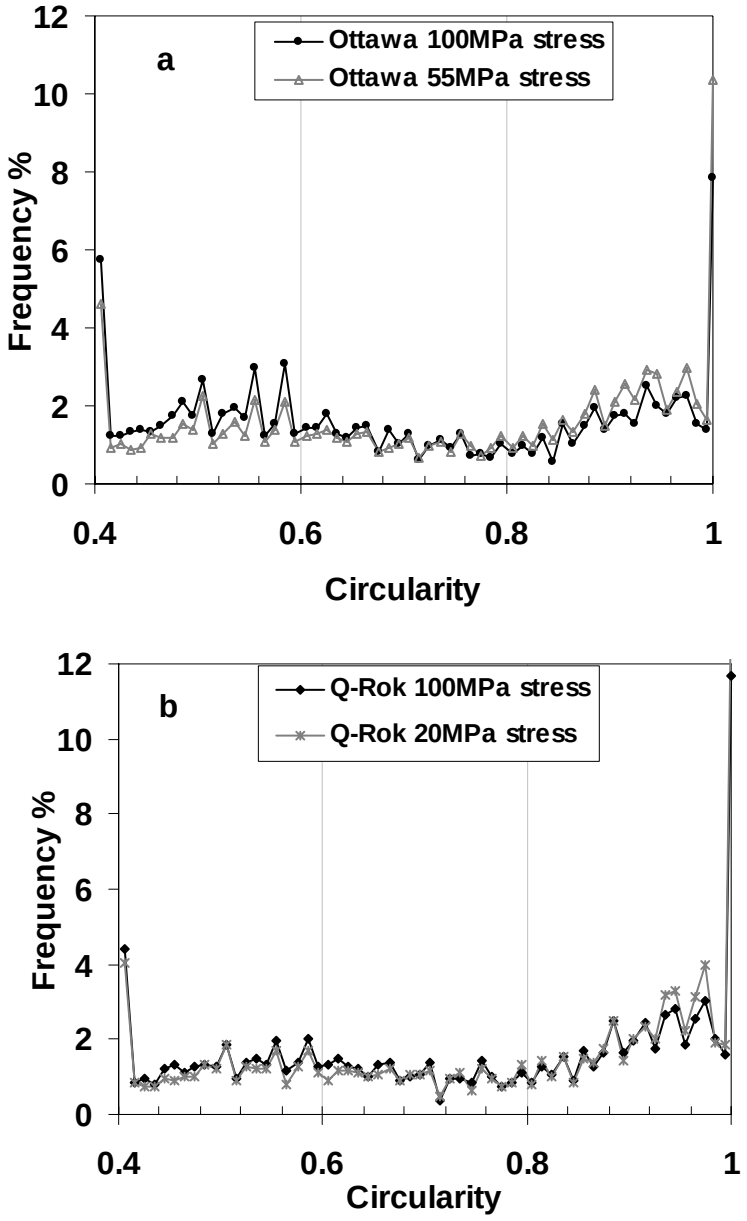

Figure 3.7: Plot showing circularity of particles (below 75μm based on sieve analysis) at different applied stresses by digital image analysis using FPIA for (a) Ottawa sand and (b) Q-Rok sand samples.

finer particles (Figure 3.7b) the differences are not as significant. This implies that increased stress produces higher angularity in the finer particles (size ranges below 75 μm) of Ottawa sand. For Q-Rok sand this trend is not apparent, indicating that the increased stress does not affect the finer particles in the same way.

Comparative number based and volume based distribution plots for Ottawa sand and Q-Rok sand finer particles at 100 MPa applied vertical stress are shown in Figure 3.8. While there is minimal difference in the number based distribution for the Ottawa and Q-Rok finer particles, the volume based distribution shows a higher fraction for Ottawa finer particles compared to Q-Rok finer particles for all size ranges at 100 MPa stress level. It is also observed that at the same applied stress of 100 MPa, the circularity distribution of Ottawa sand particles is lower than the circularity of Q-Rok samples, with more low circularity values.

Typical images of Ottawa and Q-Rok sand finer particles passing #200 sieve (< 75 μm) at the intermediate and higher stress levels at different size ranges observed using FPIA are shown in Figure 3.9. It is evident that smaller size range particles (5-10μm) at a particular stress level are more circular than the larger size range particles (10-20μm). It is also observed from the particle images that the Q-Rok particles are more circular compared to the Ottawa particles at any stress level.

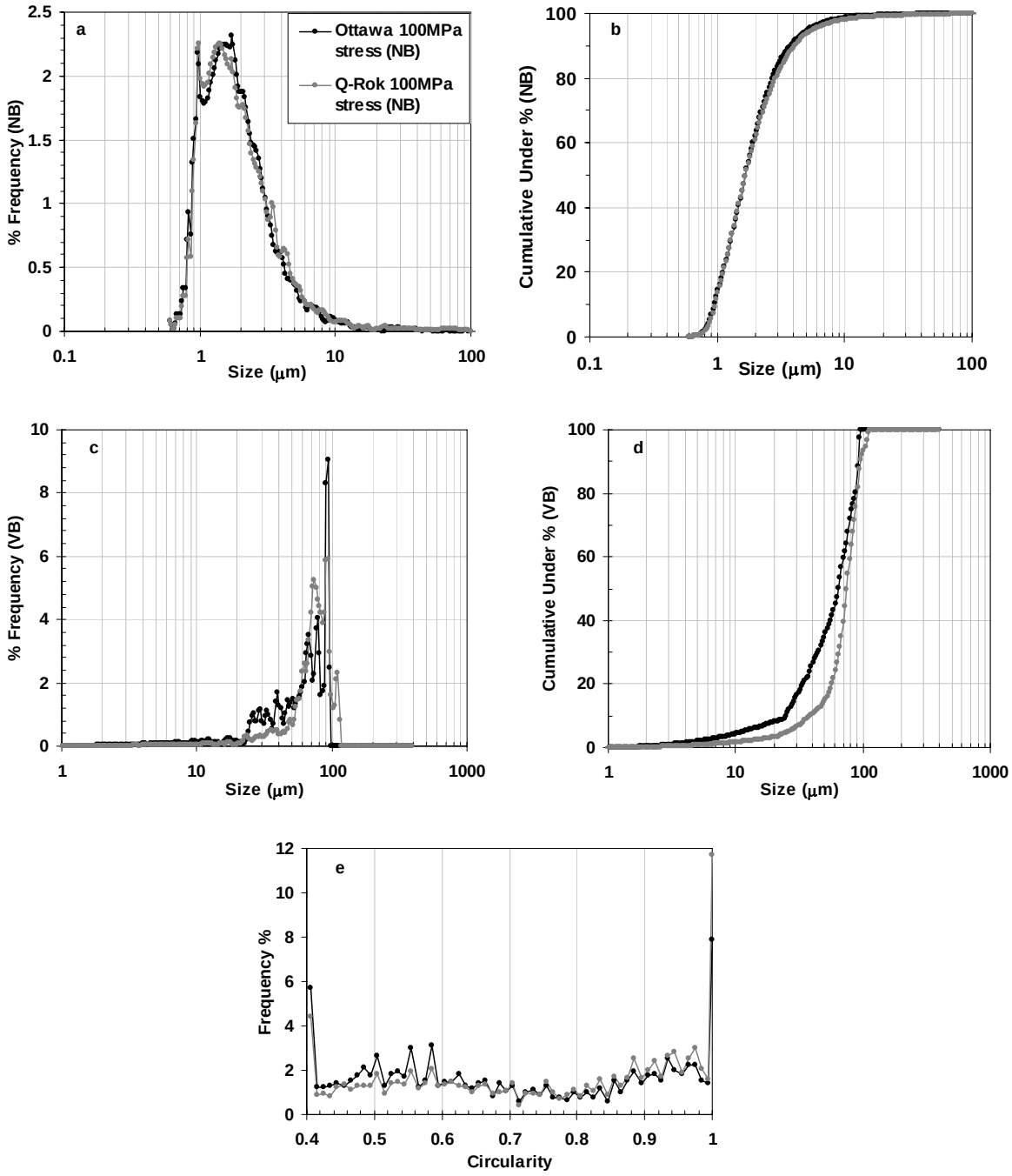

Figure 3.8: Comparative grain size distribution for Ottawa sand and Q-Rok sand at 100MPa applied stress for particle sizes below 75μm (based on sieve analysis) analyzed by digital image analysis using FPIA (a) number based percent frequency against size (b) number based cumulative under percent against size (c) volume based percent frequency against size (d) volume based cumulative under percent against size and (e) circularity plot.

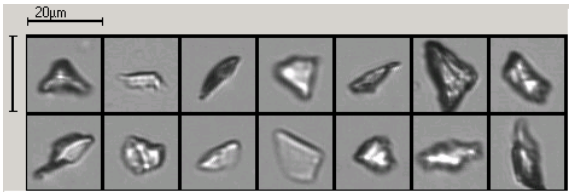

Figure 3.9a: Ottawa 100 MPa; Size range: 10-20 µm

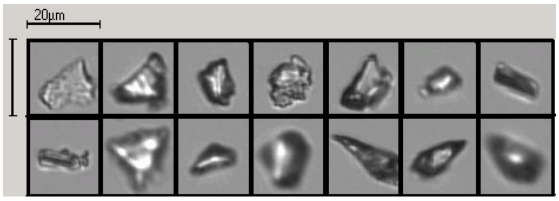

Figure 3.9b: Ottawa 55MPa; Size range: 10-20 µm

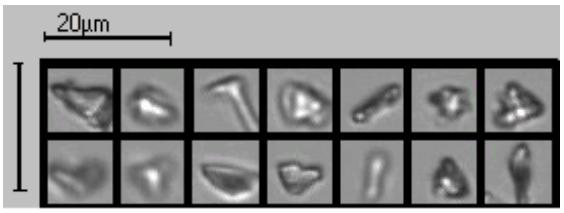

Figure 3.9c: Ottawa 100 MPa; Size range: 5-10 µm

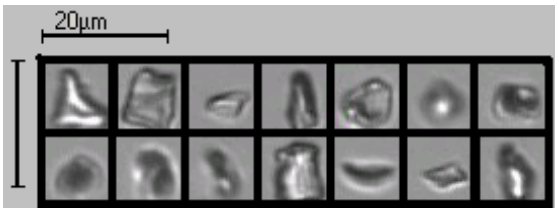

Figure 3.9d: Ottawa 55MPa; Size range: 5-10 µm

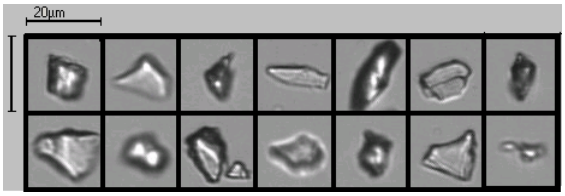

Figure 3.9e: Q-Rok 100 MPa; Size range: 10-20 µm

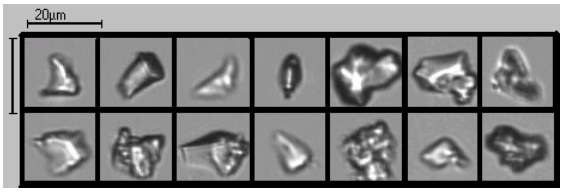

Figure 3.9f: Q-Rok 20 MPa; Size range: 10-20 µm

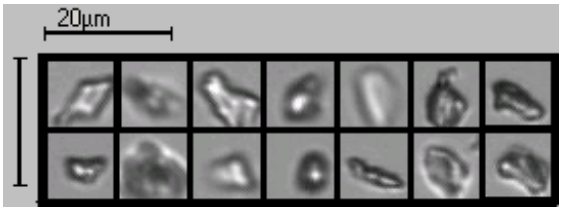

Figure 3.9g: Q-Rok 100 MPa; Size range: 5 - 10 µm

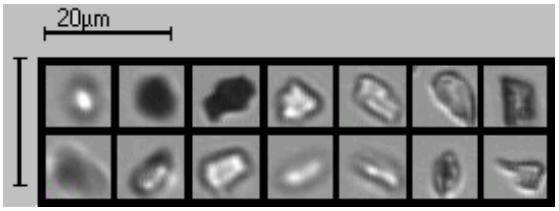

Figure 3.9h: Q-Rok 20 MPa; Size range: 5 - 10 µm

Figure 3.9: Typical images of Ottawa sand and Q-Rok sand particles as observed using FPIA (a) Ottawa 100 MPa; size range: 10 – 20µm (b) Ottawa 55 MPa; size range: 10 – 20µm (c) Ottawa 100 MPa; size range: 5 – 10µm (d) Ottawa 55 MPa; size range: 5 – 10µm (e) Q-Rok 100 MPa; size range: 10 – 20µm (f) Q-Rok 20 MPa; size range: 10 – 20µm (g) Q-Rok100 MPa; size range: 5 – 10µm (h) Q-Rok 20 MPa; size range: 5 – 10µm.

Using laser light scattering through Malvern Mastersizer S, the shape and size distribution were also analyzed for finer particles (diameter <75μm through sieve analysis) generated due to the applied vertical stress of 55 and 100 MPa on Ottawa sand and 20 and 100 MPa stress on Q-Rok samples.

Figures 3.10 and 3.11 show the volume based and number based distribution patterns for Ottawa and Q-Rok sand samples, respectively. From volume based distribution for both types of sand samples it is noticed that the distribution plot shifts towards the left with increasing applied stress. Thus, as observed with FPIA, the laser light scattering results indicate the particle size reduction with increasing applied stress. The comparative distribution analysis of Ottawa and Q-Rok sand finer particles for 100 MPa stress is shown in Figure 3.12. The volume based comparative distribution shows that Q-Rok sand produces a higher fraction of finer particles than Ottawa sand at 100 MPa vertical stress.

The repeatability of the test results for mean particle diameter analyzed using image processing by FPIA and laser light scattering by Malvern Mastersizer S for particles below 75 μm (as per dry sieve analysis) of Ottawa sand and Q-Rok sand samples (each sample analyzed three times) at different applied stress levels is summarized in Table 3.1. Very good repeatability was obtained, which is evident from the small standard deviation values. It is observed from the number based measurements through FPIA that for Ottawa sand finer particles, the mean diameter reduces by 19% with vertical stress increases from 55 MPa to 100 MPa, whereas for Q-Rok sand finer

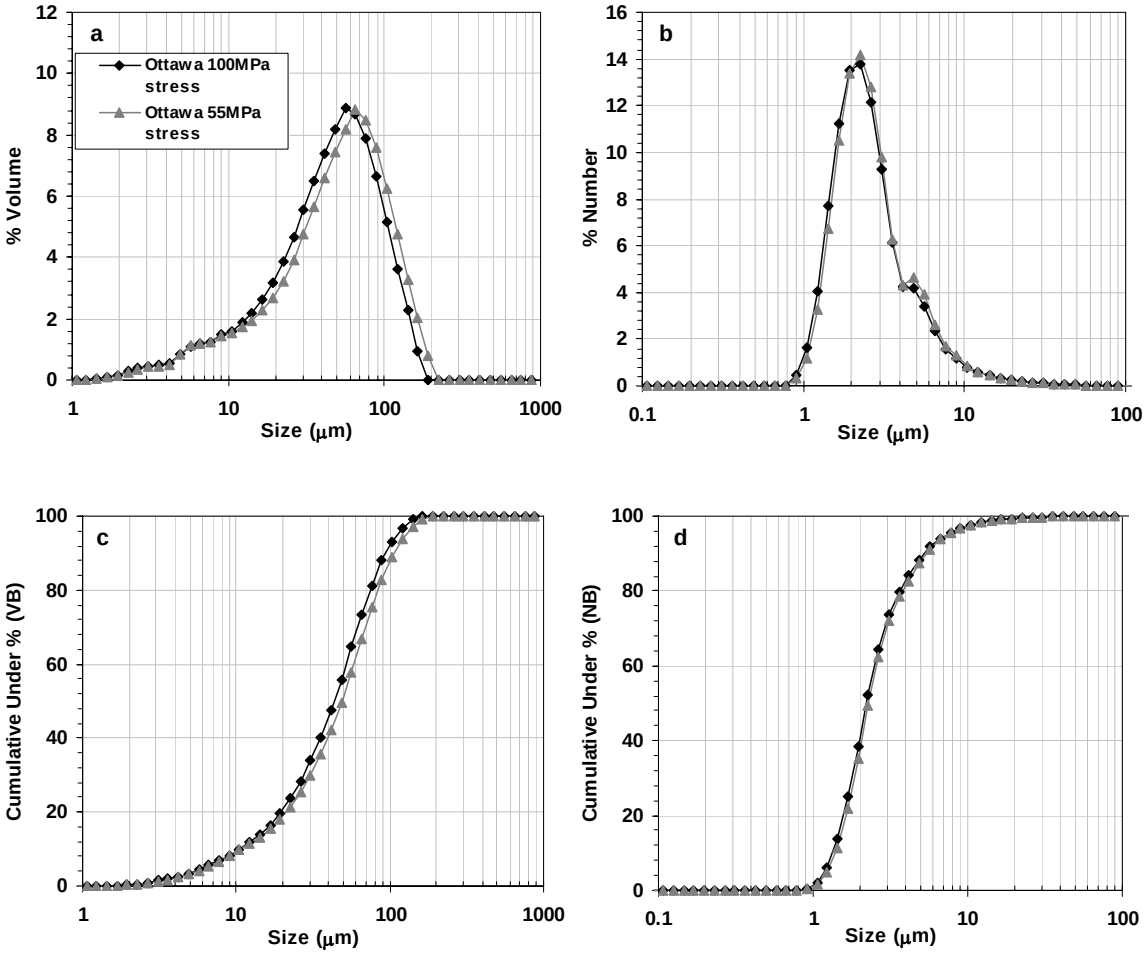

Figure 3.10: Comparative grain size distribution for Ottawa sand at different applied stress for finer particles (diameter <75μm through sieve) analyzed through laser diffraction (a) volume based percent frequency against size (b) number based percent frequency against size (c) volume based cumulative under percent against size (d) number based cumulative under percent against size.

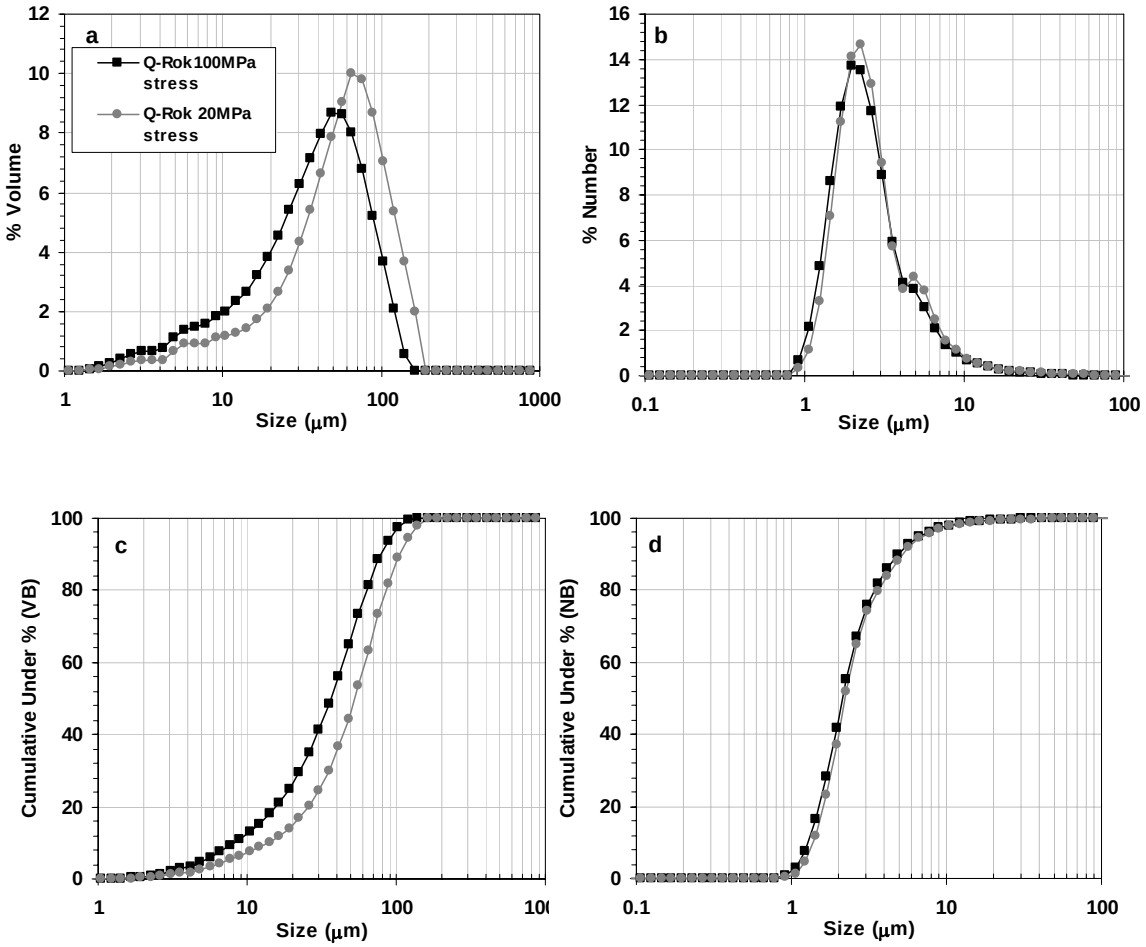

Figure 3.11: Comparative grain size distribution for Q-Rok sand at different applied stress for finer particles (diameter <75μm through sieve) analyzed through laser diffraction (a) volume based percent frequency against size (b) number based percent frequency against size (c) volume based cumulative under percent against size (d) number based cumulative under percent against size.

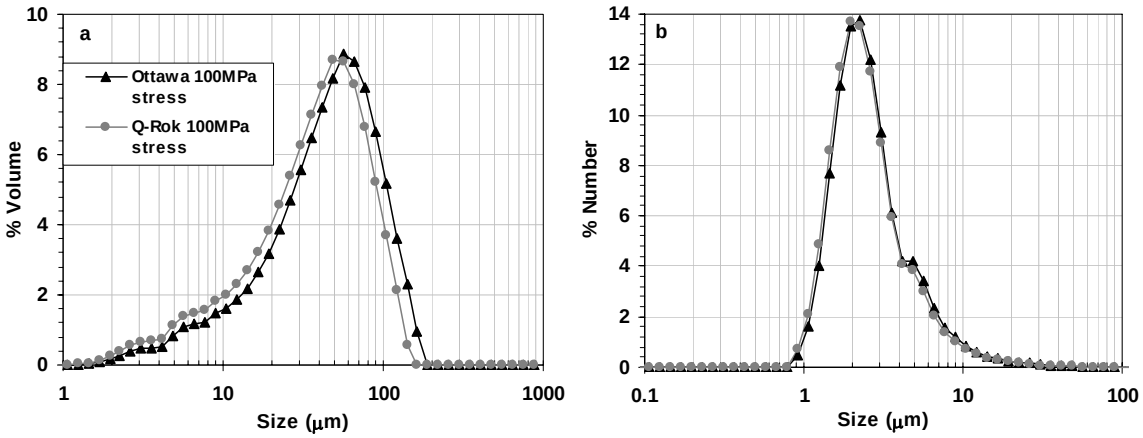

Figure 3.12: Comparative grain size distribution analysis for Ottawa and Q-Rok sand finer particles (diameter <75μm through sieve) at 100 MPa stress analyzed through laser diffraction (a) volume based and (b) number based.

Table 3.1: Summary of number based and volume based mean diameter and standard deviation based on three repeatability tests by FPIA and laser diffraction on Ottawa and Q-Rok sand finer particles (particle diameter below 75 μm through dry sieve) at intermediate and higher stress.

Sample Name	Technique							
	Image processing by FPIA				Laser light scattering by Mastersizer			
	Number Based		Volume Based		Number Based		Volume Based	
	Mean Diam. (μm)	Std. Deviation	Mean Diam. (μm)	Std. Deviation	Mean Diam. (μm)	Std. Deviation	Mean Diam. (μm)	Std. Deviation
Ottawa 55MPa stress	2.94	0.1	79.91	3.24	2.28	0.023	48.26	0.223
Ottawa 100MPa stress	2.37	0.015	61.46	2.96	2.22	0.01	43.07	0.706
Q-Rok 20MPa stress	3.16	0.098	79.99	1.28	2.22	0.012	53.35	1.405
Q-Rok 100MPa stress	2.69	0.067	74.35	1.45	2.12	0.034	36.03	2.098

particles an approximately 15% reduction in mean diameter is noticed with vertical stress increases from 20 MPa to 100 MPa. The corresponding differences in mean diameter through laser light scattering are not so significant (2% reduction for Ottawa sand and 4% for Q-Rok sand), but it also reflects the similar trend of decreasing mean diameter with increasing stress level for finer particles of both types of sand. Significant reduction in volume based mean diameter with increasing stress for Ottawa and Q-Rok finer particles are also evident from Table 3.1.

It is also observed from both the number based and volume based measurement through FPIA (Table 3.1) that the mean diameter of Ottawa sand finer particles (i.e. particle sizes below 75 μm passed through dry sieve of # 200 mesh) at 100 MPa stress is smaller than the mean diameter of Q-Rok sand finer particles at the same stress. Contrary to the FPIA results, laser light scattering analysis shows that the mean diameter of Q-Rok sand (finer particles passed through #200mesh) at 100 MPa stress are lower than the mean diameter of Ottawa sand at the same stress. However, it should be recognized that the distribution analysis done by digital image processing through FPIA and by laser light scattering through Malvern Mastersizer S are completely two different procedures. In laser light scattering the basic result produced by the analysis is a volume based distribution using Mie theory [18] which presumes particles are perfect spheres. The analyzed distribution is expressed in a set of size classes which are optimized to match the detector geometry and optical configuration giving the best resolution. All parameters are derived from this fundamental distribution. The distribution parameters and derived

diameters are calculated from the fundamental distribution using the summation of the contributions from each size band where in performing this calculation the representative diameter for each band is taken to be the geometric mean of the size band limits expressed by:

$$\sqrt{d_l d_{l+1}} \tag{3.6}$$

However, in the image processing through FPIA, the analysis of particle distribution is made using the projected area and circumference of each particle. A circle having the same area as the projected area of the particle in question is assumed, and its diameter is calculated. As discussed previously, in the number based distribution, the number of particles (f_{0l}) whose circular diameter d_i are within the range of d_l to d_{l+1} is calculated, whereas for volume based the overall volume of particles (f_{3l}) whose circular diameter d_i are within the range of d_l to d_{l+1} is calculated. An equivalent sphere is considered for the volume calculation. The representative diameter for each size bin is calculated by the arithmetic mean of the size band limits as follows:

$$\frac{d_l + d_{l+1}}{2} \tag{3.7}$$

The shape characteristics analyzed by image processing through FPIA of the finer particles (diameter <75 μm through dry sieve) for two types of sand samples at intermediate and higher stress is summarized in Table 3.2. The results shown here are the mean of the three repetitive tests performed on each sample. It is observed that the mean circularity decreases with increasing stress for the finer fraction of both types of sand.

Table 3.2: Summary of shape analysis (circularity based) by image processing through FPIA on Ottawa and Q-Rok sand finer particles (particle diameter below 75 μm through dry sieve) at intermediate and higher stress.

Sample Name	Circularity		
	Mean Circ.	50% Circ.	Circ. <0.85 (%)
Ottawa 55MPa stress	0.746	0.78	57.27
Ottawa 100MPa stress	0.701	0.67	66.20
Q-Rok 20MPa stress	0.774	0.83	50.95
Q-Rok 100MPa stress	0.749	0.78	56.57

The mean circularity of the Ottawa sand at 100 MPa stress is also lower than the mean circularity of Q-Rok samples at 100 MPa stress, whereas the percentage of finer particles with circularity <0.85 for Ottawa sand at 100 MPa stress is much higher than Q-Rok sand at similar stress. These observations further confirm earlier observations that with increasing stress the finer particles develop more angularity.

Prior to the application of one-dimensional compressive stress, Ottawa sand and Q-Rok sand had similar size distributions (Figure 3.2) and very different morphology (Figures 3.4a and 3.4b). Analysis of these samples subjected to a given compressive stress (for example Figure 3.8 corresponding to 100 MPa vertical stress) shows interesting results. Contrary to the expectations, for a portion of the material that is smaller than approximately 75 microns (i.e., passing through # 200 mesh), the percent finer based on equivalent spherical volume of particles at a given size range is higher for

Ottawa than Q-Rok. This observation was also found to be true for intermediate vertical stress value (Figure 3.5 and 3.6). A rational explanation for this observation is as follows. At micro level, Ottawa sand produces higher volume fraction of finer particles compared to Q-Rok sand under similar imposed stress. Though the axial strain resulting from confined compression for Ottawa sand is much lower than Q-Rok, the Ottawa particles that undergo crushing break into multiple finer pieces, where as a likely mechanism for particle crushing in Q-Rok is the breakage of individual particle asperities from the particle edge. This observation is also consistent with morphology data listed in Table 3.2. The mean circularity of Ottawa sand particles is less than Q-Rock indicating more angularity of fine particles. Since both the Ottawa and Q-Rok sand have similar mineralogy and crystallographic structure, it is concluded that particle shape plays a significant role in crushing behavior of granular materials.

CONCLUSION

Grain-size distribution and shape analysis at the macro (> 75 μm) and micro (< 75 μm) length scales determined by using several processes/techniques were evaluated for Q-Rok and Ottawa samples at select applied stress levels. In particular, specimens from stress levels 0 MPa and 100 MPa captured together encompass the total possible range while the intermediate stress level specimens roughly correspond to the transition to substantial non-linear behavior. The comparative grain size distribution analysis by sieve analysis shows that the sub-angular Q-Rok samples produces a higher fraction of finer aggregates as compared to the sub-rounded Ottawa sand samples at 100 MPa. This implies that macro level Q-Rok samples are subjected to more crushing than the Ottawa

sand at 100 MPa stress. The shape histogram through PSDA clearly indicates an increase in roundness for both types of specimens with increasing applied stress.

The size distribution analysis of particles finer than 75 μm through digital image analysis by Flow Particle Imaging Analyzer (FPIA) reveals that increasing applied stress generates more finer fraction of particles and at 100 MPa stress the mean size of Ottawa sand particles are comparatively smaller than the Q-Rok sand particles. The shape characteristic of the finer particles for different specimens has also been analyzed in terms of circularity. It is seen that the circularity decreases with increasing applied stress implying that the micro level particles (< 75 μm) are becoming more angularity due to the increased stress level. Comparison between Ottawa and Q-Rok sand particles at 100 MPa indicate that the finer fraction of Ottawa sand particles develop higher angularity than the Q-Rok sand particles. In contrast to the particle breakage behavior at macro level (i.e. sub-angular Q-Rok sand undergoes more breakage than sub-rounded Ottawa sand), the micro level particle analysis shows that Ottawa sand produces a higher volume fraction of finer particles compared to Q-Rok sand under similar imposed stress levels. The particle shape is suggested to be the principle governing factor that controls such particle breakage behavior for the two types of sand analyzed in this study.

The micro level size distribution has also been analyzed by laser light scattering technique and we observed good agreement of the distribution pattern between FPIA and the laser light scattering results. However, there is a disagreement regarding mean particle size of the finer particles as measured by the two processes. The laser light

scattering results show that the mean diameter of Q-Rok specimens are lower than the Ottawa sand particles at 100 MPa stress level which is in contrast to FPIA results. The differences as is explained here is due to the fundamental differences between the separate techniques and theory used by these two systems while calculating the size distribution.

REFERENCES

1. Hardin, B.O., *"Crushing of soil particles",* J. of Geotec.Engrg., ASCE, 1985, 111(10), 1177-1192.
2. Lee, K.L. and Farhoomand, I., *"Compressibility and crushing of granular soils in anisotropic triaxial compression",* Can. Geotech. J., Ottawa, Canada, 1967, 4(1), 68-86.
3. Lo, K.Y. and Roy,M., *"Response of particulate materials at high pressures".* Soils and found.,Tokyo, Japan, 1973, 13(1), 1-14.
4. Marsal, R.J., "*Large scale testing of rockfill materials",* J. of Soil Mech. and Found. Div., ASCE, 1967, 93(2), 27-43.
5. Leslie, D.D., "*Large scale triaxial tests on gravelly soils",* Proc. of the 2nd Pananerican conf. on soil mech. and found. Engr., 1963, 1, 183-202.
6. Leslie, D.D., "*Shear strength of rockfill",* Physical properties engineering study, US Army Corps of Engineering, 1975, 526, 124.
7. Lade, P.V.; Yamamuro, J. A.; Bopp, P. A., *"Significance of particle crushing in granular materials",* J. of Geotechnical Engineering, 1996, April, 309-316.

8. Lanaro, F.; Tolppanen, P., *"3D characterization of coarse aggregates",* Engineering Geology, 2002, 65, 17–30.

9. Provder, T., *"Challenges in particle size distribution measurement past, present and for the 21st century",* Progress in Organic Coatings, 1997, 32, 143-153.

10. Xu, R.; Guida, O. A. D., *"Comparison of sizing small particles using different technologies",* Powder Technology, 2003, 132, 145 – 153.

11. Pons, M.N.; Vivier, H.; Belaroui, K.; Bernard,M. B.; Cordier, F.; Oulhana, D.; Dodds, J.A., *"Particle morphology: from visualisation to measurement",* Powder Technology, 1999, 103, 44–57.

12. Pellegrin, D. V. D.; Stachowiak, G. W., *"Assessing the role of particle shape and scale in abrasion using 'sharpness analysis'Part I. Technique development",* Wear, 2002, 253, 1016–1025.

13. Zhang, P.-C.; Liu, J.; Chew, C.H.; Gan, L.M.; Li, S.F.Y., *"AFM imaging and characterization of latex particles formed by copolymerization of styrene and poly(ethylene oxide) macromonomer",* Talanta, 1998, 45, 767–773.

14. Christoph, G.G., "*Influence of particle properties and initial specimen state on the specimen response to one-dimensional loading at high stresses",* MS Thesis, University of Massachusetts, Amherst, 2005, 268.

15. DeJong, J.T. and Christoph,G.G*., "Relation of initial specimen state and particle properties to the breakage potential of granular soils*", 57th Canadian Geotechnical Conference; 5th Joint CGS/IAH-CNC Conference, 2004, Geo Quebec, 21-27.

16. Wettimuny, R.; Penumadu, D., *"Application of fourier analysis to digital imaging for particle shape analysis",* J. of Computing in Civil Engg. ASCE, 2004, 2-9.

17. Malvern Instruments Ltd. Mastersizer user manuals. 1997.

18. Gise, P., *"Laser light scattering as a method of detecting and sizing particulates on smooth planar surface",* Particulate science and technology, 1988, 6(1), 29-41.

PART 4: MECHANICAL PROPERTIES OF BLENDED SINGLE WALL CARBON NANOTUBE COMPOSITES

This part is a slightly revised version of a paper with the same title published in the Journal of Material Research in August 2003 by Dayakar Penumadu, Amal Dutta, George M. Pharr and B.Files:

D. Penumadu, A. Dutta, G. M. Pharr and B. Files “Mechanical Properties of Blended Single Wall Carbon Nanotube Composites” J. Mater Res., Vol. 18, No. 8, Aug 2003.

My primary contributions to this paper include (1) developing of experimental setup, (2) most of the gathering and interpretation of literature, (3) performing the laboratory experiments, (4) interpretation and analysis of test results, (5) most of the writing.

ABSTRACT

The improvement in mechanical properties of blended nanocomposites prepared using a low-viscosity, liquid epoxy resin and purified single-wall carbon nanotubes (SWCNTs) was evaluated. The macroscopic tensile stress–strain behavior for hybrid materials made with varying amounts of SWCNT was determined and showed little improvement in the breaking tensile strength. The corresponding variations in modulus and hardness were obtained using nanoindentation considering time effects and showed quantifiable but modest improvements. The small changes in the observed stiffness and breaking strength of carbon nanotube composites is due to the formation of bundles and their curvy morphology.

INTRODUCTION

In 1985, a new form of carbon, buckministerfullerene C60 was discovered by Smalley and co-workers at Rice University [1]. C60 is a geometric cage-like structures of pure carbon atoms bonded in hexagon and pentagon configurations. Besides diamond, graphite and C60, the quasi one-dimentional nanotube is another form of carbon first reported by Iijima in 1991 when he discovered multi-walled carbon nanotubes (MWNT) in carbon soot made by arc-discharge method [2,3]. About two years later, observations of single-wall carbon nanotubes (SWCNT) were made [4]. Since then the SWCNT have stimulated great interest in various scientific communities [5,6]. A significant amount of work has been done in the past decade to reveal the unique structural, electrical, mechanical, electrochemical and chemical properties of individual carbon nanotubes. Nanotubes are long, slender fullerenes where the walls of the tubes are hexagonal carbon (graphite structure) and often capped at each end. The carbon nanotubes have been shown to exhibit exceptional material properties that are a consequence of their symmetric structure. Many researchers have reported mechanical properties of carbon nanotubes that exceed those of any previously existing materials. Although there are varying reports in the literature on the exact properties of carbon nanotubes, theoretical and experimental results have shown extremely high elastic modulus, greater than 1 TPa (the elastic modulus of diamond is 1.2 TPa) and reported strengths 10 – 100 times higher than the strongest steel at a fraction of the weight. In addition to the exceptional mechanical properties associated with carbon nanotubes, they also posses superior thermal and electric properties: thermally stable up to 2800^0 C in vacuum, thermal conductivity about twice as high as diamond, electric-current-carrying capacity 1000 times higher than

copper wires [7]. These exceptional properties of carbon nanotubes have led to an explosion of research efforts worldwide.

The chirality of the carbon nanotubes has significant implications on the material properties and its effect on the elastic and other mechanical properties of carbon nanotubes is unclear. Lourie et al. have studied the dependence of elastic properties on the diameter and chirality of carbon nanotubes [8]. They observed that diameter selective resonance raman scattering can be employed to sense the elastic properties of armchair SWCNTs having different diameter. Tensile properties of both the multi-wall and single-wall nanotubes have been evaluated by attaching between two opposing atomic force microscope tips or specially designed stress-strain gage and loading under tension [9-12]. For single-wall nanotube ropes, assuming that only the outermost tubes assembled in the rope carried the load during the experiment, tensile strengths of 13 to 52 Gpa and average elastic moduli of 320 to 1470 Gpa were reported. The elastic properties of SWCNTs in compression was studied by Cornwell et al. [13]. Molecular dynamics simulations were used to investigate the elastic behavior of open-ended, free-standing SWCNTs. Tubes compressed in this process were found to maintain their cylindrical symmetry until some critical value of the strain was reached at which point the tubes buckled. Though the mechanical property information of hybrid materials made from SWCNT and polymers is limited to date, the primary issue that has been raised is related to poor matrix and SWCNT interface properties. The present research results present additional insight on this aspect.

EXPERIMENTAL

SWCNTs used in this study were made using the laser ablation technique and were obtained from Tubes@Rice [14]. To minimize phase segregation during the preparation of polymer composite material [15], the following specimen preparation approach was developed at National Aeronautics and Space Administration/Johnson Space Center. Because of its compatibility with nanotubes, long gel time for mixing and degassing, and low viscosity, commercially available EPON Resin 862 was used with Curing Agent W, available from Resolution Performance Products (www.resins.com; Houston, TX). Details on specimen preparation are included because of the lack of such information in the published literature and its importance.

(i) Sonicate nanotube solvent (acetone/toluene azeotrope) mixture in a bath for 1 h. (ii) Add the desired amount of resin, catalyst, and nanotube suspension to a beaker, where the ratio of resin to catalyst is 100:26.4 by weight. (iii) To evaporate the solvents place the beaker on a hot plate/stirrer combo, turn on the hot plate to 60 °C, and start stirring. (iv) Let samples stir as necessary until the solvent is removed completely. (v) Stir manually with glass stir rod for 2–3 min. (vi) Degas in vacuum oven at 60 °C for 3.5 h (also removes remaining solvent). (vii) Warm up the mold to 60 °C in an oven. (viii) Load the compression mold with material. (ix) Place mold in a vacuum oven at 60 °C for about 1 h for further degassing. (x) Remove from vacuum oven and place in a press. (xi) Insert the plunger into the mold and add pressure. (xii) Cure the sample. The cure cycle is 121 °C for 1 h and 177 °C for 2.5 h. Figure 4.1 shows the details of the compression mold, and Figure 4.2 shows a Teflon piece used to minimize extrusion and a 3% by



Figure 4.1: Compression Mold

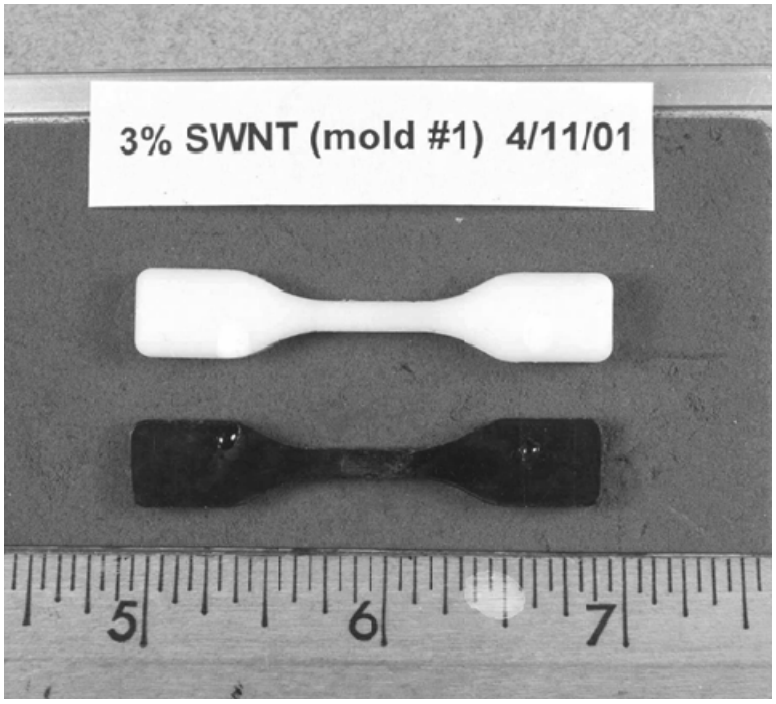

Figure 4.2: Dog Bone Specimens

weight SWCNT specimen.

RESULTS AND DISCUSSION

In the radial breathing mode, the characteristic Raman peak corresponding to radial displacement of carbon atoms for SWCNT (with a diameter of 1.01 nm) used in this research was approximately at 202.7 cm^{-1} for a laser at 780 nm wavelength. As can be seen from Figure 4.2 (and will be seen later in this section), relatively good dispersion was achieved for the current samples. The state of dispersion can also be qualitatively evaluated by observing the occurrence of localized initiation sites leading to premature fracture during a tensile test.

The results from tensile tests (ASTM D-638) performed on dog bone specimens is shown in Figure 4.3. It can be seen that the state of stress corresponding to failure (peak point in the curve) shows a slight decrease (4%) for epoxy specimens added with SWCNT at 1% and 3% by weight and shows 7% increase for blended composite with 5% SWCNT. Figure 4.3 also shows small changes in the initial stiffness (slope of stress–strain curve) corresponding to tensile Young's modulus for increasing nanotube content, and no quantitative conclusions are made due to a lack of high resolution in the small strain measurements. Strain to failure decreased with the use of carbon nanotubes indicating a brittle character more than that of pure epoxy. For all practical purposes, these data suggest that no significant changes in macroscopic stress–strain behavior of epoxy with SWCNTs were observed for tensile test data. Possible reasons for these observations are discussed later.

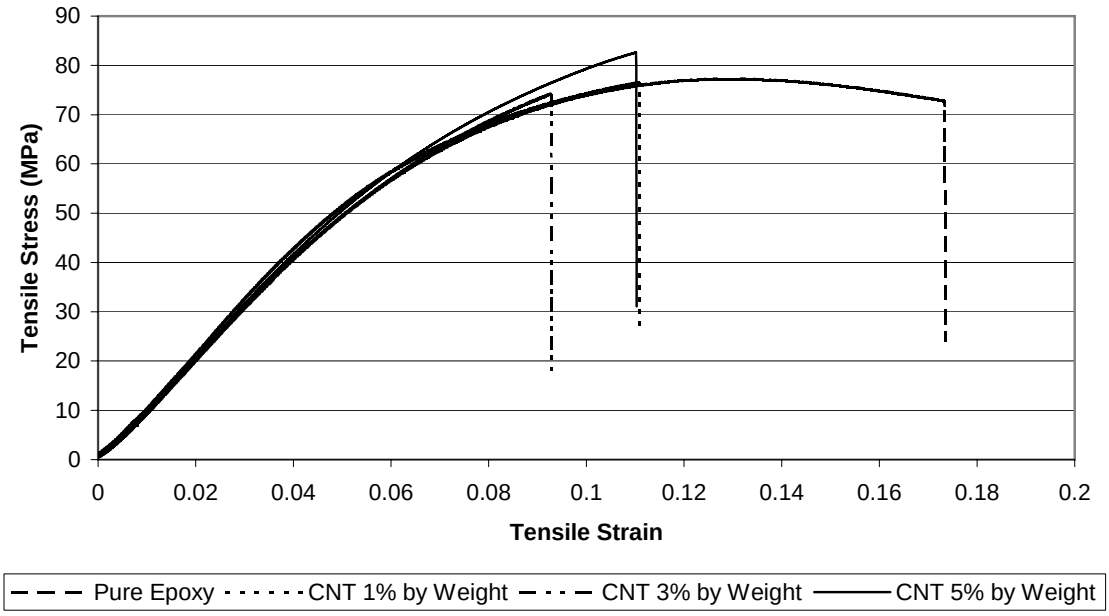

Figure 4.3: Data from Tensile Tests

To more accurately evaluate the effect of carbon nanotubes on the elastic behavior, a series of nanoindentation (load and displacement sensing) tests were performed with a Berkovich indentor (a three-sided pyramid) [16]. The area calibration factor for the indenting tip as a function of depth of indentation was obtained using the procedure of Oliver and Pharr, and modulus as a function of depth of indentation was obtained using continuous stiffness measurements [17]. As shown in Figure 4.4, constant loading rate test sequence was used that included ramping up the indentation load to a target value of 100 mN at a constant loading rate (500 μN/s and 1000 μN/s), maintaining the peak load constant for 100 s, and unloading to 90% of the peak load. Creep is expected for these materials, and holding the load constant for a period of time prior to unloading allows for dissipation of creep displacements. Since the mechanical properties of polymer based

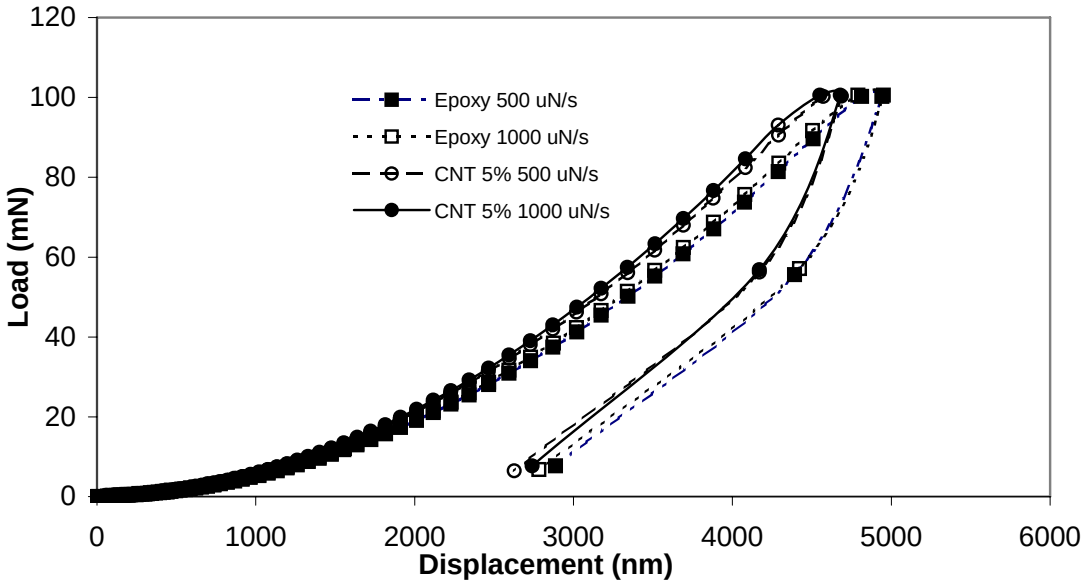

Figure 4.4: Load-Displacement relationship used for Nano-Indentation

composites are significantly affected by loading rate, the effects of time on Young's modulus values were also determined. Figure 4.4 (average load versus displacement for ten indents) indicates that all specimens show considerable amount of creep strain at the peak load.

The continuous stiffness method (CSM) was used during the loading segment with a sinusoidal displacement of 2 nm at 45 Hz. Ten indents were made in each of the samples at the two loading rates. Figure 4.5 shows the variation of average modulus for depth of indentation varying from 2 to 5 μm along with error bars corresponding to one standard deviation for two loading rates. It can be concluded that the loading rate effect on interpreted modulus was minimal and a constant value across the depth was obtained

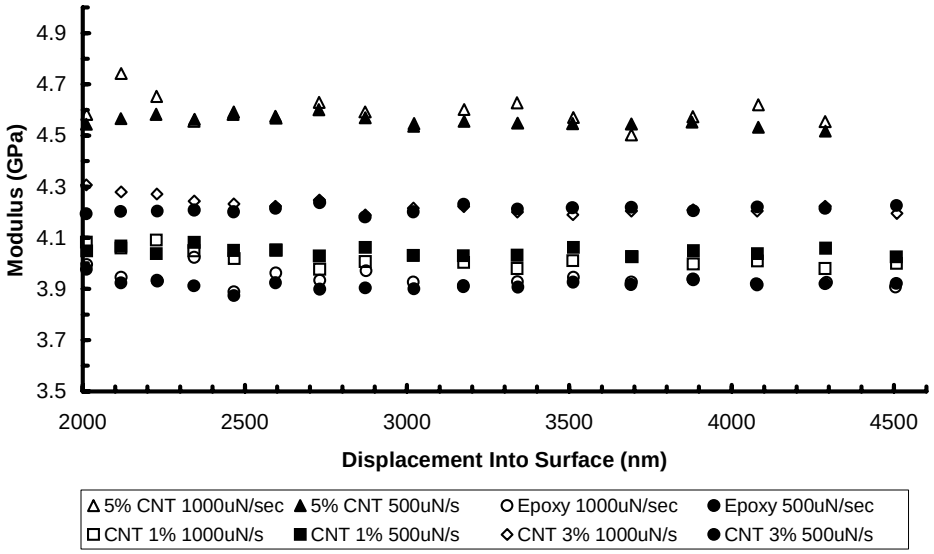

Figure 4.5: Modulus versus Depth of Indentation for varying SWCNT content and loading rate.

for all the samples. The instrumented indentation testing shows a consistent increase in average modulus value as a function of purified single wall carbon nanotube content as shown in Figure 4.6 (similar results were also obtained for hardness). This increase could not be observed from tensile test data on dog bone specimens shown earlier and is probably due to poor resolution in the measurement of small strains, and, more importantly, the nature of the test (tensile) on the compliant composite material, which is further addressed later in the paper.

Figure 4.7 shows scanning electron microscope (SEM) images of the fracture surface of a 5% SWCNT composite specimen at the end of tensile test at two magnifications. It can be concluded that the specimen preparation procedure used for

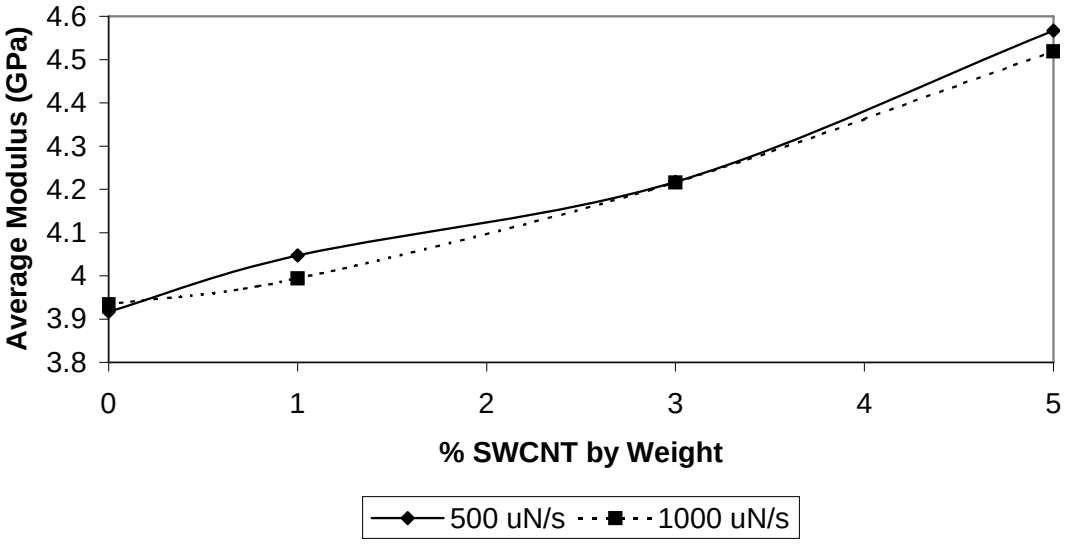

Figure 4.6: Modulus increase with increasing SWCNT content

a

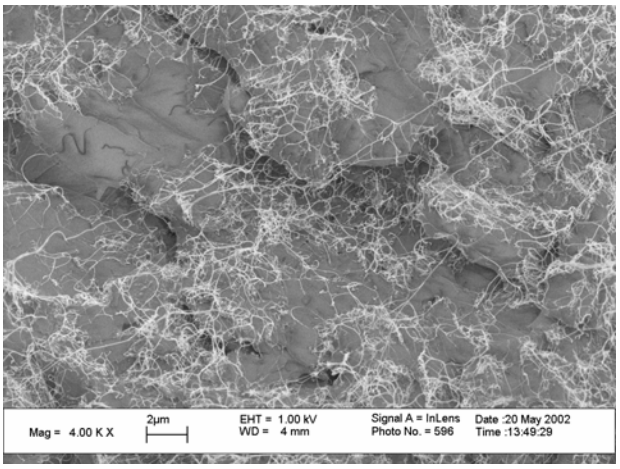

b

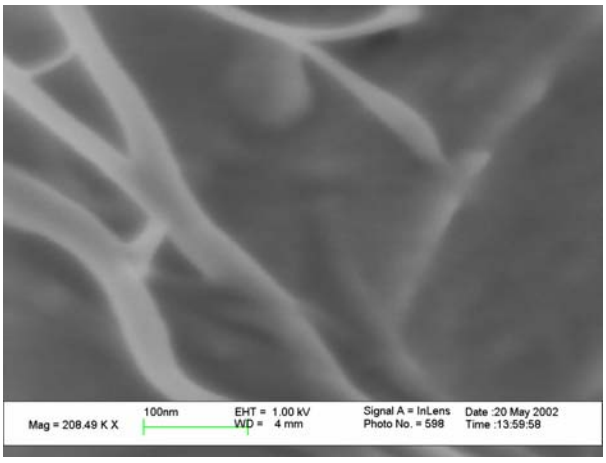

Figure 4.7: SEM images of 5%SWCNT composite (a) small magnification, (b) large magnification.

making these hybrid materials is reasonable given the good dispersion of the nanotubes. The SEM from higher magnification images seem to indicate that nanoropes, typically composed of 10–20 SWCNTs, are the smallest bundles (nanoropes) formed during the mixing procedure due to very high Van der Waals forces on individual tubes. Despite the good sonication and mixing procedures used in this research, it was difficult to obtain complete dispersion of individual tubes in a solution form, avoiding the rope/bundle formation prior to casting the hybrid materials. If complete dispersion is possible (using novel methods such as layer-by-layer assembly or polymer wrapping of nanotubes or chemical functionalization), then the morphology will indicate rodlike formation for these tubes or ropes [18].

Figure 4.7 also shows that many of these long and intertwined nanoropes were pulled out of epoxy matrix during the application of shear stress due to poor interface friction behavior. If one were to use a modulus of 1000 GPa for individual SWCNT or a straight bundle/nanorope, then results shown in Figures 4.5 and 4.6 could be surprising at a first glance. Considering the fact that the nanoropes may have to stretch before the actual load transfer from the matrix even with good interface shear strength, relatively large strains to failure for individual straight nanotubes or nanoropes (5–6%), and brittle behavior of nanocomposite, the actual contribution from nanotube to the failure tensile strength can be justified to be small as found in this research.

In tension tests, the modulus did not appear to change noticeably with the addition of nanotubes and could be due to the following. SEM pictures (such as the ones shown in Figure 4.7) indicate that 10–20 nanotubes were bundled together to form nanoropes in the matrix prior to setting of epoxy. Due to relatively high viscosity, it is likely that only peripheral tubes bonded to polymers. Also, during a tensile test, load transfer from matrix occurred only in the peripheral tube, and inner tubes may have undergone simultaneous slippage. In compression, buckling of nanoropes is likely, and slippage is minimized due to the geometrical constraint [19]. The noticeable improvements of modulus observed in nanoindentation testing could be due to both the complex stress path followed in determining the modulus that may include significant compressive loading and local confining pressure provided by a large volume of SWCNT in the probing area, resulting in a local stiffening of polymer matrix [20]. Recent micro-Raman spectroscopy results also suggest that specimens in tension show a shift of the wave number corresponding to only one tenth of that observed for identical specimens in hydrostatic compression and further supports our data [21,22].

CONCLUSION

In summary, the mechanical property changes due to SWCNT were evaluated for varying weight fraction (1– 5%). SEM images showed good level of dispersion of nanoropes throughout the epoxy matrix. Failure strength from tensile tests on dog bone specimens did not show significant differences and strain to failure decreased, indicating the brittle nature of the composites. Initial stiffness values (corresponding to modulus) from the stress–strain data of tensile tests showed little difference, confirming the

slippage of nanotubes within a nanorope undergoing tension. Instrumented indentation testing revealed a steady and modest increase of modulus and hardness as a function of SWCNT content and could be used as a routine tool for evaluating mechanical properties of new polymer nanocomposites (using a small sample volume) with carbon nanotubes as fillers/ reinforcement. It is hypothesized that significant strength and modulus increases can be obtained by improving the morphology of long nanobundles/nanoropes to be more rodlike in the epoxy matrix with a preferential alignment along the major principal stress direction.

REFERENCES

1. Kroto, H.W.; Heath, J.R.; O'Brien, S.C.; Curl, R.F.; and Smalley. R.E., *"C60 Buckminsterfullerene"*, Nature, 1985, 318, 162-163.
2. Iijima, S., *"Helical microtubles of graphitic carbons"*, Nature, 1991, 354, 56-58.
3. Iijima, S. and Ichihashi, T., *"Single-shell carbon nanotubes of 1-nm diameter"*, Nature, 1993, 363, 603-605.
4. Bethune, D.S.; Kiang, C.H.; Devries, M.S.; Gorman, G.; Savoy, R.; Vazquez, J.; and Beyers, R., *"Cobalt-catalysed growth of carbon nanotubes with single-atomic-layer walls"*, Nature, 1993, 363, 605-607.
5. De Heer, W.A.; Châtelain, A.; Ugarte, D., *"A Carbon Nanotube Field-Emission Electron Source"*, Science, 1995, 270(5239), 1179-1180.
6. Dai, H.; Wong, E.W.; and Lieber, C.M., *"Probing Electrical Transport in Nanomaterials: Conductivity of Individual Carbon Nanotubes"*, Science, 1996, 272(5261), 523 – 526.

7. Collins, P.G. and Avouris, P. "*Nanotubes for Electronics*", Scientific American, 2000, 283(6), 62.

8. Lourie, O.; Wagner, H.D.; Zhang, Y.; and Iijima, S., "*Dependence of elastic properties on morphology in single-wall carbon nanotubes"*, Advanced Material, 1999, 11(11), 931-934.

9. Hostenson, E. T.; Ren, Z.; Chou, T.-W., **"***Advances in the science and technology of carbon nanotubes and their composites: a review"*, Composites Science and Technology, 2001, 61(13), 1899-1912.

10. Yu, M. –F.; Lourie, O.; Dyer, M. J.; Moloni, K.; Kelly, T.F.; Ruoff, R.S., "*Strength and Breaking Mechanism of Multiwalled Carbon Nanotubes Under Tensile Load"*, Science, 2000, 287(5453), 637-640.

11. Yu, M.F.; Flies, B.S.; Arepalli, S.; and Ruoff, R.S., "*Tensile loading of ropes of single wall carbon nanotubes and their mechanical properties"*, Physical Review Letters, 2000, 84(24), 5552-5555.

12. Xie, S.; Li, W.; Pan, Z.; Chang, B.; Sun, L., "*Carbon nanotube arrays"*, Materials Science & Engineering, A: Structural Materials: Properties, Microstructure and Processing, 2000, A286(1), 11-15.

13. Cornwell, C. F.; Wille, L. T., "*Elastic properties of single-walled carbon nanotubes in compression"*, Solid State Communications, 1997, 101(8), 555-558.

14. Guo, T.; Nikolaev, P.; Thess, A.; Colbert, D. T.; Smalley, R. E., "*Catalytic growth of single-walled nanotubes by laser vaporization"*, Chemical Physics Letters, 1995, 243(1,2), 49-54.

15. Sandler, J.; Shaffer, M. S. P.; Prasse, T.; Bauhofer, W.; Schulte, K.; Windle, A. H., *"Development of a dispersion process for carbon nanotubes in an epoxy matrix and the resulting electrical properties"*, Polymer, 1999, 40(21), 5967-5971.

16. Hay, J.L. and Pharr, G.M., *ASM Handbook 8* (ASM International, OH, 2000) p. 232.

17. Oliver, W. C. and Pharr, G. M., *"An improved technique for determining hardness and elastic modulus using load and displacement sensing indentation experiments"*, Journal of Materials Research, 1992, 7(6), 1564-83.

18. Mamedov, A. A.; Kotov, N. A.; Prato, M.; Guldi, D.M.; Wicksted, J. P.; Hirsch, A., *"Molecular design of strong single-wall carbon nanotube/polyelectrolyte multilayer composites"*, Nature Materials, 2002, 1(3), 190-194.

19. Schadler, L. S.; Giannaris, S. C.; Ajayan, P. M., *"Load transfer in carbon nanotube epoxy composites"*, Applied Physics Letters, 1998, 73(26), 3842-3844.

20. Thostenson, E. T.; Li, W. Z.; Wang, D. Z.; Ren, Z. F.; Chou, T. W., *"Carbon nanotube/carbon fiber hybrid multiscale composites"*, Journal of Applied Physics, 2002, 91(9), 6034-6037.

21. Ajayan, P. M.; Schadler, L.S.; Giannaris, C.; Rubio, A., *"Single-walled carbon nanotube-polymer composites: strength and weakness"*, Advanced Materials, 2000, 12(10), 750-753.

22. Hadjiev, V. G.; Iliev, M. N.; Arepalli, S.; Nikolaev, P.; Files, B. S., *"Raman scattering test of single-wall carbon nanotube composites"*, Applied Physics Letters, 2001, 78(21), 3193-3195.

PART 5: NANOINDENTATION TESTING FOR EVALUATING MODULUS AND HARDNESS OF SINGLE-WALLED CARBON NANOTUBE REINFORCED EPOXY COMPOSITES

This part is a slightly revised version of a paper with the same title published in the Journal of Material Research in January 2004 by Amal K. Dutta, Dayakar Penumadu, and B.Files:

A.K.Dutta, D. Penumadu and B. Files “Nanoindentation testing for evaluating modulus and hardness of single-walled carbon nanotube–reinforced epoxy composites ” J. Mater Res., Vol. 19, No. 1, Jan 2004.

My primary contributions to this paper include (1) selection of the topic and development of the problem into a work relevant to my doctoral research study, (2) development of experimental setup, (3) most of the gathering and interpretation of literature, (4) performing most of the laboratory experiments, (5) interpretation and analysis of test results, (6) most of the writing.

ABSTRACT

Instrumented indentation testing was used to evaluate the changes in mechanical properties of single-walled carbon nanotube composite specimens with varying weight percentage (0, 0.1, 0.5, and 1.0 wt%) of nanotubes using a low-viscosity liquid epoxy resin. The nanotubes were prepared using laser ablation technique. Reference tensile tests were also performed on the same samples, and relevant comparisons with indentation results were made. The variations in modulus and hardness obtained using nanoindentation (considering time effects) showed quantifiable differences between the various composite specimens, but differed from tensile test data. The small changes in the observed stiffness and breaking strength of carbon nanotube composites was due to the formation of bundles, their curvy morphology, and microporosity in the specimens.

Interesting fluctuations obtained from the interpreted values of modulus with depth of indentation is attributed to varying degrees of the local confining effect of nanotube bundles. Creep exponents for these nanocomposites were also evaluated and indicate considerable improvements.

INTRODUCTION

Since the discovery of carbon nanotubes in 1991 by Iijima [1] and subsequent observations related to their unique mechanical and electrical properties, an extensive research in the field of blended carbon–epoxy nanocomposites has been initiated. A comprehensive review on the manufacturing process and mechanical and electrical properties of nanotubes and nanocomposites can be found in recent literature [2, 3]. The characteristic flexural properties and hardness dependency of multiwalled nanotube–epoxy composites with varying weight fraction on carbon nanotube has been studied by Lau et al. [4]. Allaoui et al. [5] have also reported the effect on mechanical and electrical properties of multiwalled carbon nanotube–epoxy composite with different weight percentages. In these studies, increase in elastic modulus was reported as a function of increased weight percentage of carbon nanotubes in the composites. Haggenmueller et al. [6] used solvent casting and melt mixing to disperse single-walled carbon nanotube (SWNT) material in poly (methyl methacrylate) films and showed increase in elastic modulus and yield strength with increasing loading of nanotubes and draw ratio. Ajayan et al. [7] suggested that the most effective ways of strengthening nanotube-reinforced epoxy materials include breaking bundles into individual tube fragments and dispersing these segments in the matrix and cross-linking the tubes within bundles via irradiation or

chemical treatments to increase rigidity and reduce tube slippage. The load transfer mechanism was studied for multiwalled carbon nanotube–epoxy composites by Schadler et al. [8] and found that the compression modulus is higher than the tensile modulus, indicating that the load transfer to the nanotubes in composite is higher in compression and was confirmed using the shift of Raman peak position with amplitude of strain during compression and tension. The mechanical properties of the multiwalled nanotube composites have been observed based on the tensile test methods, where macrolevel stress–transfer mechanism was being studied without the ability to evaluate nano- to microlevel behavior of nanotube bundle interactions with epoxy. It is thus important to understand the mechanical properties at microlevel, giving due emphasis on the nature of property changes with depth for the composite material. Penumadu et al. [9] recently presented the results on mechanical properties of blended SWNTs using nanotubes prepared at Rice University. The individual SWNTs used in this research were prepared from laser ablation technique and were used for preparing three types of hybrid material containing 1%, 3%, and 5% by weight of SWNT using compression mold and were evaluated against the pure epoxy sample. Using nanoindentation, the corresponding variations in modulus and hardness were determined and this study has reported quantifiable, but modest increases with increase in weight percentage of SWNT.

In this paper, we extend this study by using composite specimens made using cast molding technique (instead of compression molds used in the prior study) and SWNTs obtained using a modified laser ablation process. In addition, experiments were designed to study the creep behavior of these viscoelastic materials. The SWNTs were prepared by

a laser ablation technique developed at NASA Johnson Space Center (JSC) and purified using a custom procedure that takes approximately 2 weeks for its completion. The entire purification process takes approximately 2 weeks to complete and results in a yield rate of 30%. These purified nanotubes were mixed with epoxy at 0.1%, 0.5%, and 1.0% weight percentage. Considering time effects, the depth-dependent variation of elastic modulus and hardness was studied using nanoindentation technique, and the observed changes were rationalized considering tensile test data on dog bone specimens.

SPECIMEN PREPARATION PROCEDURE

Blended composites comprising 0.1%, 0.5%, and 1% SWNTs mixed in epoxy resin (epichlorohydrin and bisphenol F) were prepared. Because of its compatibility with nanotubes, long gel time for mixing and degassing, and low viscosity, commercially available EPON Resin 862 was used with Curing Agent W, available from Resolution Performance Products (www. resins.com) (Houston, TX). To minimize phase segregation during the preparation of polymer composite material, the following specimen preparation approach was developed. (i) Sonicate nanotube solvent (acetone/toluene azeotrope: 1 h); (ii) add resin and catalyst (100:26.4 by weight); (iii) stir on a hot plate at 60 °C and remove; and (iv) degas in vacuum oven at 60 °C for 3.5 h, load the cast mold with material, cure the sample.

The modulus and hardness of the dog bone cast molded specimens were obtained from nanoindentation testing using NanoIndenter XP (MTS NanoInstruments, Oak Ridge, TN) (with a pyramid-shaped Berkovich indenter) on cross-sectional and longitudinal

portions of the sample within the gage length. Indentation creep tests were also performed for determining the effect of increased nanotube content on the time-dependent deformation behavior of these nanocomposites.

EXPERIMENTAL PROCEDURE AND RESULTS

Using the procedures of ASTM Standard D-638, deformation-controlled tensile tests were performed on the dog bone specimens using an MTS-SinTech 20/G (MTS Systems Corporation, Eden Prairie, MN) materials testing system. Typically, three tests were repeated for each carbon nanotube content for tensile testing. The initial portion of the axial stress–axial strain curves were quite linear over a wide range of strain values, and the linear regression technique provided a good estimate of the modulus values. Table 5.1 summarizes the results from one set of such tensile test data. It is evident that with increasing nanotube content, the strain to failure (breaking strain) decreased substantially, indicating the brittle nature of nanotube composite specimens. The tensile strength (peak stress) decreased with increasing SWNT content and is probably due to microdefects resulting from blended composites during cast molding technique. Because of the inherent tendency for strain localizations to occur in a tensile test, the stress to failure in these specimens will be controlled by weak zone(s) in the gauge length that will initiate premature failure. The Young's modulus values showed a decrease for 0.1% and 0.5% specimens and showed a noticeable increase for 1.0% specimens. This data will be further discussed later in this paper in conjunction with the results from nanoindentation test data.

Table 5.1: Results from tensile test data.

SWCNT Content (%)	Failure Strain (%)	Peak Stress (MPa)	Modulua (GPa)
0.0	9.4	73.7	5.46
0.1	7.9	76.8	4.78
0.5	4.7	65.2	4.96
1.0	3.9	57.7	6.01

A series of 10 indentations were performed for each sample. The test began with an approach segment of the indenter to the surface of the nanocomposite specimen, followed by a load or creep segment. Because the samples were made with polymer matrix, which was a soft material, a smaller factor in the change of stiffness (a factor of 2 to 4 in this research) was used to determine the contact to the surface prior to initiating indentation load segment. In the load segment, the indent was made at a constant strain rate of 0.05/s with the load increasing until a maximum value of 100,000 μN. The constant strain rate was maintained by controlling the ratio of the applied load increment to the current load value to a constant target value of 0.05. The third segment of the experiment was a hold segment for 10 s followed by an unload segment that was load-controlled with an unloading rate equal to 70% of the loading rate. The unloading was continued until 80% of the maximum load was removed. A second hold segment was applied with a data logging delay of 2 s and number of hold points equal to 50. The experiment was then completed with a final unload segment in which all of the applied load was removed.

A typical load versus displacement curve for ten in-dentations in constant strain rate test for 1% SWNT on a cross-sectional part of the sample is shown in Figure 5.1. Figure 5.1 indicates a considerable amount of creep strain at the peak load for the specimen. It is thus important to normalize loading rate effects to evaluate the mechanical properties of these nanocomposite specimens. In Figure 5.2, the comparative nature of the average load versus displacement curves (only loading segment considered here) for different samples on the cross-sectional part of the gauge length of dog bone specimen is shown. It is seen from Figure 5.2 that as the weight percentage of nanotubes increased, greater load requirement for reaching a corresponding displacement was noted and shows modest benefits of reinforcing with single-walled nanotubes.

The elastic modulus and the hardness values were interpreted from the measured data based on the composite response of the indenter and the material using the procedure of Oliver and Pharr [10]. Figure 5.3 shows the variation of the elastic modulus with the depth of indentation on the cross-sectional part of the gauge length of these composite specimens for varying SWNT content. Each curve in Figure 5.3 represents an average value of modulus from ten indents. The authors chose to provide modulus (and hardness) values in this paper for indentation depths larger than 500 nm, due to higher confidence in determining true cross-sectional area of the indenting tip at corresponding depths. It is seen that for all depths, the average modulus increased with larger percentage (1%) of

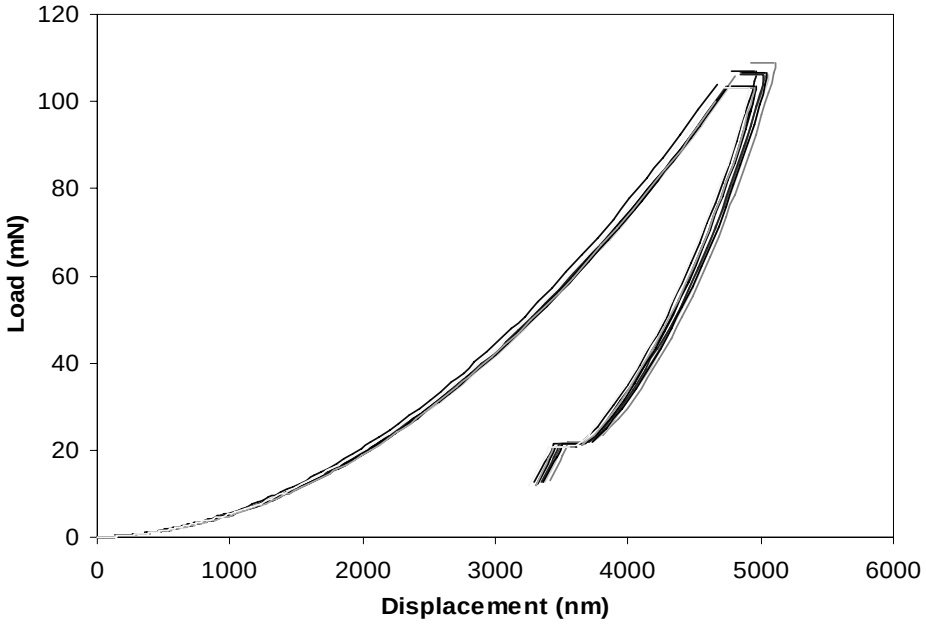

Figure 5.1: Load versus deformation for 1% by weight SWNT-reinforced epoxy composites.

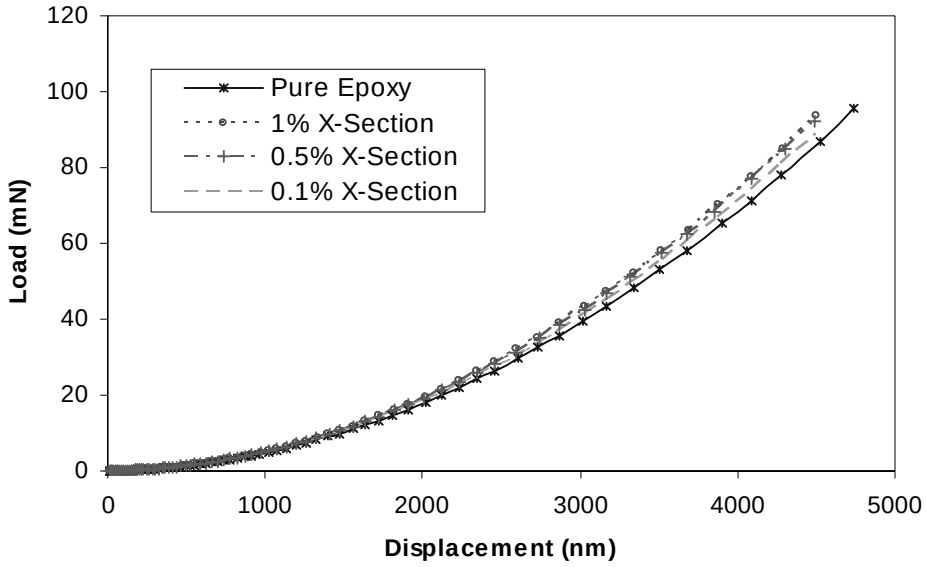

Figure 5.2: Effect of increasing carbon nanotube content on the load versus deformation behavior (mean values from 10 indents).

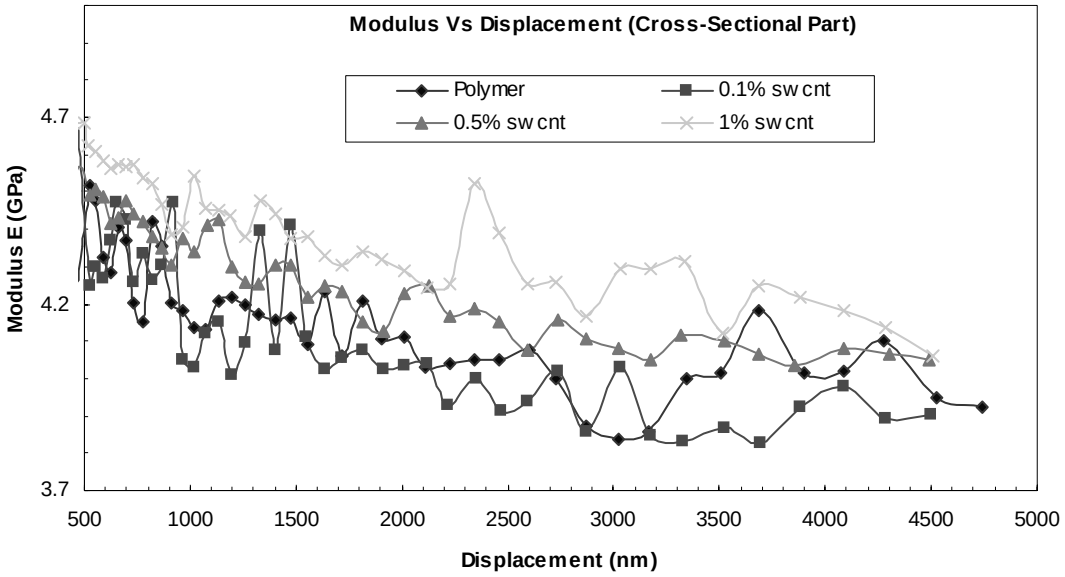

Figure 5.3: Effect of increasing carbon nanotube content on mean modulus values with depth of indentation

SWNTs. When the nanotube content was small (0.1%), the measured modulus of pure epoxy sample was slightly higher. It is evident from Figure 5.3 that at certain depths of indents (e.g., around 1500 nm), significant increase was observed for 0.1% SWNT sample. This is speculated to be due to larger local vol% of nanotubes in that region (depth wise), and is probably an indication of poor dispersion of individual tubes. However, in general, for higher weight percentage of nanotubes (0.5% and 1.0%), a modest increase in indentation modulus was observed and is not consistent with average modulus observed from tensile test data (Table 5.1). An important trend observed from instrumented indentation testing is that with increase in depth of indentation, average modulus values consistently decreased for all samples, as noted in Figure 5.3. The decrease in modulus with increased depth of indentation can be due to the segregation of

nanotubes to the surface of the specimen in the mold during the specimen preparation process used in this research and needs to be further evaluated. The variation of hardness function of depth is shown in Figure 5.4. A consistent and notable (but modest) increase in hardness values were observed with the addition of nanotubes and is associated with the increased confining effect provided by the nanotube bundles to resist load. Hardness values also decrease with depth of indentation. It is important to note that the nanoindentation load–displacement data was analyzed according to Oliver and Pharr [10] to determine both the nanoindentation contact area and the hardness values. This method does not account for pile-up (or sink-in), which can occur for soft composite specimens. Figure 5.5 shows a typical optical image of an indent for current samples and does not indicate significant pile-up or sink-in.

An experimental difficulty with the measurement of hardness and modulus values for time-dependent polymer nanocomposite materials using instrumented indentation is that the creep aspect of deformation behavior can increase the indentation displacement even during an unloading segment. This results in artificially high contact stiffness values affecting the modulus and hardness values. Because of the expected creep for these materials, loading segments used in the previous section (Figures 5.3 and 5.4) included holding the load constant for a while prior to unloading, allowing for partial dissipation of creep displacements. The authors also attempted to evaluate the creep behavior of these nanocomposites to evaluate the associated changes with the use of SWNTs at constant room temperature.

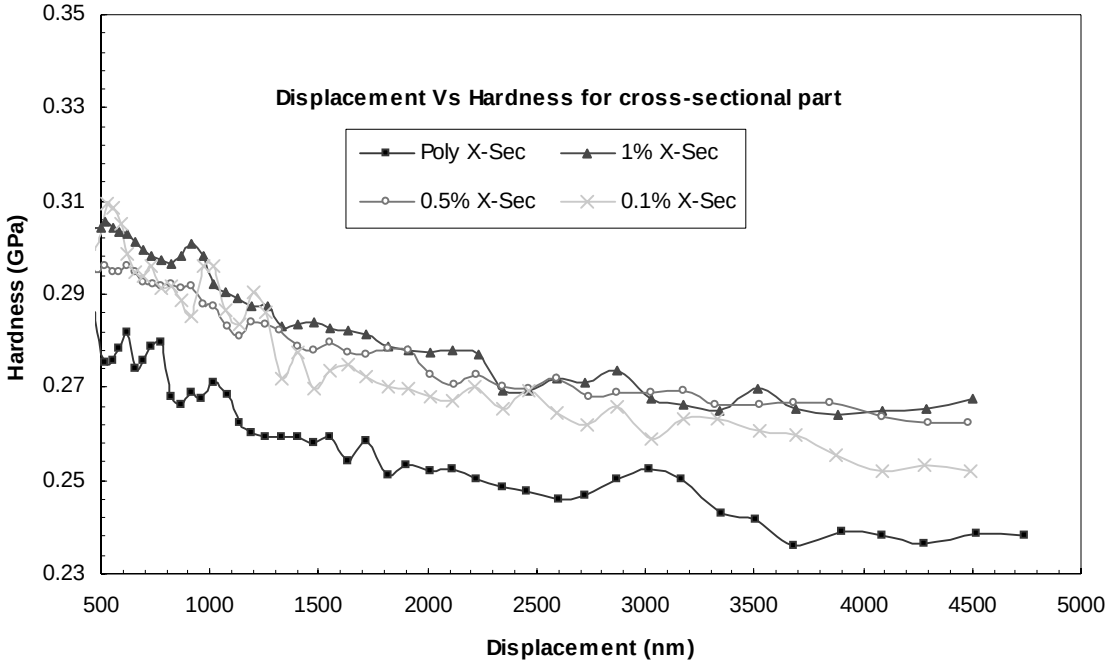

Figure 5.4: Effect of increasing SWNT content on mean hardness values with depth of indentation

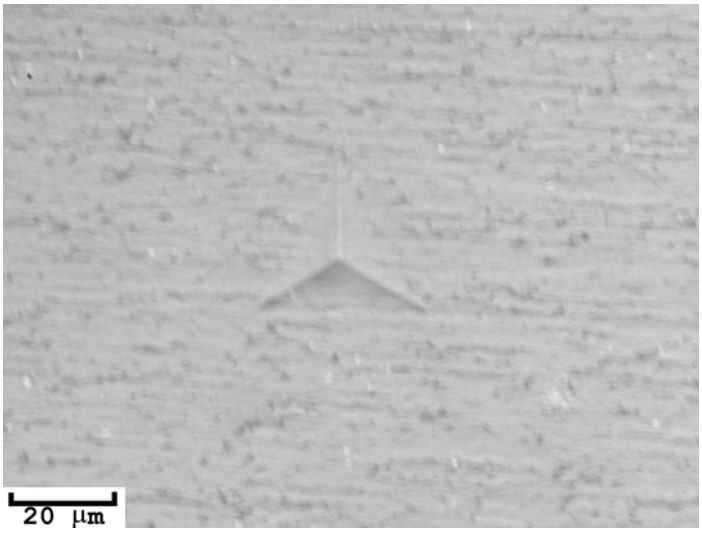

Figure 5.5: Typical indent shape in epoxy specimen showing minimal pile-up or sink-in.

CREEP BEHAVIOR OF NANOTUBE-REINFORCED EPOXY COMPOSITES

It has been well documented in the literature that creep behavior of many materials can be approximated with a power law creep equation with a constant stress exponent, except at low temperatures or high stresses. The power law states that the creep rate, ε, depends both upon the applied stress and a strength factor. Under constant stress, the variation of the strength factor would then affect the creep rate. At a constant temperature, rate of change of creep strain (ε_c) can be approximated by the following relationship:

$$\frac{d}{dt}\left(\varepsilon_c\right) = K\left[\frac{\sigma}{\tau}\right]^{\eta} \tag{5.1}$$

The exponent, η, is one of the parameters of interest that is often evaluated from creep experiments (K is a material constant and σ is the stress amplitude corresponding to steady-state conditions) for modeling timedependent mechanical properties. Measuring the creep properties from depth-sensing indentation under condition of constant load was proposed by Pollock et al. [11] and made an approximation that the strain rate should scale as below:

$$\frac{d}{dt}\left(\varepsilon_c\right) = k\frac{\left(\frac{dh}{dt}\right)}{h}, \tag{5.2}$$

where k is a geometric constant and h is the instantaneous displacement of the indenter. Mayo et al. [12] developed a similar technique using nanoindentation. The experimental procedure involved loading the indenter at a high loading rate and then holding the load on the indenter constant and monitoring the displacement of the indenter as a function of

time. Due to the change in contact area with varying depth of contact, hardness or mean stress changes as the test proceeds. It is important to realize that the time-dependent mechanical properties of materials measured by different techniques (uniaxial versus indentation creep exponents) may be different due to the following: (i) steady-state versus transient behavior; (ii) uniformity of stress distribution (homogeneous versus radial); (iii) volume of material being deformed (constant for uniaxial and continually increasing for indentation testing; and (iv) geometry of the material is controlled by the properties of material (modulus and hardness) in indentation testing, whereas it is fixed by a given choice of specimen shape (cylinder or a dog bone) in tensile/ compression testing.

For conventional creep tests performed in uniaxial tension at constant temperature, the steady-state creep rate is often related to stress using a stress exponent that is a material property. An equivalent expression for instrumented indentation creep test relates the indentation strain rate (normalized rate of indentation displacement) with hardness through a corresponding creep exponent. This data can be evaluated by determining the variation of the displacement of a Berkovich indenter as a function of time at constant load. The following testing sequence was thus applied using NanoIndenter XP for studying creep properties of these samples. The indent was made at a constant loading rate of 5 mN/s (i.e., under load control) with the load increasing until a peak value of 50 mN was applied to the indenter. This was followed by a hold segment with a data logging delay of 10 s for a total holding time limit of 1000 s The unload segment was load controlled with a constant unloading rate of 5 mN/s. The unloading continued until 90% of the peak load was removed followed by a hold segment for 1000 s

and complete unloading. Figure 5.6 shows typical results from nanoindentation creep tests. These tests were performed twice for each of the nanocomposite materials, and very good repeatability was obtained.

A way of quantifying the hardness-based creep parameter is to use the data from constant load (at 50 mN) segment portion and plot the variation of indentation strain rate versus hardness on log–log scale to obtain the creep parameter from the slope of best-fit linear regression using associated displacements under hold segment. Figure 5.7 shows the comparison of displacement–time data under constant load and indicates that with an increase in nanotube content, the resulting creep displacements decreased noticeably. This indicates the beneficial effects of reduced creep deformation and its rate (Figure 5.7) with increased weight percentage of SWNT. The displacement rate during hold period under constant load was observed to be high for the initial stage of hold segment and decreased with increase in hold time. By differentiating the displacement versus time data, the displacement rate of the indenter can be obtained continuously during the constant load hold period.

The indentation strain rate corresponds to the ratio of the instantaneous descent rate of the indenter by the displacement at that point in time. Hardness is obtained by dividing the load by the instantaneous contact area. A plot of indentation strain rate versus hardness (analogous to strain-rate versus stress) was obtained from data corresponding to the hold segment as shown in Figure 5.8. The creep exponent values increased with an increase in the amount of carbon nanotubes as shown in Figure 5.8.

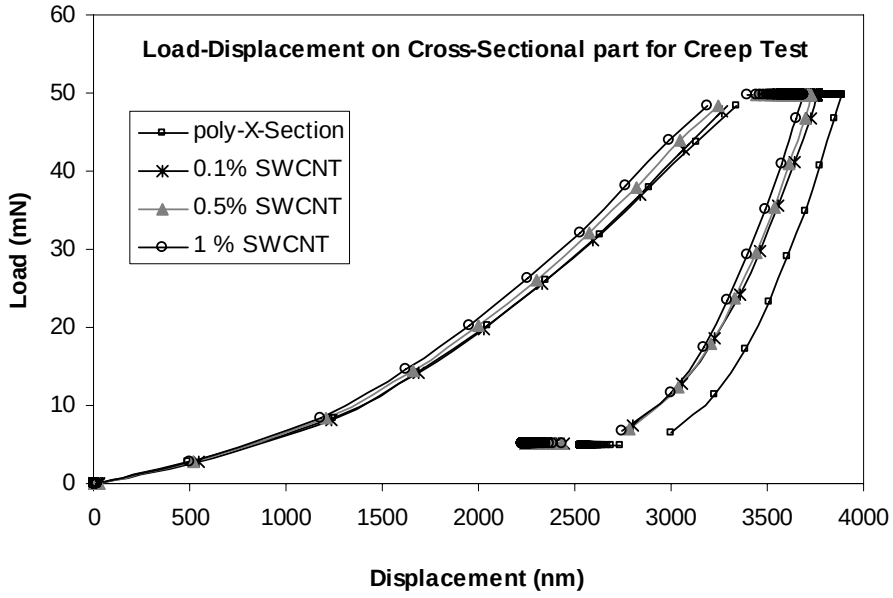

Figure 5.6: Results from indentation creep tests showing the influence of increasing SWNT on time-dependent deformation properties.

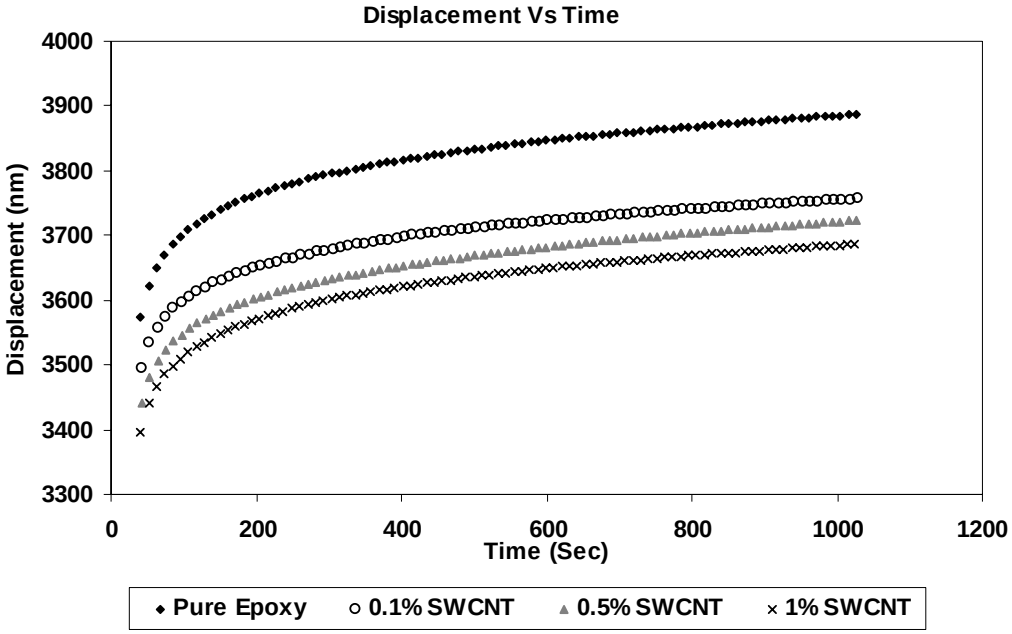

Figure 5.7: Variation of creep displacement under constant load of 50 mN indicates the improvement in time-dependent deformation properties with increasing SWNT.

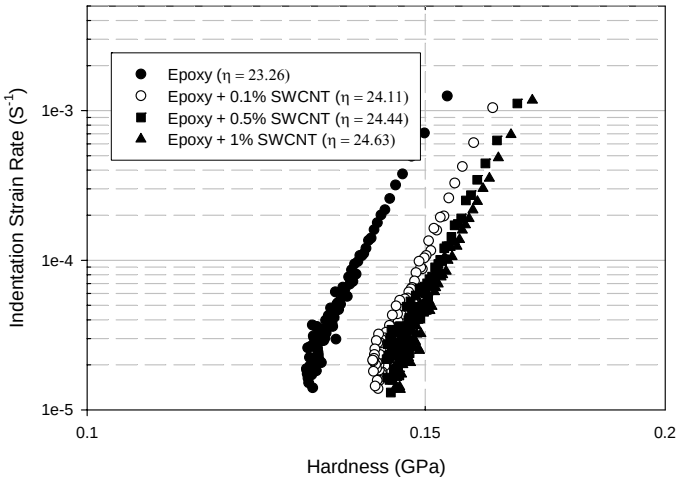

Figure 5.8: Variation of indentation strain rate with hardness for increasing carbon nanotube content.

These curves also indicate that for a given hardness value (analogy with stress amplitude), polymer samples without nanotube reinforcement show highest strain rate. It is also interesting to note that the exponent values are almost constant for the entire range of strain rates observed during the creep experiments.

The variation in the modulus and reduction in strength observed in macroscopic tensile test data with increasing weight content of SWNT may partially be explained by considering the electron micrographs of these specimens. As an example, Figure 5.9 shows digital scanning electron micrographs from a location of the broken specimen of polymer with 0.5% SWNT over its gauge length. Defects associated with microvoids during specimen preparation and poor dispersion of individual nanotubes is evident and may explain some of the inconsistencies associated with the effect of increased nanotube content on the modulus values obtained from tensile tests. However, instrumented

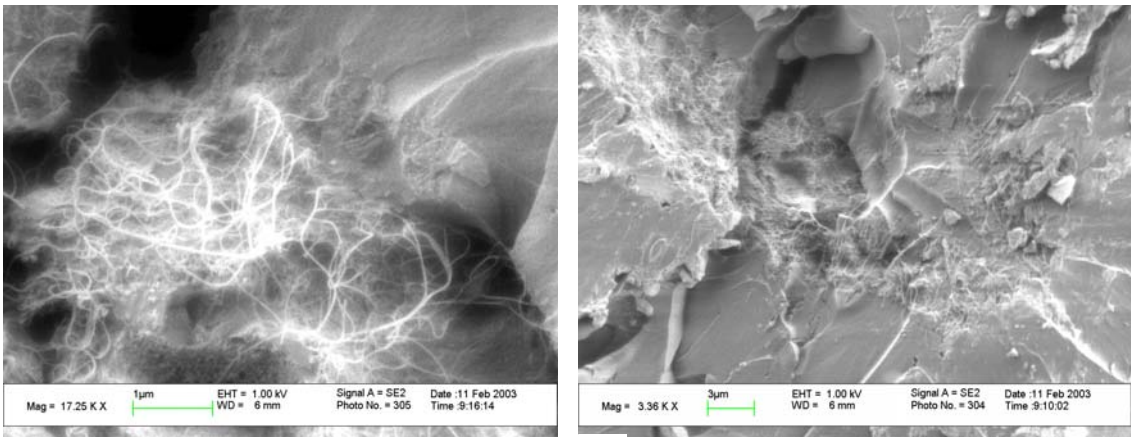

A B

Figure 5.9: SEM images on the broken (by tensile force) surface of 0.5% SWNT composite. Sample: (A) magnification = 17,250; (B) magnification = 3350.

indentation tests did not reveal such decrease in modulus values and is probably due to the small representative volume of the sample being tested. The consistent and modest increase of hardness is potentially due to increased confinement provided by the nanotubes (or bundles). If one were to take an average value of modulus and hardness for all the indentation depths, the following is concluded. Epoxy samples with 1% SWNT content show an increase of 4% in modulus when compared to the pure epoxy sample. Similarly, an increase of 5.7% in hardness is observed for composites with 1% SWNT content. Recent work of Biercuk et al. [13] showed that the hardness of SWNT–epoxy composites increased linearly from 0.4 GPa for the pristine epoxy to 1.4 GPa at 2% nanotube content. The sample preparation procedure in their research involved dispersing carbon nanotubes ultrasonically for very long times (48 h) in an organic solvent. The objective of this paper was to present the potential of using instrumented indentation technique for evaluating time-dependent mechanical properties of polymer-based single-walled carbon nanotube composites. It is envisioned that the current research related to

preparing functional SWNTs with improved interface shear properties, straight morphology (instead of being curved tubes), and good dispersion should dramatically improve the mechanical properties. Nanoindentation testing offers a unique opportunity to evaluate the changes in mechanical properties of these composite materials using a very small specimen volume, making the exploratory research stage of these novel materials cost effective.

SUMMARY AND CONCLUSIONS

In the current work, the mechanical property changes of single-walled carbon nanotube–based epoxy composites were studied for varied weight percentages of nanotubes (0.1–1%). The following are concluded from this study:

(1) Instrumented indentation testing is a viable tool for evaluating the time-dependent mechanical properties of polymer composites made using SWNTs based on small sample volume. Differences in mechanical properties were observed when compared to the uniaxial tensile test data and is attributed to specimen inhomogenities and corresponding strain localizations. This may be due to the cast molding technique used in the current research, curved morphology of nanotubes, poor dispersion, and associated phase segregation.

(2) The change in modulus and hardness as a function of indentation depth on the composite samples was evaluated. Epoxy with 1% SWNT showed an average increase in the modulus value by 4% and hardness by 5% when compared to the pure polymer specimen using nanoindentation.

(3) The hardness and modulus values decreased with increasing indentation depth. A comparison of displacement–time data under constant load indicates that with an increase in nanotube content, the resulting creep displacements decreased noticeably. Creep exponents were evaluated from the plots of indentation strain rate versus hardness and showed a steady increase with increasing nanotube content. This indicates the beneficial effects of reduced creep deformation with increased weight percentage of SWNT.

REFERENCES

1. Iijima, S., **"***Helical microtubules of graphitic carbon"* Nature, 1991, 354(6348), 56-58.
2. Lau, K.-T.; and Hui, D., "*Effectiveness of using carbon nanotubes as nano-reinforcements for advanced composite structures"* Carbon, 2002, 40(9), 1605-1606.
3. Thostenson, E. T.; Ren, Z.; Chou, T.-W., "*Advances in the science and technology of carbon nanotubes and their composites: a review"*, Composites Science and Technology, 2001, 61(13), 1899-1912.
4. Lau, K.-T.; Shi, S.-Q.; Cheng, H.-M., "*Micro-mechanical properties and morphological observation on fracture surfaces of carbon nanotube composites pre-treated at different temperatures"*, Composites Science and Technology, 2003, 63(8), 1161-1164.

5. Allaoui, A.; Bai, S.; Cheng, H. M.; Bai, J. B., "*Mechanical and electrical properties of a MWNT/epoxy composite",* Composites Science and Technology, 2002, 62(15), 1993-1998.

6. Haggenmueller, R.; Gommans, H. H.; Rinzler, A. G.; Fischer, J. E.; Winey, K. I., " *Aligned single-wall carbon nanotubes in composites by melt processing methods",* Chemical Physics Letters, 2000, 330(3,4), 219-225.

7. Ajayan, P. M.; Schadler, L. S.; Giannaris, C.; Rubio, A., "*Single-walled carbon nanotube-polymer composites: strength and weakness",* Advanced Materials, 2000, 12(10), 750-753.

8. Schadler, L. S.; Giannaris, S. C.; Ajayan, P. M., "*Load transfer in carbon nanotube epoxy composites",* Applied Physics Letters, 1998, 73(26), 3842-3844.

9. Penumadu, D.; Dutta, A.; Pharr, G. M.; Files, B., "*Mechanical properties of blended single-wall carbon nanotube composites",* Journal of Materials Research, 2003, 18(8), 1849-1853.

10. Oliver, W. C.; Pharr, G. M., "*An improved technique for determining hardness and elastic modulus using load and displacement sensing indentation experiments",* Journal of Materials Research, 1992, 7(6), 1564-1583.

11. Pollock, H.M.; Maugis, D. and Barquins, M., "*Microindentation Tech. In Mat. Sci. & Eng.",* edited by P.J. Blau and R. Lawn ASTM 47 (Pittsburgh, PA, 1986).

12. Mayo, M. J.; Siegel, R. W.; Liao, Y. X.; Nix, W. D., "*Nanoindentation of nanocrystalline zinc oxide (ZnO)",* Journal of Materials Research, 1992,, 7(4), 973-979.

13. Biercuk, M. J.; Llaguno, M. C.; Radosavljevic, M.; Hyun, J. K.; Johnson, A. T.; Fischer, J. E. **"***Carbon nanotube composites for thermal management",* Applied Physics Letters, 2002, 80(15), 2767-2769.

PART 6: MECHANICAL BEHAVIOR OF INDIVIDUAL SAND PARTICLES USING NANOINDENTATION AND THE EFFECT OF STRESS LEVEL

This chapter is a slightly revised version of a paper with the same title to be submitted in Journal of Geotechnical Engineering by Amal K. Dutta and Dayakar Penumadu:

Dutta, A. K. and Penumadu, D. "Mechanical Behavior of Individual Sand Particles Using Nanoindentation and the Effect of Stress Level," Journal of Geotechnical Engineering, 2006.

My primary contributions to this paper include (1) developing experimental setup, (2) most of the gathering and interpretation of literature, (3) performing most of the laboratory experiments, (4) interpretation and analysis of test results, (5) most of the writing.

ABSTRACT

The mechanics of granular material is an important issue that governs many geotechnical engineering applications. Several studies exists that describe the complex deformation response for an aggregate of material and this study attempts to characterize the particle scale behavior accurately. In this paper, nanoindentation technique is used to study individual sand particles smaller than 1 mm. Appropriate experimental and interpretation procedures are developed to obtain hardness and modulus. The micromechanics associated with two types of silica sand (Ottawa and Q-Rok sand) having similar mineralogy and different morphology is studied. Confined compression tests are performed on their assemblage, and selected particles are characterized to study the effects of confining stress level on particle-scale response.

INTRODUCTION

To obtain comprehensive insight into the characteristics and behavior of granular materials, it is important to determine the relationship between the bulk assembly and individual particle properties of such materials. The tensile strength of the soil particles has been found to influence the macroscopic behavior of granular materials [1-3]. Macroscopic observations on granular materials are usually obtained using element testing and/or physical modeling. The engineering properties of materials and the effect of particle crushing on the stress-strain and strength behavior have been analyzed by Yamamuro and Lade [4-6]. The tensile strength of rock and single particle is measured indirectly [7] by compressing the particle between flat platens until failure occurs. McDowell & Amon [8] showed that for similar loading geometries, weibull statistics [9] can be applied to characterize soil particle strength. Nakata et al. [10, 11, 12] have demonstrated how the onset of particle damage at asperities can be linked with the onset of plastic yielding and showed that Weibull could be used to estimate failure probabilities of soil particles in triaxial specimens. There are several compilations of elastic moduli from single crystal study for a wide variety of materials/minerals available, notably those of Hearmon [13,14] in the Landolt-Bornstein tables, and Sumino and Anderson [15] (for crystalline materials), and of Bansal and Doremus [16] (for glasses). However, for measuring individual fine particle material strength, all these methods involves either theoretical measurements or drawing inferences from the bulk material properties. Until recently, equipment did not exist for accurately measuring the mechanical properties such as hardness, elastic modulus and creep properties of the individual particles. During the last decade, there have been revolutionary developments in the field of depth-sensing

nanoindentation technique, using which mechanical properties of small volumes of material can now be determined accurately [17,18]. In this technique, an indenter probe of appropriate geometry is placed in contact with the sample surface and then pushed into it. The resistance to indentation and the indentation depth are continuously monitored throughout the experiment, and by analyzing the load-displacement curve, both hardness and elastic modulus of the material can be measured directly and more precisely. Nanoindentation technique is now an accepted and proven technique for mechanical characterization of micro and nanoscale materials in a wide variety of disciplines [19-28].

Using depth sensing nanoindentation instrumentation technique, an attempt was made in this study to characterize the micromechanical properties including hardness, Young's modulus and time dependent creep parameters for individual granular sand particles. In addition authors use nanoindentation technique to evaluate the micromechanical property changes due to the applied stress for varying particle shape under confined conditions.

MATERIALS AND EXPERIMENTAL METHODS

Two types of silica sand (Ottawa sand and Q-Rok sand obtained from US Silica, Berkeley Springs, WV) having similar mineralogy with approximately 99.8% SiO_2 as per Product Data Sheets of U. S. Silica (Appendix A and Appendix B) and size but very different morphology, are used for studying the particle level mechanical properties. The single particle material properties of the sub-rounded Ottawa sand and sub-angular Q-Rok sand as per the study of McDowell and Bolton [29] and Nakata et al. [11] are shown

in Table 6.1. Jason et al. [30] recently has performed 1-D compression tests on these sand materials and studied the effect of specimen and particle properties on the crushing behavior of granular soils. Ottawa and Q-Rok sand that was used in their one dimensional compression tests were studied in this paper for evaluating the micromechanical properties of the individual sand particles using nanoindentation technique. Individual particles obtained from unstressed state and assembly that has been subjected to a confined compression stress of 100 MPa were analyzed to evaluate the change in mechanical properties with stress level at a single particle scale.

For indenting purposes, sand particles larger than 600 μm in diameter (particles retained on US standard sieve #30) were embedded in the polymer matrix. This study is first of its kind to use nanoindentation technique to study small particles individually. Details of specimen preparation are also included here because of the lack of such information in the published literature and its importance for obtaining reliable data.

The sample preparation procedure for nanoindentation measurements on individual sand particles consist of mounting the particles in a polymer matrix and polishing the surface to approximately 1 μm roughness. In the first stage of sample preparation, the raised surface of bottom plate and inside of the cylinder wall of BUEHLER SAMPL-KUP (Figure 6.1) was coated with release agent (Buehler Silicone Mold Release 20-3046) and few grains of specified sieve sized sand particles were placed on the raised surface. The cylindrical part of the SAMPL-KUP then slipped over the plate and the cold mounting material was poured into the cup. The mounting material

Table 6.1: Summary of Sand Properties

Sand	D_{50} (mm)	C_u [1]	C_c [2]	G_s [3]	Roundness [4]	Aspect ratio [5]	Fracture Strength [6] (Mpa)
Ottawa 20-30	0.74	1.06	0.98	2.64	0.43	1.22	12.8
Q-Rok	0.75	1.47	1.09	2.64	0.48	1.34	4.8

[1] $C_u = D_{60}/D_{10}$ (ASTM D2487-93), [2] $C_c = D_{30}^2/(D_{10}*D_{60})$ (ASTM D2487-93), [3] AASHTO T133,
[4]Roundness = Perimeter^2/4*p*A, [5]Aspect Ratio = Major axis/ Minor axis,
[6]Fracture Strength = Force at failure/diameter^2. (McDowell and Bolton 1998)

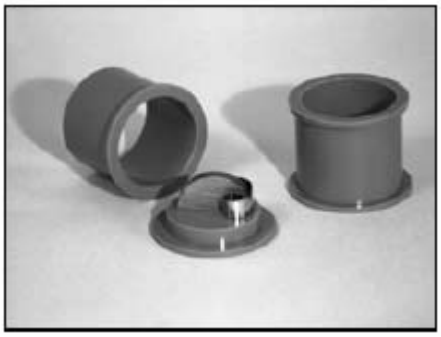

Figure 6.1: SAMPL-KUP Mounting Cups

(substrate) used consists of 5 parts by weight of No. 20-8130 BUEHLER EPOXICURE^{TM} RESIN to 1 part by weight of No. 20-8132 EPOXICURE^{TM} HARDNER. After curing (approximately 24 hours at room temperature) the plate was removed from the cylinder and the finished mold was taken out. In the next stage, the flat mold surface that consist the sand particles was grinded in two steps. In the first step, the specimen was grinded on a rotating wheel at 180 rpm by using a 45 micron metal bonded diamond disk (ULTRA-PREP Diamond Disks, Buehler Made) until a desired flat surface was achieved. In the second step the specimen was grinded with a 15 micron diamond disk. The sample was polished in three steps. The first polishing was made using a 9 micron diamond paste (METADI II, BUEHLER) on ULTRA-POL cloth with rotating wheel speed at 180 rpm. Mineral oil has been used during this polishing stage so as to keep the paste thin. The second step polishing was made with diamond paste (METADI II, BUEHLER) of size 3 micron on TEXMET 1000 cloth. The final polishing was performed on a napless cloth (TEXMET 1000) using a suspension that was made up of colloidal silica (MASTERMET II, Buehler) admixed with 30% Hydrogen Peroxide in the ratio of 5:1. The wheel speed throughout the polishing process was maintained at 180rpm.

Typical SEM (Scanning Electron Microscope) images of Ottawa and Q-Rok sand before crushing are shown in Figure 6.2. The sub-rounded nature of Ottawa sand and sub-angular shape of Q-Rok sand are clearly evident from these images. In addition, one can see the significant difference in surface texture. Figure 6.3 shows a typical epoxy specimen with embedded particle used for nanoindentation testing. The sand particles are

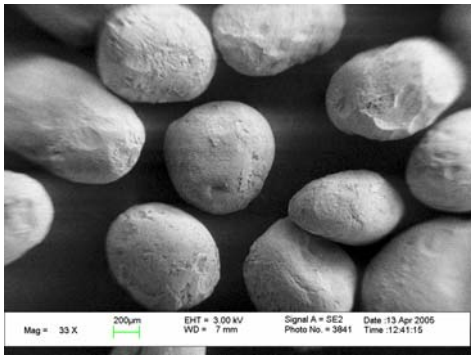

a

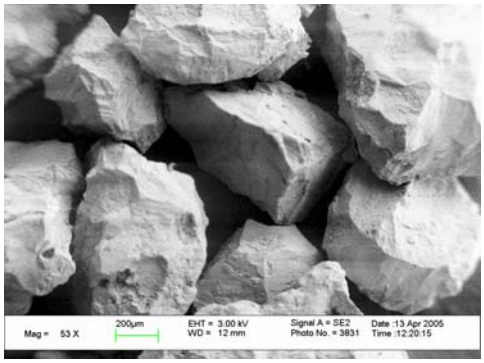

b

Figure 6.2: SEM image of (a) sub-rounded Ottawa sand and (b) sub-angular Q-Rok sand before applied stress.

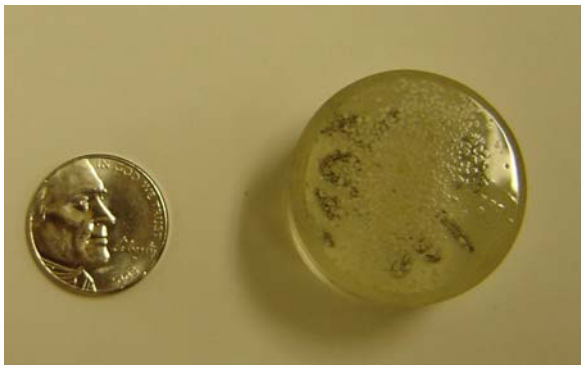

Figure 6.3: Typical sample specimen for nanoindentation on sand particles.

shown embedded here within the polymer matrix. Typical SEM images of sub-rounded Ottawa sand and sub-angular Q-Rok sand subjected to 100 MPa vertical stress after final polishing are shown in Figures 6.4a and 6.4b respectively. The particles are embedded within the polymer matrix whose average particle size is about 600 μm. The nanoindentation tests have been performed by Nanoindenter XP at Oak Ridge National Laboratory (ORNL).

To measure the elastic modulus and hardness of individual grains of Q-Rok and Ottawa sands before and after the applied 100 MPa stress, a series of nanoindentation (load and displacement sensing) tests were performed with a Berkovich indenter on individual sand grains. The area calibration factor for the indenting tip as a function of depth of indentation was obtained using the procedure of Oliver and Pharr [31]. Using continuous stiffness measurement (CSM) procedure, the elastic modulus was measured as a function of depth of indentation. The basic experiment in CSM begins with a slow surface approach mechanism, based on the measurements of load, displacement, and stiffness to identify carefully the point of first contact. The surface approach velocity was 10nm/s, with 2-nm oscillation in the harmonic displacement at a frequency of 45 Hz. Once the surface was detected, a constant loading rate test sequence was applied that includes ramping up the indentation load to a target value of 100 mN at a constant strain rate [$(dP/dt)/P$] of 0.05/s. Thus, the constant strain rate was maintained by controlling the ratio of the applied load increment to the current load value to a constant target value of 0.05. A hold segment for 10 s was applied at the peak load followed by an unload segment which was again load-controlled with an unloading rate equal to 70% of the

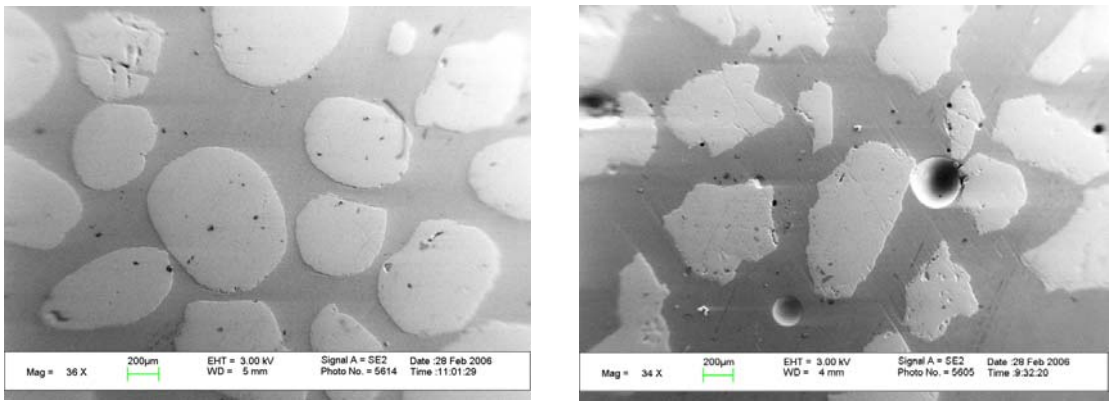

a **b**

Figure 6.4: SEM image of (a) sub-rounded Ottawa sand and (b) sub-angular Q-Rok sand subjected to 100 MPa stress after final polishing.

loading rate. The unloading continued until 90% of the maximum load was removed followed by a hold segment for 1000 s. This was followed with a final unload segment in which all the applied load was removed. The unloading was done in two steps where the effect of thermal drift, if any, was checked from the data of second load hold segment (i.e. at 10% of peak load).

For creep analysis, considering the smaller size of the individual sand particles, embedded within a softer polymer matrix with low creep parameters (as Q-Rok and Ottawa samples were made up of silica sand), we applied a lower peak load and extend the peak load holding time much longer. Similar surface approach mechanism as discussed above was used for the surface detection. The indentation creep experiment was performed at a constant loading rate of 10 mN/s (i.e., under load control) with the load increasing until a peak value of 75 mN was reached. This was followed by a hold segment for a total holding time limit of 10000 seconds. The unload segment was

performed under load control using a constant unloading rate of 10 mN/s. The unloading continued until 90% of the peak load was removed followed by a hold segment for 1000 s before complete unloading. During indentation, the thermal drift, if any, was checked from the data of second load hold segment.

Verification of experimental accuracy and determination of area function coefficients for nanoindentation were made by applying the same procedures as mentioned above on the amorphous fused silica. Elastic modulus, hardness and creep parameters for fused silica agreed with prior results from the literature.

RESULTS AND DISCUSSION

For the measurement of elastic modulus and hardness, typically ten indentation experiments were performed on ten different grains of Ottawa and Q-Rok sand samples and the indentation locations were carefully positioned at the center of the polished particle surface which was embedded in epoxy matrix. As defined before, the grains were having diameter greater than 600 μm and typically larger particles were chosen for nanoindentation. The behavior of load versus displacement for the ten indents for unstressed Ottawa and Q-Rok sand samples (i.e. at zero stress) is shown in Figure 6.5a and Figure 6.5b respectively. Good repeatability of load versus displacement nature for the ten indents is noticed.

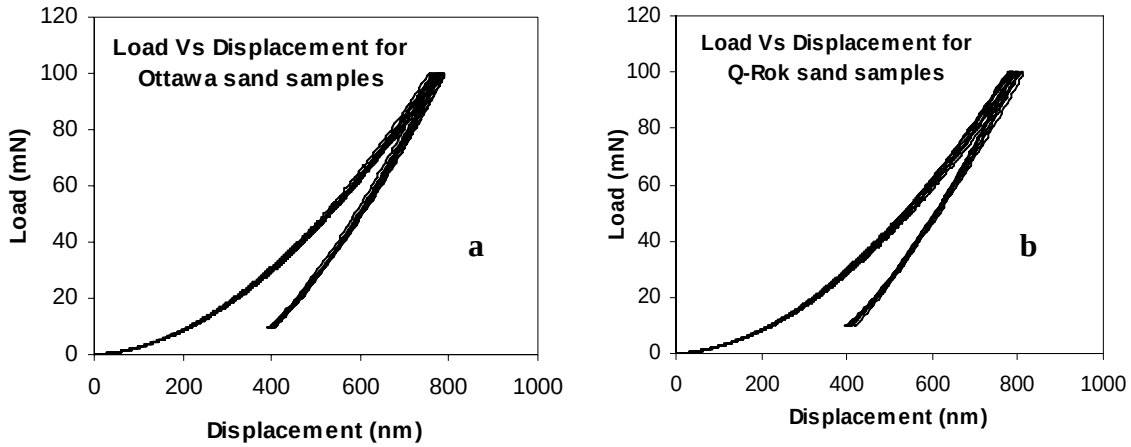

Figure 6.5: Load versus deformation for (a) unstressed Ottawa sand particles and (b) unstressed Q-Rok sand particles.

The same indentation method was applied on amorphous fused silica (calibration material) for verification and calibration of the indentation experiments to obtain suitable area function. Figure 6.6a illustrates the load versus displacement curves for ten indents on the amorphous fused silica. The amorphous fused silica is an isotropic material and its published value of elastic modulus is about 72 GPa [32]. The average elastic modulus of fused silica at different depth of indentation based on the ten indents is shown in Figure 6.6b. Using the calibrated area function, the average of ten indents for this fused silica resulted in a modulus value of 72.6 GPa showing uniformity of the modulus for all depths of indentation as noticed in Figure 6.6b.

Using the same area function coefficients used for fused silica as mentioned above, the mean value of elastic modulus and hardness (average of ten indents) along with the error bar (~ one standard deviation) at different depths of indentation for Ottawa and Q-Rok sand at 100MPa stress are plotted in Figures 6.7 and 6.8 respectively. It is

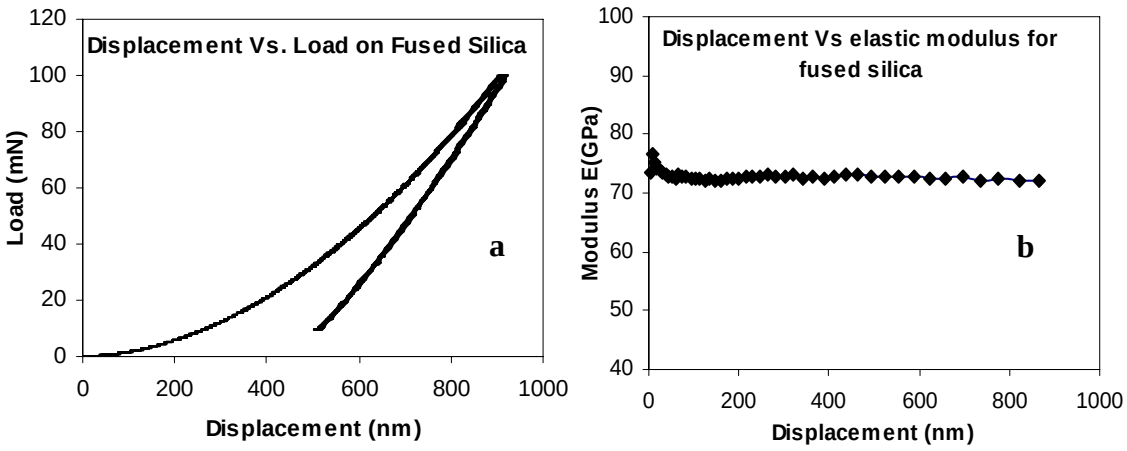

Figure 6.6: (a) Load versus deformation and (b) Elastic modulus versus deformation for fused silica.

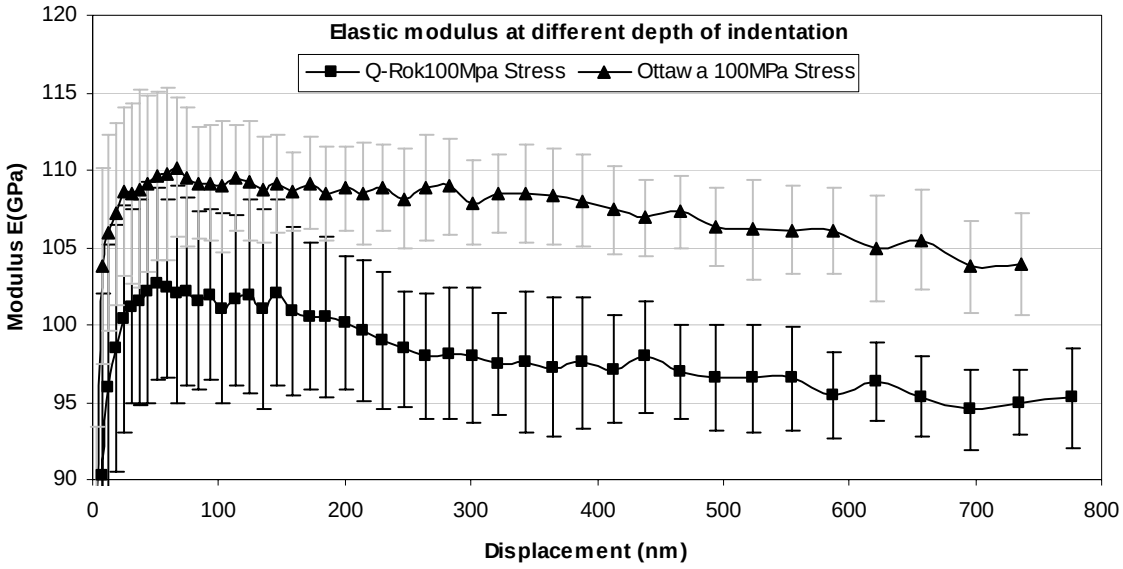

Figure 6.7: Mean modulus with depth of indentation for Ottawa and Q-Rok sand particles subjected to 100 MPa stress.

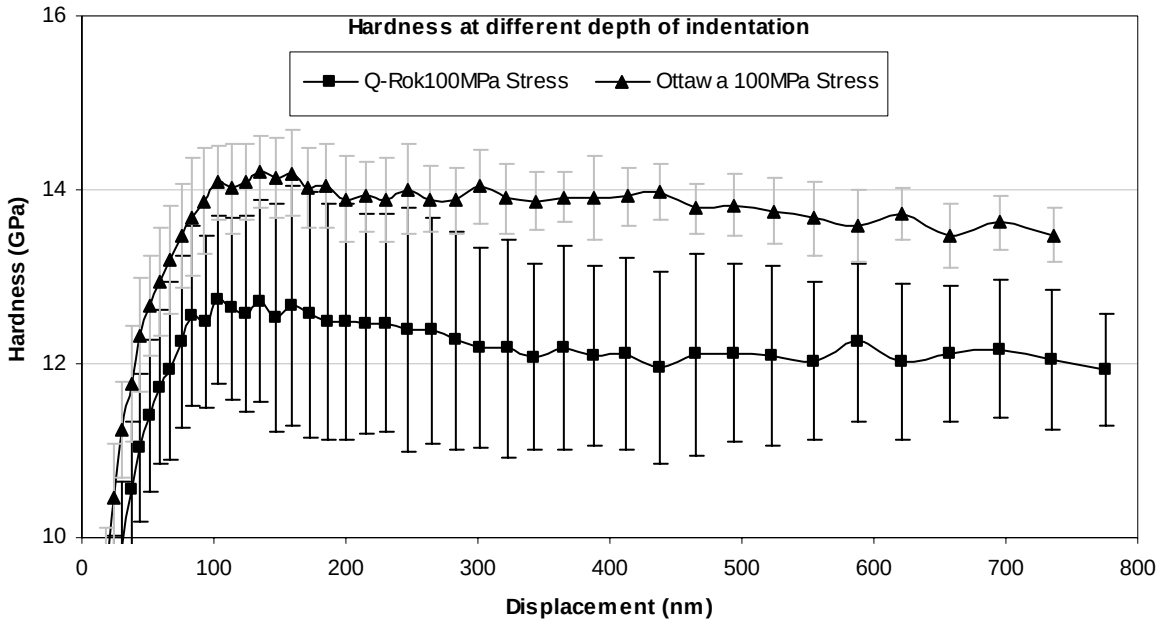

Figure 6.8: Mean hardness with depth of indentation for Ottawa and Q-Rok sand particles subjected to 100 MPa stress.

clearly evident that for all depths, the average modulus and hardness of Ottawa sand particles subjected to 100MPa stress is consistently higher than the Q-Rok sand particles at similar stress level.

The comparative results of mean modulus and mean hardness with the depth of indentation for Ottawa and Q-Rok sand particles at varying stress levels (0 and 100 MPa) are shown in Figures 6.9 and 6.10 respectively. A key observation is that the Ottawa sand particles are in general having comparatively higher elastic modulus and hardness than Q-Rok sand particles at a given stress level. This observation is in agreement with the macroscopic 1-D compressive test results on same materials [30] showing that sub angular Q-Rok sand particle assembly exhibit greater initial strain and a greater overall strain than sub rounded Ottawa sand under similar stress level. In their study, a higher

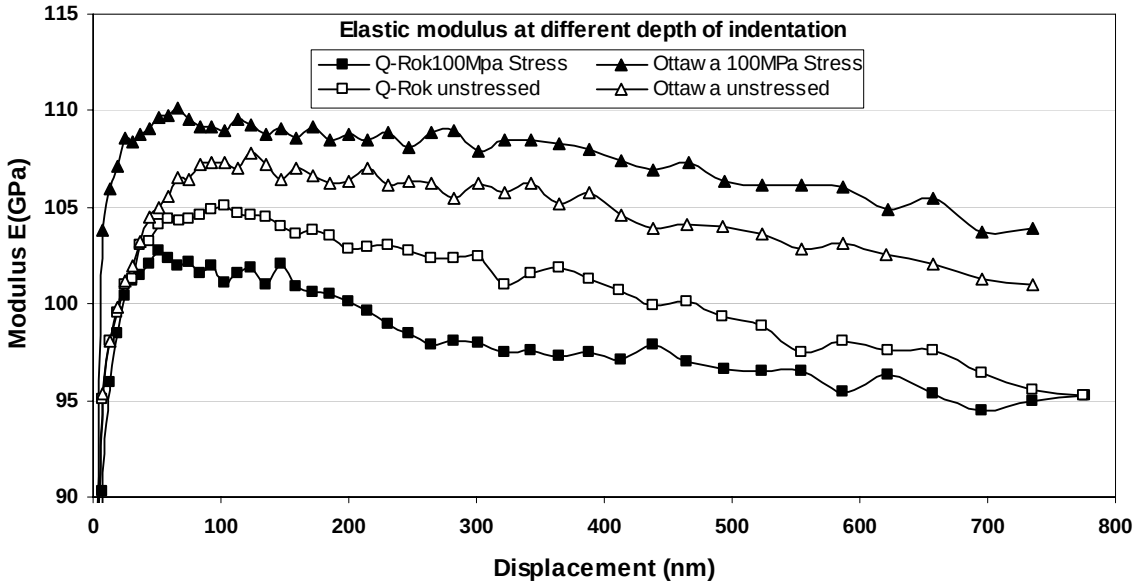

Figure 6.9: Mean modulus with depth of indentation for unstressed and 100 MPa stressed Ottawa and Q-Rok sand particles.

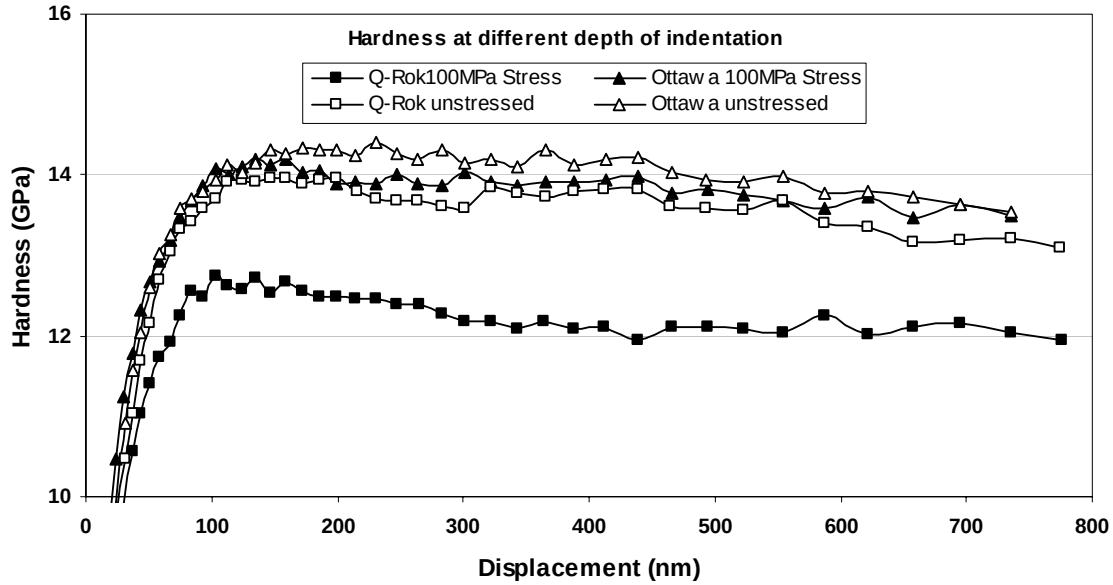

Figure 6.10: Mean hardness with depth of indentation for unstressed and 100 MPa stressed Ottawa and Q-Rok sand particles.

fraction of finer particle generation under 1-D compression for Q-Rok sand particles was correlated with the shape factor where the particle failure was considered primarily through asperity breakage. For Ottawa sand, failure of the particles at higher stress was correlated with the particle splitting and not by asperity breakage. However, based on the general trend of hardness and modulus of these two types of materials in Figures 6.9 and 6.10, it is clear that besides the shape factor, the engineering properties of the materials also plays an important role in particle failure. Figure 6.9 also reveals that with increased stress (at 100 MPa) the elastic modulus for the Ottawa sand particles increases for all depth of indentation compared to the zero stressed particles. Whereas, for Q-Rok particles, we noticed a decrease in modulus for 100MPa stressed particles as compared to the zero stressed particles. This implies that under applied stress, Q-Rok sand particles exhibits lower material strength than the Ottawa sand particles.

The hardness versus displacement plots (Figure 6.10) shows only small differences between the hardness of Ottawa sand at 0 MPa (unstressed) and 100MPa stress and Q-Rok sand at 0 MPa (unstressed), but there is remarkable decrease in hardness for Q-Rok sand at 100 MPa stress. The general trend in hardness, however, is that induced stress results a lowering of hardness for both types of sand particles and the overall hardness decrease is much higher in Q-Rok sand as compared to Ottawa sand. The softer material behavior for Q-Rok sand particles is also evident from the higher indentation depth reached by these materials compared to the Ottawa sand particles under the same indentation peak load of 100 mN.

In addition to these differences in their mechanical properties between the two types of particles described above, it is expected that their breakage behavior will also be different under any given stress condition, particularly at higher stress level. Lowering of hardness and modulus for Q-Rok sand at higher applied stress level thus will cause rapid particle failure compared to the Ottawa sand. This implies that besides asperity breakage, overall particle failure can also be a major contributor for generation of higher fraction of fines for Q-Rok sand than Ottawa sand at higher crushing stress values.

Table 6.2 shows a comparative summary of average elastic modulus and hardness for the two types of sand particles at zero stress and 100 MPa stress. In this research, measurement values for depth of indentation larger than 100 nm were only considered to compute the average modulus and hardness, due to higher confidence in determining true cross-sectional area of the indenting tip at corresponding depths [33]. From Table 6.2, it is seen that at zero stress, the average elastic modulus and hardness of Q-Rok sand particles is 3.8% and 3.1% respectively smaller than corresponding Ottawa particles at zero stress, whereas with 100 MPa applied stress, the respective parameters are decreased by 8.8% and 11.5% respectively.

Figures 6.9 and 6.10 also illustrate that with increase in indentation depth, average modulus and hardness consistently decreased for all samples, suggesting substrate may have an influence on modulus and hardness. It is important to note that for indentation purposes, larger particles were chosen randomly and the exposed surface profile of the particles through SEM images (Figures 6.4a and 6.4b) shows an average particle diameter

Table 6.2: Mean modulus and hardness results from indentation test.

Sand	Average Modulus (GPa)	Std. Dev	Average Hardness (GPa)	Std. Dev
Ottawa_Zero stress	105.18	1.9	14.10	0.24
Ottawa_100MPa Stress	107.65	1.61	13.89	0.19
Q-Rok_Zero stress	101.14	2.86	13.67	0.25
Q-Rok_100MPa Stress	98.20	2.21	12.29	0.24

greater than 600 μm. This indicates that during polishing, to expose the surface for indentation, the particles reduced in size to approximately half of its original value 300 μm due to polishing. The maximum indentation depth reached for all the samples were less than 800 nm which was 0.27% of the total sample depth. Numerous investigators have used both experimental and theoretical methods to study the substrate effects during nanoindentation testing based on film/substrate response [34-38]. Based on their study it may be inferred that due to larger ratio of total sample depth versus indentation depth, substrate effect may not be an issue. Unfortunately, there is no such study that describes the substrate effect during indentation for such type of small size granular materials whose modulus and hardness are much higher than the polymer matrix. Dutta et al. [17, 18] showed in their previous study that the hardness of the polymer matrix after its curing was 0.29 GPa with a Young's modulus of 4.78 GPa. Thus, comparing the substrate parameters with the results shown in Table 6.2, the modulus and hardness of the sand samples are 20 to 40 times larger than the polymer substrate. Owing to these large differences in mechanical properties between the indenting sample and substrate, a possible substrate effect can not be fully denied and needs further study. We also noticed that the decreasing trend of hardness and modulus for Q-Rok samples are prominent from

the lower indentation depth (as low as 100 nm), whereas for Ottawa sand this trend initiates at higher indentation depths (at 400 nm). The possible reason may be due to the differences in particle morphology of these two types of materials and the nature of contacts the particles make with the substrate. As Ottawa particles are sub rounded, the particle-substrate contact is semi-spherical (considering the embedded portion of the particle within the substrate), whereas, the sub-angular morphology of the Q-Rok particles creates irregular contact with the substrate with sharper tip. Due to the semi-spherical contact of the Ottawa particles, the stress distribution at the sample-substrate interface for a given applied indentation load will be more uniform compared to the irregular shaped contact interface for Q-Rok samples, and thus the substrate is expected to provide higher resistance against any strain gradient at the contact interface. This suggests that the particle morphology can also trigger a plausible substrate effect and demands additional research. However, as our focus in this study was to establish procedure for using nanoindentation for measuring the mechanical properties of the individual particles and such study is unprecedented, comprehensive substrate effects were not addressed.

It is important to note that contact area, elastic modulus and hardness during nanoindentation were determined by analyzing the load-displacement data according to Oliver and Pharr [31] method. This method does not account for material pile-up or sink-in. A typical SEM image of the nanoindentation on the sand material is shown in Figure 6.11 and does not indicate any significant pile-up or sink-in, validating the approach used for interpretation.

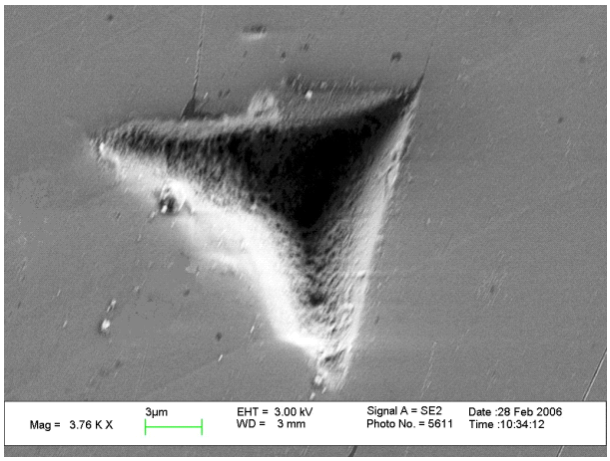

Figure 6.11: SEM image of typical indentation shape in sand specimen showing minimal pile-up or sink-in.

CREEP BEHAVIOR OF OTTAWA AND Q-ROK SAND PARTICLES

For analyzing creep behavior of the individual sand particles, a constant rate of loading followed by a hold segment was applied. Figure 6.12 is a typical plot of the load time history used for the creep tests of stressed and unstressed sand particles as well as for the reference material (fused silica). As shown in the figure, the load on the indenter was ramped to a specified maximum (75 mN in this study) at a constant loading rate of 10 mN/s and was kept constant during holding segment for a time period of 10,000 seconds, to monitor the displacement versus time (indentation creep) response. The unloading segment was also performed in load control mode with an unloading rate of 10 mN/s and once the load dropped to a value of 10% of the peak load another hold segment for 1,000 seconds was implemented to measure the thermal drift related data. During creep experiments, a major issue is the stability of the indentation equipment and care has been exercised to minimize variation in temperature during the hold segment by using

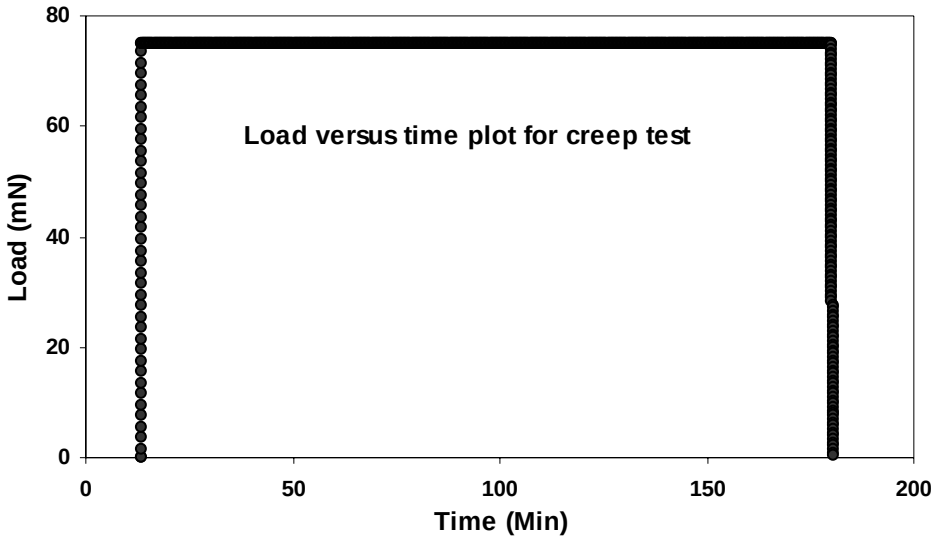

Figure 6.12: Plot showing load versus time for the creep experiment

temperature controlled environment. Prior to starting the indentation test, efforts were made to minimize the effects of thermal drift by allowing the instrument and sample environment to reach a state of thermal equilibrium for several hours (typically 6 hours). For those experiments where the thermal drift rate has changed significantly, creep related data was discarded.

Figure 6.13 illustrates a typical behavior of indentation creep response for different types of individual silica particles and the reference material made of fused silica. Higher indentation creep strain was observed for Ottawa and Q-Rok particles at unstressed compared to 100 MPa stress. This implies that induced stress affects the time dependent properties of granular materials and may have important implications to fault mechanism and earthquake studies. To analyze the repeatability, several tests were

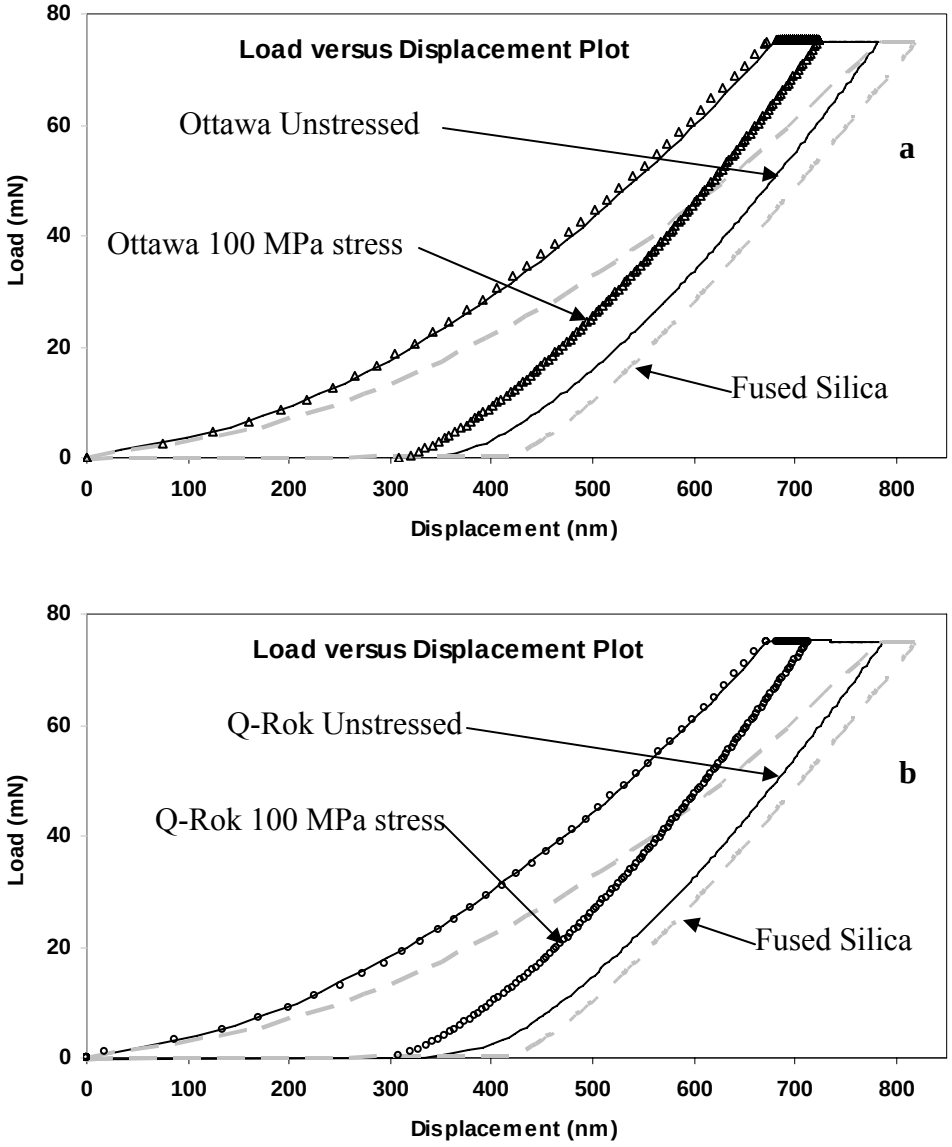

Figure 6.13: Results from indentation creep tests showing the influence of stress on time dependent deformation properties for (a) Ottawa sand unstressed and 100 MPa stressed particle along with fused silica (b) QRok sand unstressed and 100 MPa stressed particle along with fused silica.

performed on different granules of each type of stressed and unstressed sand particles and good repeatability was observed. Typical load displacement behavior of three tests performed on three different grains of Q-Rok sand at 100 MPa stress is shown in Figure 6.14 which shows good repeatability response.

A comparison of displacement-time data under constant load for different types of sand particles at zero stress (i.e. unstressed) and 100 MPa stress along with the standard fused silica behavior is shown in Figure 6.15. To facilitate comparison, the displacement corresponds to the starting point of creep hold segments was initialized to be zero. This plot indicates that with increasing stress from zero to 100 MPa, the resulting creep displacements for both types of sands decrease noticeably. The displacement rate during the hold period under constant load is observed to be high for the initial stage of hold segment and decreases with increase in hold time. For the fused silica, it is found that the displacement increases at a declining rate with time and finally reaches an almost constant displacement rate, resulting in a decreasing strain rate against time and displacement. In comparison to all the samples examined, minimum creep displacement was observed for the fused silica. It can also be seen from Figure 6.15 that the creep displacement is larger for Q-Rok than Ottawa when they were not subjected to stress, and the trend reversed slightly for these particles at 100 MPa stress, suggesting that the induced one-dimensional compression stress affects Q-Rok particles more than the Ottawa sand particles.

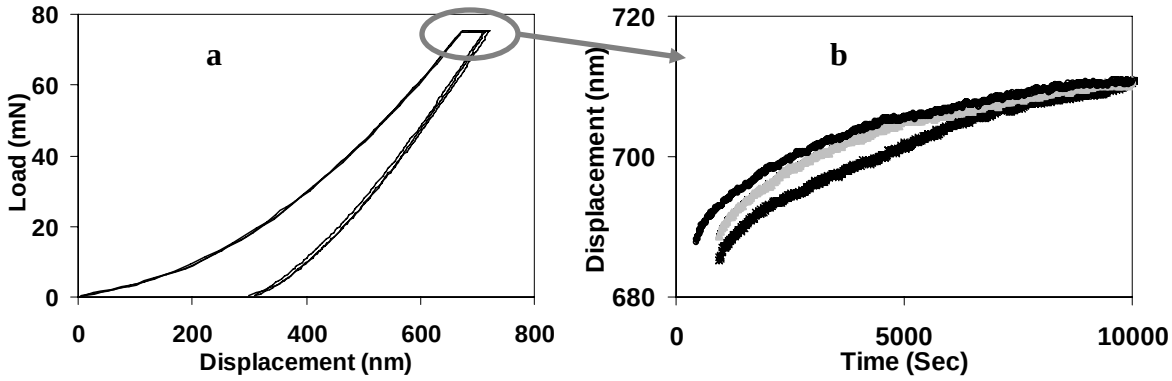

Figure 6.14: The repeatability results of three tests performed on Q-Rok 100 MPa stressed particles (a) Load versus displacement response and (b) Displacement versus time response for the load hold segment of three tests.

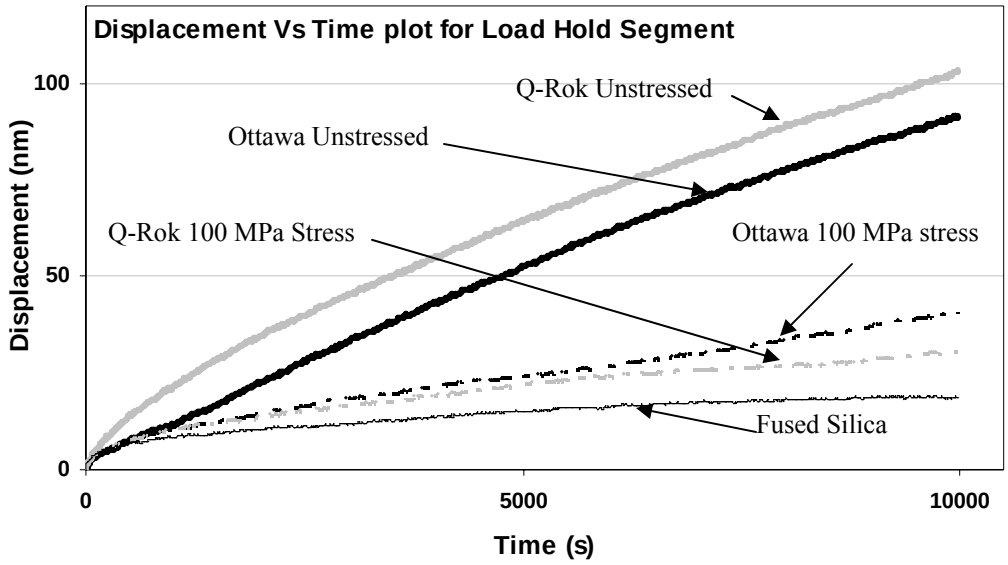

Figure 6.15: Variation of creep displacement during load hold segment for unstressed and stressed (100 MPa) Ottawa and Q-Rok sand, and fused silica.

It is to be noted that the method applied for performing creep property measurements in this study was a constant rate of loading/hold type of experimentation which was first proposed by Mayo et al [39]. This type of experiment utilizes the ability of the nanoinderter XP to incrementally apply the load on the indenter up to the specified peak load and then keep the load constant for a period of time, allowing one to determine the indentation strain rate and hardness during the hold segment when both were expected to be changing. In uniaxial tests, the behavior of a wide range of materials can be described by the relation [40],

$$\dot{\varepsilon} = A\sigma^n, \tag{6.1}$$

where $\dot{\varepsilon}$ is the strain rate, σ is the applied stress, n is the stress exponent and the factor A contains the temperature dependence through the Boltzmann factor. The stress exponent provides useful information on the mechanism of the time-dependent plastic deformation concerned.

According to Pollock et al. [41], in depth sensing nanoindentation, the strain rate $\dot{\varepsilon}$ should according to Equation 6.2.

$$\dot{\varepsilon} = \frac{d}{dt}(\varepsilon) = k\frac{\left(\frac{dh}{dt}\right)}{h}. \tag{6.2}$$

Here, ε is the creep strain, h is the instantaneous displacement of the indenter and k is a geometric constant. The stress σ (or hardness) can be approximated with the following scaling relations

$$\sigma \sim P/h^2 \sim H, \tag{6.3}$$

where, P is the indentation load, h is displacement and H is hardness.

Applying the definition of strain rate and stress as shown in Equations 6.2 and 6.3, the hardness based creep parameter for the sand particles can be quantified from the variation of indentation strain rate versus hardness (on logarithmic scale) to obtain the creep parameter using measured displacements under hold segment. Figure 6.16 shows the comparison of log (strain rate) versus log (hardness) for the different sand particles and the fused silica. Here, for measuring strain rate, each data point represents 100 second average instantaneous displacement versus average hardness under the peak load hold segment. The hardness is obtained based on Oliver-Pharr method by dividing the load by the instantaneous contact area. The data observed to undergo a transient period immediately following the completion of the load ramp yielding a higher stress exponent for creep. The power law fit to the linear portion of the data provides the stress exponent for the corresponding materials and is shown in Figure 6.16.

In recent work, Li et al. [42], measured the stress exponent from indentation creep experiments by fitting the log strain rate versus log stress data. In their calculation, the stress has been calculated by P/h^2 (as per Equation 6.3). The displacement rate $\dot{h}$, has been calculated by using a fitting protocol where the instantaneous indenter displacement variation with time has been approximated using an empirical formula. To have a better understanding about the creep behavior of the different sand particles similar technique was explored in this study for obtaining creep exponent. The measured displacement versus time data during creep hold segment for experiments were approximated with

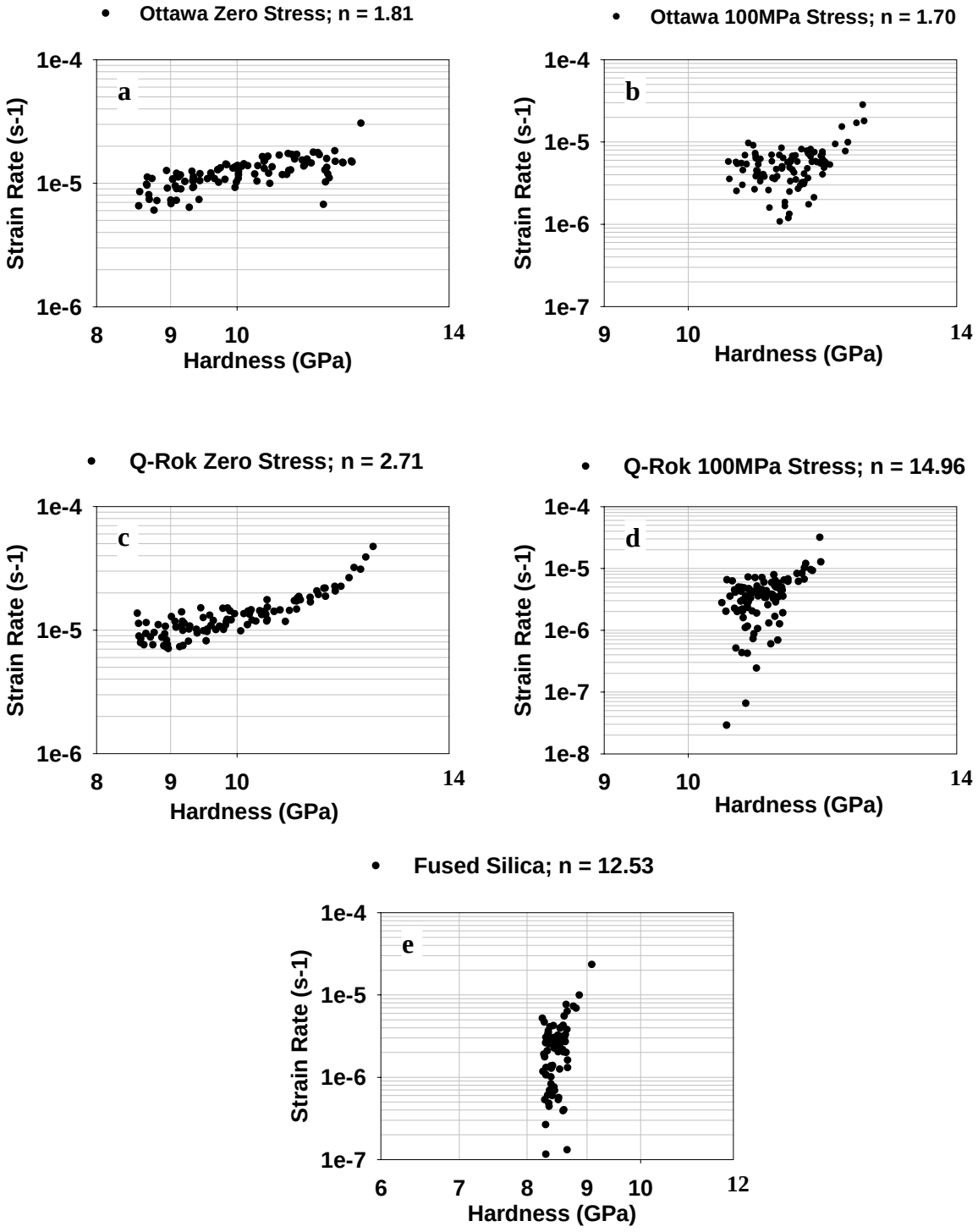

Figure 6.16: Variation of indentation strain rate with hardness (a) Ottawa sand unstressed, (b) Ottawa sand subjected to 100 MPa , (c) unstressed Q-Rok sand, (d) Q-Rok sand subjected to 100 MPa and (e) amorphous fused silica.

an empirical formula as shown in Equation 6.4 and the displacement rate $\dot{h}$, calculated from the curve fitting procedure.

$$h(t) = a + b*t + c*(t)^m. \tag{6.4}$$

Here, a, b, c, and m are fitting constants and t is time.

Figures 6.17-6.21 show the experimental displacement versus time curve during the load hold at 75 mN together with the fitted curve using Equation 6.4 as well as the plots of stress versus strain using log scale for different sand samples and the reference fused silica. It is observed that the fit with assumed function is very good with a correlation coefficient R^2~ 0.99 for all the data. From the strain-rate versus stress (~ P/h^2) plots, it was also noticed that the stress exponent at the start of the load hold is very large and it decreases reaching a steady state at larger holding time.

The creep exponent values for both Ottawa and Q-Rok obtained using the two different techniques described above show a good agreement, except for the case of fused silica. The hardness based creep exponent for the fused silica is 12.53 (Figure 6.16e), whereas the curve fitting method with stress measured as P/h^2 shows a creep exponent as 36.21 (Figure 6.21b). It is noticed from Figure 6.15 that the fused silica experienced the lowest creep (~ 18 nm) in comparison to sand particles (~ 100 nm for 100 MPa stressed particles and ~ 40 nm for zero stressed sand particles). The hardness based creep exponent measurement for our study uses continuous stiffness, constant load method where hardness is measured based on contact area that in turn depends on the accurate

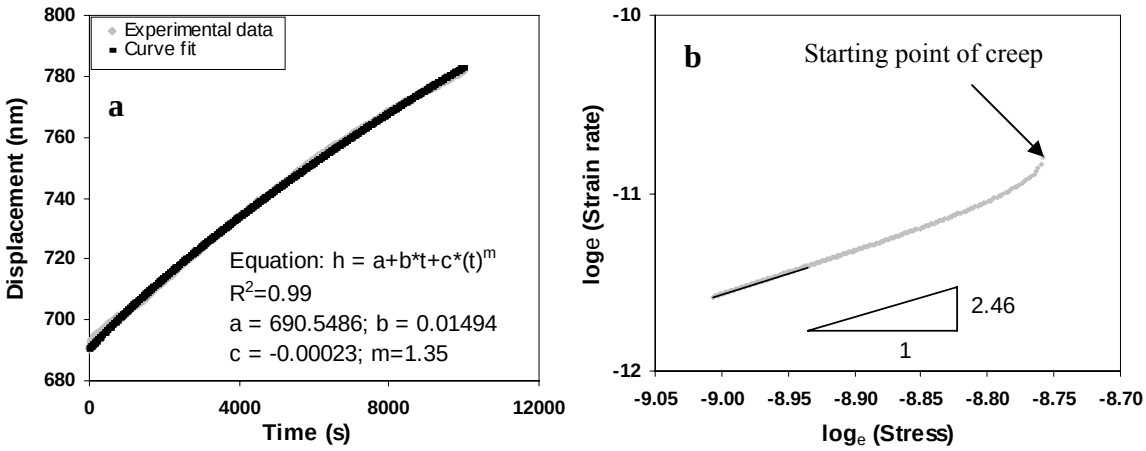

Figure 6.17: (a) Experimental and fitted creep curves for Ottawa unstressed particle, and (b) corresponding log strain rate versus log stress plot.

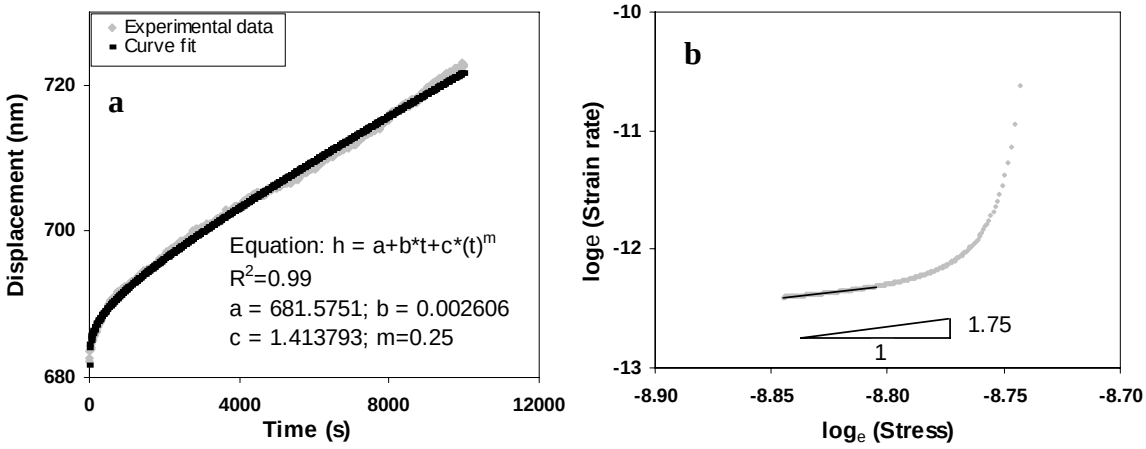

Figure 6.18: (a) Experimental and fitted creep curves for Ottawa sand particle subjected to 100MPa vertical stress, and (b) corresponding log strain rate versus log stress plot.

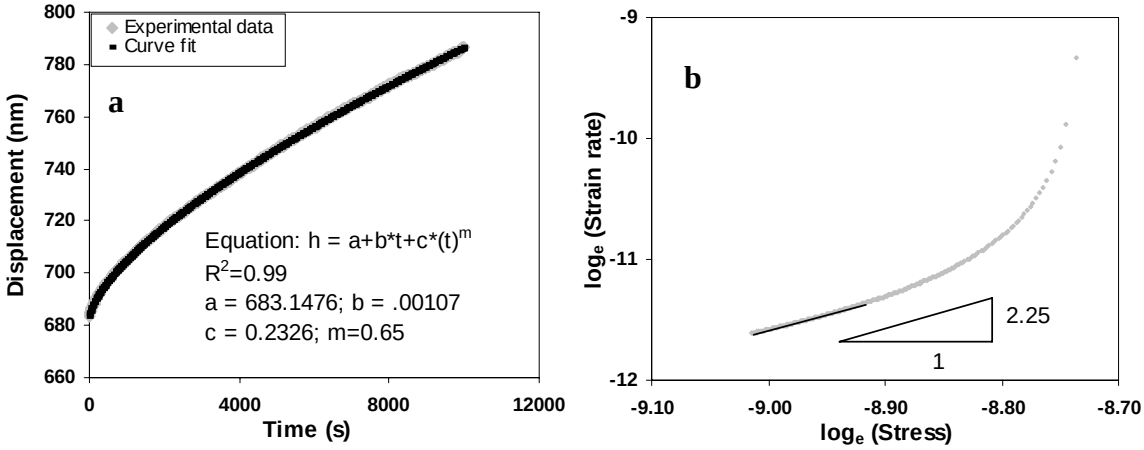

Figure 6.19: (a) Experimental and fitted creep curves for Q-Rok unstressed particle, and (b) corresponding log strain rate versus log stress plot.

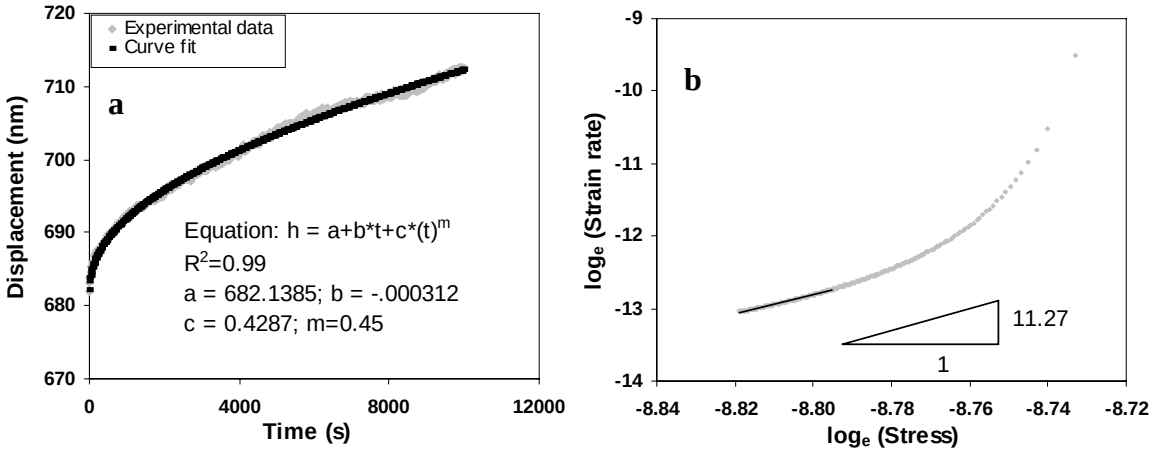

Figure 6.20: (a) Experimental and fitted creep curves for Q-Rok sand particle subjected to 100MPa vertical stress, and (b) corresponding log strain rate versus log stress plot.

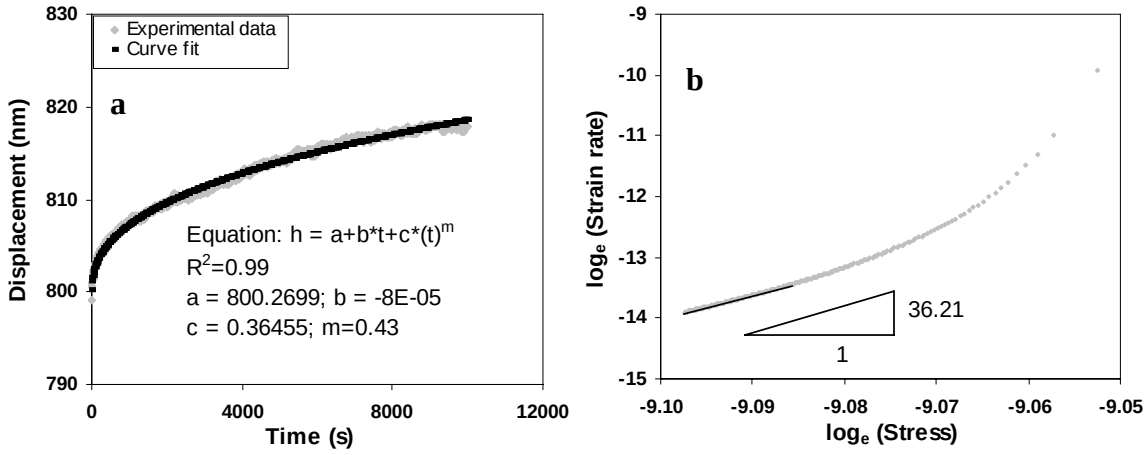

Figure 6.21: (a) Experimental and fitted creep curves for fused quartz, and (b) corresponding log strain rate versus log stress plot.

measurement of contact stiffness. For materials with very low overall creep as in fused silica, the noise background may convolute the contact stiffness changes and thereby constant decrease of hardness during load hold period may not be observed. Hence, the differences in creep exponent measurement for fused silica using two techniques may be due to the lack of a robust linear fitting of the data on hardness based creep exponent measurement.

Li et al. [42] also concluded in their study that fused silica exhibits intense size effects and indicated that as the initial indent depth exceeds 300 nm, the stress exponent saturates to a value between 60 and 80, whereas our measurement shows the creep exponent for fused silica is 36.21 for the initial indent depth of about 800 nm. This is to be noted that our creep exponent value is for larger time period (~ beyond 7000 seconds) during the load hold segment, whereas, Li et al. reported the exponent based on much lower load hold time period. Moreover, the creep experiment performed by Li et al. was

depth sensing constant load method where displacement was monitored as a function of time during load hold, whereas as stated before, we applied the continuous stiffness-constant load technique where hardness is measured based on Oliver-Pharr method in which measured contact stiffness provided measurement of contact area. Besides, the indentation machines used by Li et al. were Hysitron TriboScope for small load tests and CSM nanoindentation testing system for higher load tests, whereas Nanoindenter XP has been used for all of our experiments. Thus, the measured creep exponent differences may be attributed to the differences in experimental procedures, data measurement techniques as well as the measurement accuracy of the equipments used by Li et al. and the tests in this research.

The creep exponent analysis for Ottawa sand particles using the two different techniques illustrates that very little decrease in exponent is noticed for particles subjected to 100 MPa vertical stress compared to the unstressed particle (stress exponent changes only slightly from 1.81 to 1.70 using hardness based analysis and it decreases from 2.46 to 1.75 using curve fitting). But for Q-Rok sand particle, both the techniques exhibit a large increase in creep exponent for 100 MPa stressed particle compared to zero stressed particle (stress exponent increases from 2.71 to 14.96 using hardness based analysis and from 2.25 to 11.27 using curve fitting). Repetitive measurements (three tests on different particles of each sand type) of creep tests were performed on different types of sand particles and the creep exponents analyzed during the large load hold period are shown in Figure 6.22 along with the error bars. Very good repeatability is evident from the low error bar limits.

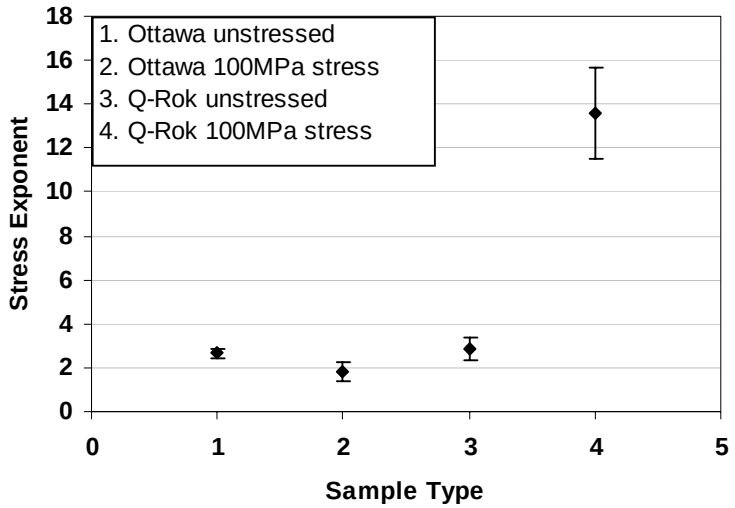

Figure 6.22: Variation of creep stress exponent with error bars for Ottawa and Q-Rok sand unstressed and 100 MPa of stress particles.

The comparative behavior of strain rate versus stress for the entire duration of creep segment of the indentation experiments for all the samples is shown in Figure 6.23. It is observed that at the initial hold portion of the data (probably a transient state), those particles which were subjected to 100 MPa of stress behave similarly (approximately equal slope) during creep, whereas the creep behavior for unstressed Ottawa and Q-Rok particles is similar at larger time period of load hold.

The indentation strain rate (based on curve fitting measurement) versus time for all the specimen is illustrated in Figure 6.24. A deviation in slope is observed during the initial stage of data where transient state probably exists. The slope of indentation strain versus time become constant once the initial transient period is surpassed (approximately beyond initial 2000 seconds). It is observed that indentation strain rate for fused silica at any given time is the lowest. At higher creep hold time (~ beyond 2000 second), the

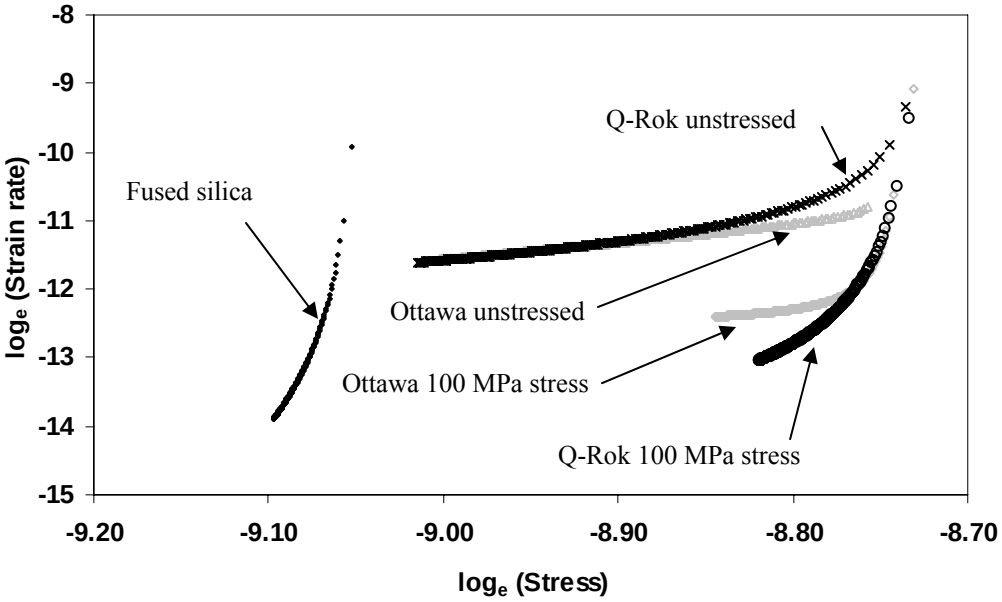

Figure 6.23: Variation of log (strain rate) versus log (stress) for fused silica and Ottawa and Q-Rok sand unstressed and 100 MPa stressed particles.

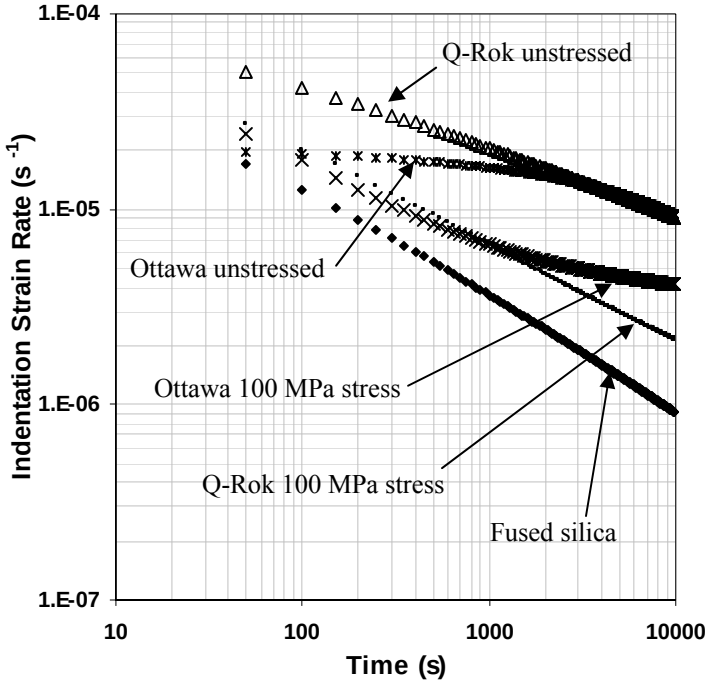

Figure 6.24: Variation of indentation strain rate versus time for fused silica and Ottawa and Q-Rok sand unstressed and 100 MPa stressed particles.

unstressed sand particles exhibit higher indentation rate than the 100 MPa stressed particles. Moreover, indentation strain rate of unstressed Ottawa and Q-Rok sand particles is almost equal beyond 2000 second hold time, but for those particles subjected to 100 MPa stress, Q-Rok sand experienced lower indentation strain rate than Ottawa sand. However, analogous to the creep exponent values, the rate of change of indentation strain rate (decreasing trend) at larger time during the constant load period was observed to be maximum for fused silica (from the highest slope of the curves in Figure 6.24) and minimum for Ottawa sand particles subjected to 100 MPa vertical stress. The unstressed particles show almost equal slope which is slightly higher than the Ottawa sand particles subjected to 100 MPa vertical stress. The rate of change of indentation strain rate for Q-Rok sand particles subjected to 100 MPa stress is lower than fused silica but remarkably higher than all other sand particles.

SUMMARY AND CONCLUSION

In the present work, the mechanical properties of Ottawa and Q-Rok sand at particle level were studied using instrumented nanoindentation, and the effect of mechanical property changes due to the application of 100 MPa confined compressive stress were analyzed. The following can be concluded from this study:

(1) This research explored nanoindentation technique for measuring the mechanical properties of micrometer-sized granular materials and introduced the appropriate experimental and interpretation procedure as well as sample preparation technique. Two different approaches, viz. hardness based and curve fitting method were

applied to evaluate the creep stress exponents for two types of sand particles subjected to varying stress levels in aggregate form in confined compression condition.

(2) Though there was mineralogical and structural similarity exists between the two types of sand particles analyzed, Ottawa sand particles have higher elastic modulus and hardness than Q-Rok sand particles at any given stress. The nanoindentation study on these materials revealed that the mechanical response of the two types of materials changed due to the application of 100 MPa of vertical stress in 1-D compression. Under stressed condition, the elastic modulus of Ottawa sand particles increases from their unstressed condition, whereas Q-Rok sand particles showed a decrease in modulus with applied stress.

(3) The indentation creep strain was observed to be higher for both types of sand particles at unstressed condition, implying that the induced stress effect on individual granular particles is counter intuitive. The effect of stress was much more pronounced for angular shaped Q-Rok particle when compared to well rounded Ottawa sand which is also evident from the remarkable increase creep-stress exponent of the Q-Rok sand particles at 100 MPa stress compared to the other sand particles.

REFERENCES

1. Billam, J., *"Some aspects of the behaviour of granular materials at high pressures: stress-strain behaviour of soils", P*roceedings of the Roscoe Memorial Symposium (ed. R.H.G.Parry), 69-80, G.T.Fonlis & Co. Ltd., 1972.

2. Bolton, M.D., *"The strength and dilatancy of sands",* Geotechnique, 1986, 36(1), 65-78.

3. Lee, D.M.,*"The angles of friction of granular fills",* PhD dissertation, University of Cambridge, 1992.

4. Yamamuro, J.A. and Lade, P.V.,*"Drained sand behavior in axisymmetric tests at high pressures",* J. Geotech. Engrg., ASCE, 1996, 122(2) 109-119.

5. Lade, P.V. and Yamamuro, J.A., *"Undrained sand behavior in axisymmetric tests at high pressures",* J. Geotech. Engrg., ASCE, 1996, 122(2) 120-129.

6. Yamamuro, J.A.; Bopp, P.A.; and Lade, P.V., *"One-dimensional compression of sands at high pressures",* J. Geotech. Engrg., ASCE, 1996, 122(2) 147-154.

7. Jaeger, J.C., *"Failure of rocks under tensile conditions",* Int. J. Rock Min. Sci., 1967, 4, 219-227.

8. McDowell,G.R. and Amon, A., *"The application of Weibull statistics to the fracture of soil particles",* Soils Found., 2000, 40(5), 133-141.

9. Weibull, W., *"A statistical distribution function of wide applicability",* J. Appl. Mech., 1951, 18, 293-297.

10. Nakata, Y.; Hyde, A.F.L.; and Murata, H.,*"A probabilistic approach to sand particle crushing in the triaxial test",* Geotechnique, 1999, 49(5), 567-538.

11. Nakata, Y.; Hyodo, M.; Hyde, A.; Kato, Y.; and Murata, H., *"Microscopic particle crushing of sand subjected to high pressure one-dimensional compression",* Soils and Foundations, 2001, 41, 69-82.

12. Nakata, Y.; Kato, Y.; Hyodo, M.; Hyde, A.; and Murata, H., *"One-dimensional compression behavior of uniformly graded sand related to single particle crushing strength",* Soils and Foundations, 2001, 41, 39-51.

13. Hearmon, R.F.S., *"The elastic constants of crystals and other anisotropic materials, in Landolt-Bornstein Tables",* III/11, 1-244, edited by K.H. Hellwege and A.M. Hellwege, Springer-Verlag, Berlin, 1979, 854.

14. Hearmon, R.F.S., *"The elastic constants of crystals and other anisotropic materials, in Landolt-Bornstein Tables",* III/18, 1-154, edited by K.H. Hellwege and A.M. Hellwege, Springer-Verlag, Berlin, 1984, 559.

15. Sumino, Y. and Anderson, O.L., *"Elastic constants of minerals, in: Handbook of Physical Properties",* III edited by Robert S. Carmichael, CRC Press, Boca Raton, FL., 1984.

16. Bansal, N. P. and Doremus, R. H., *"Handbook of Glass properties",* Academic Press, Orlando, FL., 1986, 680.

17. Penumadu, D.; Dutta, A.; Pharr, G. M.; and Files, B., *"Mechanical Properties of Blended Single-Wall Carbon Nanotube Composites",* J. Mater. Res., 2003, 18 (8), 1849-1853.

18. Dutta, A.K.; Penumadu, D.; and Files, B., *"Nanoindentation Testing for Evaluating Modulus and Hardness of Single-Walled Carbon Nanotube-Reinforced Epoxy Composites",* J. Mater. Res., 2004, 19(1), 158-164.

19. Camerucci, M.A.; Urretavizcaya, G.; and Cavalieri, A.L., "*Mechanical behavior of cordierite and cordierite-mullite materials evaluated by indentation techniques",* J. of the Euro. Ceramic Soc., 2001, 21, 1195-1204.

20. Ahn, H; Klimek, K. S; Rie, K.T., "*BCN coatings by RF PACVD at low temperature",* Surf. and Coat. Technol., 2003, 174-175, 1225-1228.

21. Mencík, J.; Munz, D.; Quandt, E.; Weppelmann, E. R.; Swain, M., "*Determination of elastic modulus of thin layers using nanoindentation",* J. of Mate. Res., 1997, 12(9), 2475-2484.

22. Lim,Y. Y.; Chaudhri, M. M., "*The effect of the indenter load on the nanohardness of uctile metals: an experimental study on polycrystalline work-hardened and annealed oxygen-free copper",* Philosophical Magazine A, 1999, 79(12), 2979 - 3000.

23. Tsui, T. Y.; Pharr, G. M., "*Substrate effects on nanoindentation mechanical property measurement of soft films on hard substrates",* J. of Mater. Res., 1999, 14(1), 292-301.

24. Saha, R.; Nix, W.D., "*Effects of the substrate on the determination of thin film mechanical properties by nanoindentation",* Acta Mater, 2002, 50(1), 23-38.

25. Hayes, S.A; Goruppa, A.A.; and Jones, F.R., "*Dynamic nanoindentation as a tool for the examination of polymer materials",* J. Mater. Res., 2004, 19(11), 3298-3306.

26. Wang,W. and Lu, K., "*Nanoindentation measurement of hardness and modulus anisotropy in Ni3Al single crystals",* J. Mater. Res., 2002, 17(9), 2314-2320.

27. Vriend, N. M. and Kren, A. P., "*Determination of the viscoelastic properties of elastomeric materials by the dynamic indentation method",* Polymer Testing, 2004, 23, 369-375.

28. Schuh, C.A. and Nieh, T.G., "*A survey of instrumented indentation studies on metallic glasses*", J. Mater. Res., 2004, 19(1), 46-57.

29. McDowell, G. R. and Bolton, M. D., *"On the micromechanics of crushable aggregates"*, Geotechnique, 1998, 48, 667-679.

30. Jason, T. D.; Christoph, G.G., *"Relation of initial specimen state and particle properties to the breakage potential of granular soils*", 57th Canadian Geotechnical Conference; 5th Joint CGS/IAH-CNC Conference, Geo Quebec, 2004.

31. Oliver,W.C.; Pharr,G.M., *"An improved technique for determining hardness and elastic modulus using load and displacement sensing indentation experiments",* J. Mater. Res., 1992, 7(6), 1564-1583.

32. General Electric Fused Quartz Products Technical Data, general catalog number 7705-7725, April 1985.

33. Oliver,W.C.; Pharr,G.M., *"Measurement of hardness and elastic modulus by instrumented indentation: Advances in understanding and refinements to methodology",* J. Mater. Res., 2004, 19(1), 3-20.

34. Xu, H. and Pharr,G.M., *"An improved relation for the effective elastic compliance of a film/substrate system during indentation by flat cylindrical punch."* Submitted to J. Mater Res., 2006.

35. Bhattacharya, A. K.; Nix, W. D., *"Analysis of elastic and plastic deformation associated with indentation testing of thin films on substrates",* Int. J. Solids Struct., 1988, 24(12), 1287-1298.

36. Tsui, T. Y. and Pharr,G.M., *"Substrate effects on nanoindentation mechanical property measurement of soft films on hard substrates",* J. Mater. Res., 1999, 14(1), 292-301.

37. Saha, R. and Nix, W.D., *"Effects of the substrate on the determination of thin film mechanical properties by nanoindentation",* Acta Mater., 2002, 50, 23-38.

38. Chen, X. and Vlassak, J.J., *"Numerical study on the measurement of thin film mechanical properties by means of nanoindentation",* J. Mater. Res., 2001, 16(10), 2974-2982.

39. Mayo, M.J.; Siegel, R.W.; Narayanasamy, A.; and Nix, W.D., "*Mechanical properties of nanophase TiO sub 2 as determined by nanoindentation",* J. Mater. Res., 1990, 5(5), 1073-1082.

40. Poirier, J.P., *"Creep of crystals-high temperature deformation processes in metals, ceramics and minerals",* Cambridge University Press, Cambridge, U.K., 1985.

41. Pollock, H. M.; Maugis, D.; and Barquins, M., *"Microindentation Tech. in Mat. Sci. & Eng.",* Edited by P.J.Blau and R. Lawn ASTM 47, Pittsburgh, PA., 1986.

42. Li, H. and Ngan, A. H. W., *"Size effect of nanoindentation creep",* J. Mater. Res., 2004, 19(2), 513-522.

Appendix 6A: U.S. Silica Product data sheet for Ottawa sand

U.S. SILICA®
Sands of Time

PRODUCT DATA

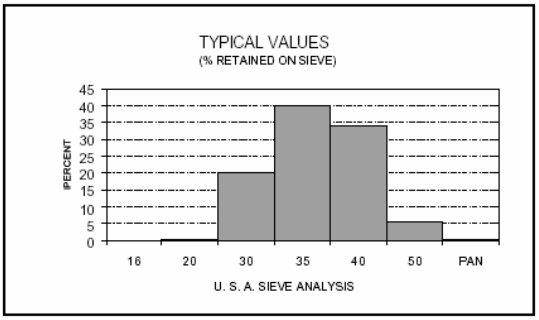

20/40 OIL FRAC

UNGROUND SILICA

PLANT: OTTAWA, ILLINOIS

USA STD SIEVE SIZE		TYPICAL VALUES		
		% RETAINED		% PASSING
MESH	MILLIMETERS	INDIVIDUAL	CUMULATIVE	CUMULATIVE
16	1.180	0.0	0.0	100.0
20	0.850	0.2	0.2	99.8
30	0.600	20.0	20.2	79.8
35	0.500	40.0	60.2	39.8
40	0.425	34.0	94.2	5.8
50	0.300	5.5	99.7	0.3
PAN		0.3	100.0	0.0

TYPICAL PROPERTIES

BULK DENSITY-COMPACTED (lbs/ft^3) 109
BULK DENSITY-UNCOMPACTED (lbs/ft^3) 102
HARDNESS (Mohs) 7
MELTING POINT (Degrees F) 3100

MINERAL ..... QUARTZ
GRAIN SHAPE ..... ROUND
SiO2 (%) 99.8
SPECIFIC GRAVITY 2.65

CONFORMS TO API(1) SPECIFICATION RP 56

(1) AMERICAN PETROLEUM INSTITUTE

December 15, 1997

DISCLAIMER: The information set forth in this Product Data Sheet represents typical properties of the product described; the information and the typical values are not specifications. U.S. Silica Company makes no representation or warranty concerning the Products, expressed or implied, by this Product Data Sheet.

WARNING: The product contains crystalline silica - quartz, which can cause silicosis (an occupational lung disease) and lung cancer. **For detailed information on the potential health effect of crystalline silica - quartz, see the U.S. Silica Company Material Safety Data Sheet.**

U.S. Silica Company P.O. Box 187, Berkeley Springs, WV 25411-0187 (304) 258-2500

Appendix 6B: U.S. Silica Product data sheet for Q-Rok sand

U.S. SILICA®
Sands of Time

PRODUCT DATA

#1 Q-ROK®

UNGROUND SILICA

PLANT: BERKELEY SPRINGS, WEST VIRGINIA

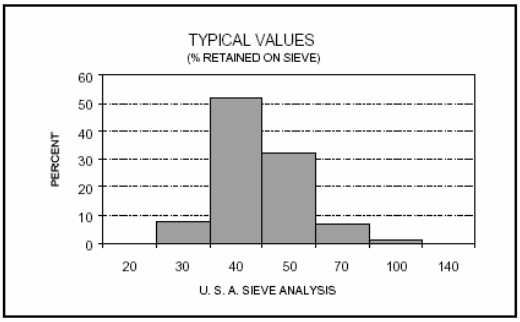

USA STD SIEVE SIZE		TYPICAL VALUES		
		% RETAINED		% PASSING
MESH	MILLIMETERS	INDIVIDUAL	CUMULATIVE	CUMULATIVE
20	0.850	0	0	100
30	0.600	8	8	92
40	0.425	52	60	40
50	0.300	32	92	8
70	0.212	7	99	1
100	0.150	1	100	0
140	0.106	0	100	0

TYPICAL PHYSICAL PROPERTIES

AFS[(1)] GRAIN FINENESS **34**
GRAIN SHAPE ..... **SUBANGULAR**
HARDNESS (Mohs) 7

(1) AMERICAN FOUNDRYMEN'S SOCIETY

MINERAL ..... **QUARTZ**
pH **6.5**
SPECIFIC GRAVITY **2.65**

TYPICAL CHEMICAL ANALYSIS, %

SiO_2 (SILICON DIOXIDE) **99.7**
Fe_2O_3 (IRON OXIDE) **0.022**
Al_2O_3 (ALUMINUM OXIDE) **0.07**
TiO_2 (TITANIUM DIOXIDE) **0.02**
CaO (CALCIUM OXIDE) **0.01**

MgO (MAGNESIUM OXIDE) ..... **<0.01**
Na_2O (SODIUM OXIDE) ..... **<0.01**
K_2O (POTASSIUM OXIDE) **0.01**
LOI (LOSS ON IGNITION) **0.2**

February 10, 2000

DISCLAIMER: The information set forth in this Product Data Sheet represents typical properties of the product described; the information and the typical values are not specifications. U.S. Silica Company makes no representation or warranty concerning the Products, expressed or implied, by this Product Data Sheet.

WARNING: The product contains crystalline silica - quartz, which can cause silicosis (an occupational lung disease) and lung cancer. **For detailed information on the potential health effect of crystalline silica - quartz, see the U.S. Silica Company Material Safety Data Sheet.**

U.S. Silica Company **P.O. Box 187, Berkeley Springs, WV 25411-0187** **(304) 258-2500**

PART 7: EVOLUTION OF MICROMECHANICS ASSOCIATED WITH 1-D GRANULAR COMPRESSION USING DISTINCT ELEMENT METHOD

This part is a slightly revised version of a journal paper by Amal K. Dutta and Dayakar Penumadu with the same title that will be submitted for review in 2006.

Dutta, A. K. and Penumadu, D., "Evaluation of micromechanics associated with 1-D granular compression using distinct element method," to be submitted for review, 2006.

My primary contributions to this paper include (1) design of the numerical modeling and development of the experimental protocols to study the mechanics of the granular material assembly, (2) programming computer code using FISH language to perform numerical simulation, (3) performing most of the laboratory experiments, (4) interpretation and analysis of results, (5) most of the writing.

ABSTRACT

Micromechanics associated with granular particles with different shape and packing is explored using DEM (Distinct Element Method). This study also focuses on the evolution of particle breakage behavior by validating experimental and simulated assembly of a granular media of known particle micro-parameters subjected to one dimensional compression under confined state. The load path of the particulate assembly measured experimentally and simulated using PFC^{2D} for two initial porosity values is found to agree well until individual particle breakage initiates. Analytical aspects of the particle breakage behavior are explored using the contact forces developed in an assembly at a given stress level and by the average particle coordination number. The effect of non-circular particle shape on initial state of packing and the stress-strain

distribution of assemblage is analyzed by developing suitable PFC^{2D} models using a two-ball clump logic for generating particles with different shape parameters.

Keywords: Distinct Element Method, PFC^{2D}, Axial-Torsional Load Unit, one dimensional compression, particle crushing, coordination number.

INTRODUCTION

The behavior of granular media is of fundamental importance to many problems in geotechnical engineering. Traditionally, finite-element or finite-difference methods are commonly used in geo-mechanics to model the complex responses of granular media [1-3] subjected various types of loading. In these methods, the material is idealized as a continuum that obeys a constitutive (stress-strain) relationship. However, developing an appropriate stress-strain law for granular material to realistically model the macroscopic assemblage behavior is difficult, and the existing formulations are often plagued by the complexity with many obscure model parameters without an ability to quantitatively describe them in a rational framework. Moreover, granular material behaves in complicated ways for specialized loading conditions such as liquefaction commonly observed in loose sands under dynamic loading conditions, and it is necessary to model such behavior accurately. This mechanism, and many others, depends on the particulate nature of sand, the packing of grains as well as the nature of contacts formed in an assembly, and the associated volume change behavior (contractive or dilative).

It is recently proposed that a better understanding of such granular media may be achieved by replacing continuum methods with distinct element or discrete particle based approach [4-6]. With these recently evolving non-continuum methods, assemblies of discrete particles appear to capture the complicated behavior under realistic loading conditions with simple assumptions and few parameters to describe constitutive behavior between two particles or between a particle and a boundary at the element level. The distinct element method (DEM) as described by Cundall and Strack [7-10] is a particular implementation of such discrete-element methods that allow finite displacements and rotations of discrete bodies, including complete detachment, and recognize new contacts automatically as the calculation progresses. Through the coding in PFC^{2D}, which is developed on the concept of distinct element method (DEM), the movement and interaction of circular particles can be modeled. A detailed description of the code can be found in [11].

In this research, the micromechanics associated with 1-D compression under confined conditions on granular materials are analyzed using the simulations from two dimensional distinct element method implemented in PFC^{2D}. The strain versus stress evolution is recorded and the behavior associated with packing and particle shape dependencies are analyzed. For the simulation purposes, the actual particle mechanical properties such as hardness, stiffness, and modulus obtained from the nanoindentation technique were used for generating the model.

CALIBRATION OF NUMERICAL CODE AND PARTICLE PARAMETERS

The research herein focuses on evaluating the quantitative assessment of granular mechanical behavior subjected to 1-D compression using distinct element method. A series of controlled laboratory experiments were performed on Ottawa sand with known particle parameters and the experimental stress strain behavior was compared with the PFC^{2D} simulations as a first step of generating the suitable model for further analysis of size dependency, shape, and packing effect of the granular assembly. A quantitative analysis of the crushing behavior of Ottawa sand particle assembly initially in loose state were also made based on the experimental and numerical responses. Laboratory experimentation of 1-D compression test under confined condition were performed on Ottawa sand using a custom compression cell having a diameter of 19 mm and height of 19 mm (Figure 7.1) and the stress-strain behavior was compared with the previous test results on the same sand using a much larger chamber [12] to ensure that boundary effects are minimal. This cell (Figure 7.1) provides a diameter corresponding to 20 times diameter of particle and is adequate for minimizing boundary effects to simulate 1-D compression. For all the tests performed, a 19 mm sample diameter was used with corresponding sample height of 19 mm, irrespective of initial packing which was quantified using porosity values. For laboratory experimentation, the vertical stress was applied through an MTS 858 Table Top Servo-Hydraulic System with the Series 359 Axial-Torsional Load Unit that has a configuration for testing under axial load up to 25 kN with standard displacements of ±100 mm (Figure 7.2). The TestStar *IIm* digital controller features a data acquisition rate of 6 kHz and uses the multitasking Windows NT operating system that allows running tests and analyzing data simultaneously. This

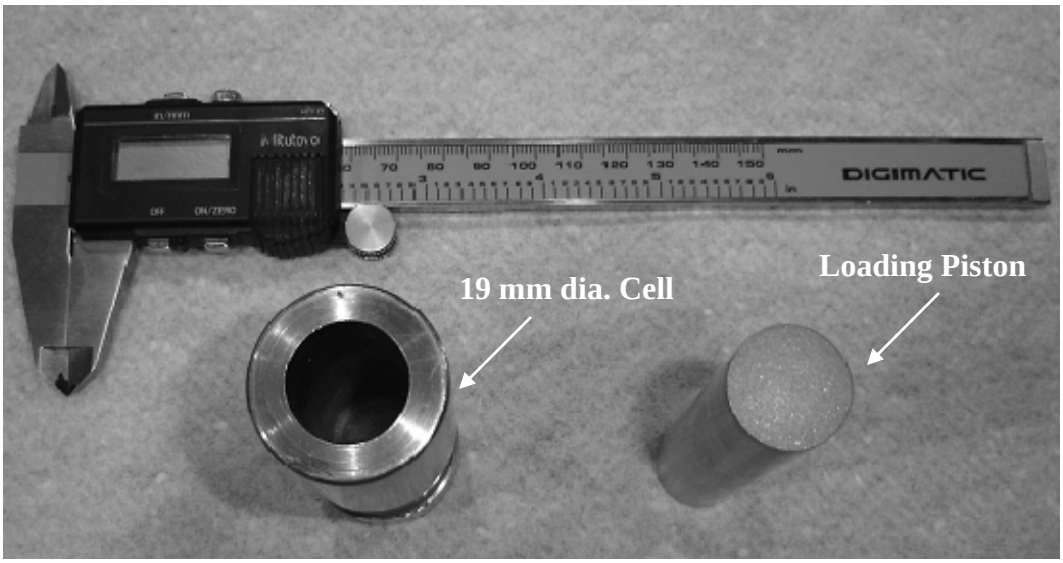

Figure 7.1: Photograph of the 19 mm diameter specimen cell.

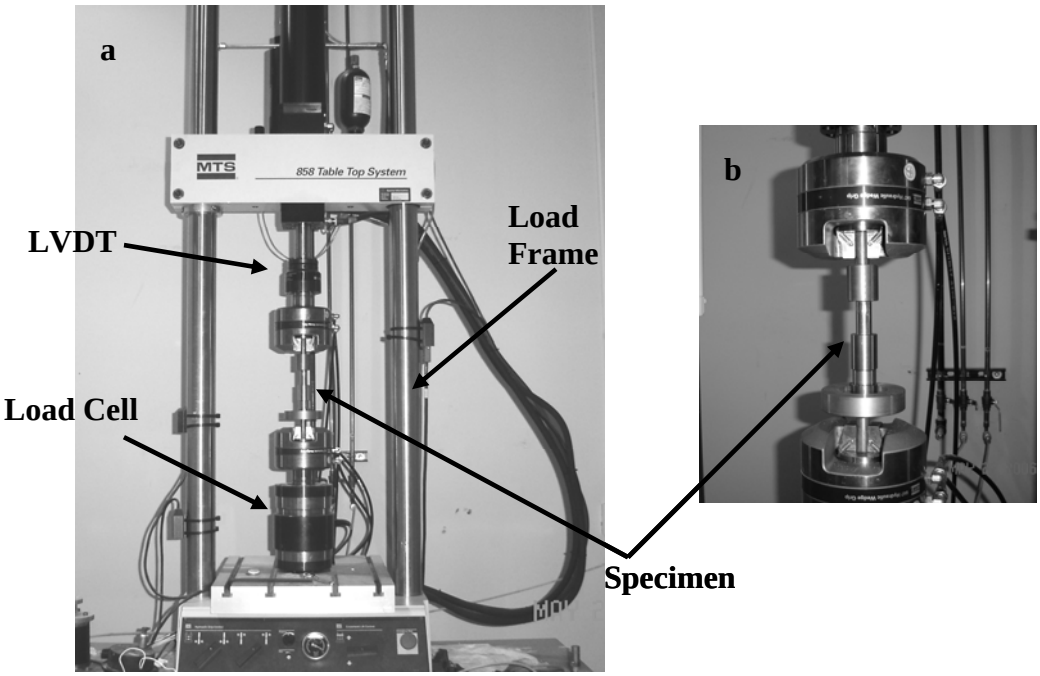

Figure 7.2: (a) Photograph of the MTS 858 Table Top System with the Series 359 Axial-Torsional Load Unit, (b) photograph of the enlarged view of the specimen cell.

testing system provides various digital control modes, such as the proportional, integral, and derivative (P.I.D.) control, channel limited channel control and dual compensation control to have precise automated control of the axial and torsional load or corresponding displacement. Tests were performed by setting zero torsion and a constant load was applied up to a maximum stress level of 85 MPa (considering the maximum capacity of the load cell).

DEM Simulation and particle micro parameters:

The compression cell used for simulation through PFC^{2D} is defined by four walls, having a width of 19 mm and a height of 19 mm. A compacted assembly of arbitrarily placed particles was generated by the radius expansion method to fill the cell. To calibrate the cell parameters by comparing the stress-strain response of the model with the laboratory results for the granular material assembly representing Ottawa sand, the particles are numerically generated with emphasis on initial particle size and shape. Table 7.1 shows single particle material properties for sub-rounded Ottawa sand (Ottawa 20-30) as per the study of McDowell and Bolton [13] and Nakata et al. [14, 15]. In PFC^{2D}, the basis for simulation is circular disk, which however may be grouped into clumps to obtain a specific aspect ratio. Thus to simulate Ottawa sand, clumps were created that consists of two overlapping balls. However, for simplicity the aspect ratio chosen for generating the clumps was 1.25 instead of actual measured aspect ratio of 1.22 for Ottawa sand (Table 7.1). The SEM image of the Ottawa sand particles (Figure 7.3) also confirms that the chosen aspect ratio of 1.25 is reasonable. In addition, to study the shape effects,

Table 7.1: Summary of Ottawa sand properties

Sand	D_{50} (mm)	C_u[1]	C_c[2]	G_s[3]	Roundness[4]	Aspect ratio[5]	Fracture Strength[6] (Mpa)
Ottawa 20-30	0.74	1.06	0.98	2.64	0.43	1.22	12.8

[1] $C_u = D_{60}/D_{10}$ (ASTM D2487-93), [2] $C_c = D_{30}^2/(D_{10}*D_{60})$ (ASTM D2487-93), [3] AASHTO T133,
[4]Roundness = Perimeter^2/4*p*A, [5]Aspect Ratio = Major axis/ Minor axis,
[6]Fracture Strength = Force at failure/diameter^2. (McDowell and Bolton 1998)



Figure 7.3: SEM image of Ottawa sand particles.

simulations were also performed based on particle aspect ratio of 1.0 (i.e. perfect circular disk) and 1.5.

Clump Logic and particle density parameter:

The basic idea followed for generating the clumps is given below.

First, a compacted assembly (with required packing) of arbitrarily placed circular particles was generated by radius expansion method to fill the cell. The particle diameter range chosen was between 0.73 mm and 0.75 mm to represent Ottawa sand used in the present research. In the next step, each circular particle was deleted and replaced by a two-particle clump of the specified aspect ratio having the same co-ordinates for its center. The radius of the two particles in each clump was set equal to

$$R_c = R_d * cfac\,, \tag{7.1}$$

where, R_d is the original particle radius and *cfac* is the factor chosen such that the area of the clump created is equal to the area of the original particle. Similarly, the density of the two particles in each clump was chosen in such a way that the weight of the clump and the original particle remains the same. The key thing to note here is that the mass of a clump is equal to the sum of the masses of all of the particles in the clump. The factor that multiplies the density (*dens_mfac*) was obtained by equating the weight of the original particle is given by Equation 7.2.

$$W_d = \rho_d g \pi R_d^2 t \tag{7.2}$$

(where, ρ_d and R_d are the density and radius of the original particle, t is the particle thickness in 2D simulations, and g is the gravitational acceleration).

The weight of the clump is given by Equation 7.3.

$$W_c = \left(\rho_c \pi R_c^2 + \rho_c \pi R_c^2\right) tg \tag{7.3}$$

(where ρ_c and R_c are the density and radius of the two particles in each clump). The density multiplication factor was obtained by the relation:

$$\rho_c = \rho_d * dens_mfac\,. \tag{7.4}$$

This is to be noted that a very precise measurement of the two factors *cfac* and *dens_mfac* are necessary to achieve the required initial packing as well as to reach equilibrium. Considering their importance, a detail step-by-step calculation for choosing appropriate factors (i.e. *cfac* and *dens_mfac*) for creating a 2-ball clump with aspect ratio 1.25 is shown below:

Figure 7.4, shows a two particle clump with each particle having radius R. The clump aspect ratio is

$$\psi = {H_c}/{W_c} = {5R}/{4R} = 1.25\,. \tag{7.5}$$

Computation of overlap area, A_o:

$$A_o = 4A_4\,. \tag{7.6}$$

$$A_4 = A_s - \Delta A_t\,. \tag{7.7}$$

$$\sin\phi = {R_4}/{R} = {1}/{4} \tag{7.8}$$

$$\phi = \sin^{-1}\frac{1}{4} \tag{7.9}$$

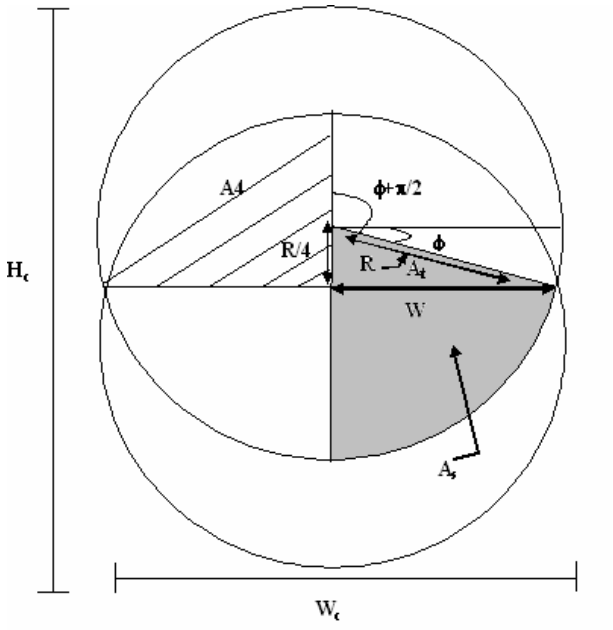

Figure 7.4: Schematic diagram of two particle clump with aspect ratio 1.25.

$$A_s = \int_{\phi+\pi/2}^{\pi} \frac{R^2}{2} d\theta = \frac{R^2}{2}\left[\frac{\pi}{2} - \phi\right] \tag{7.10}$$

And, $$\Delta A_t = \frac{1}{2} W \frac{R}{4} = \frac{R}{8}\left(R\cos\phi\right) \tag{7.11}$$

$$A_o = 4A_4 = 4(A_s - A_t) = 4\left[\frac{R^2}{2}\left(\frac{\pi}{2} - \phi\right) - \frac{R^2}{8}\cos\phi\right] \tag{7.12}$$

So, the area of clump

$$A_c = 2\pi R^2 - A_0 = R^2\left[2\pi - 2\left(\frac{\pi}{2} - \phi\right) + \frac{\cos\phi}{2}\right] \tag{7.13}$$

$$or, A_c = 4.131076082\,. \tag{7.14}$$

Given one disk of radius R_d, the radius of the two balls comprising a clump, R_c with Ψ = 1.25 that has same clump area as disk area (Figure 7.5) was computed by setting $A_d = A_c$ and solving for R_c such that

$$\begin{aligned} &A_d = A_c \\ &or, \pi R_d^2 = 4.131076082\, R_c^2 \\ &or, R_c = 0.872053922 R_d\,. \end{aligned} \tag{7.15}$$

So, the chosen factor, *cfac,* for the two balls clump in this study with aspect ratio = 1.25 is 0.872053922. Using similar logic, the *cfac* factor for the two ball clump with aspect ratio = 1.50 is calculated as 0.788355818.

Using Equations 7.2, 7.3 and 7.4, the density factor, *dens_mfac*, was calculated for the two ball clump with aspect ratios 1.25 and 1.50. From Table 7.1 it is noticed that

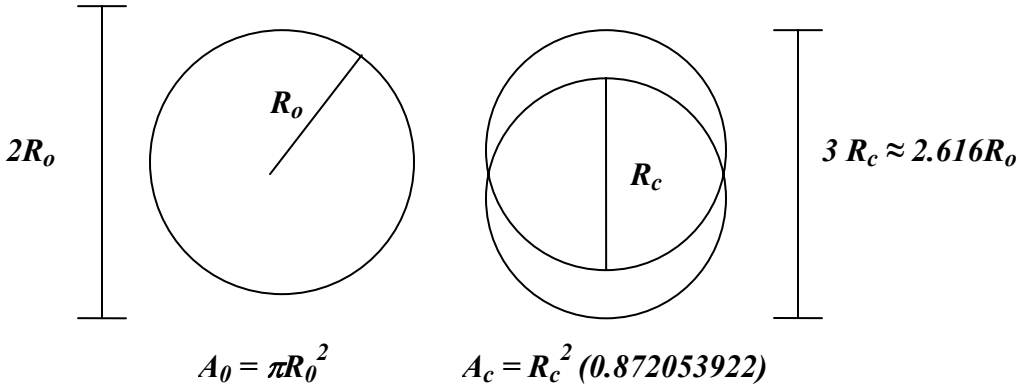

Figure 7.5: Schematic diagram showing a disc and a two ball clump (aspect ratio 1.25) with same area.

the density of the Ottawa sand particles is 2640 kg/m^3. Considering the particles in the clump are of unit thickness, the density of the disks in the clump can be calculated by setting $W_d = W_c$ such that

$$\rho_d g \pi R_d^2 = 2\rho_c g \pi R_c^2 \tag{7.16}$$

$$or, \rho_c = \frac{1}{2}\left(\frac{R_d^2}{R_c^2}\right)\rho_d \tag{7.17}$$

$$\rho_c = 0.657481178\rho_d \tag{7.18}$$

So, the chosen factor, *dens_mfac,* for the two balls clump with aspect ratio = 1.25 was 0.657481178. Using similar logic, the *dens_mfac* for the two ball clump with aspect ratio = 1.50 was calculated as 0.80449889.

The clump logic provides a means to simulate and analyze the behavior of shape dependency of particle assembly. The clumps behave as a rigid body with deformable

boundary, and are assumed to be unbreakable regardless of the forces acting upon it. Initially, because of the random generation of the circular balls with subsequent replacement by the two balls clumps, the generated clumps remain at fixed distances from each other and there may be some extent of overlap causing large contact forces between them. So, after the clumps have been created, the model is allowed to reach the state of balanced forces where clumps are separated to reach equilibrium. Once the equilibrium has been reached, gravity and frictional coefficient of particles were applied to reach a new state of mechanical balance (i.e. the in situ state of state), and the assemblage is ready for numerical experiments.

Packing of assembly:

The desired porosity of the assembly is maintained throughout the process and checked by constructing the measurement circles at different location within the assembly. The porosity is measured as the ratio of the area of voids between balls/clumps within the model to the total area of the model. In this research, the assembly is simulated considering a dense state of assembly and a comparatively loose state of initial porosity. For calibration purposes, the experimental analysis results on Ottawa sand at two different porosity states (one dense and one comparatively loose state) were compared with the simulation results on the clump particle assembly with particle aspect ratio of 1.25. Besides, to calibrate the model, the experimental results on Ottawa sand assembly having a known porosity of 37.13 percent (i.e. equivalent to 65% of relative density) were also compared with a previously reported study on the same sand material [12]. This is to be noted that the PFC^{2D} model is two-dimensional and there is no clear

relationship exists between the 2D porosity for a packing of disks and the 3D porosity of a packing of spheres. It is shown by Deresiewicz [16] that the closest packing of uniform spheres in 3D has a porosity of 0.2595, while the corresponding close packing of uniform circles in 2D has a porosity of 0.0931. Moreover, in PFC^{2D}, a fully packed uniform circular particle assembly with zero friction corresponds to a porosity of 0.16 [11]. Considering the above and the shape factor of particles, the desired 3-D porosity value of 0.3713 (equivalent to 65% relative density) was modeled in PFC^{2D} with 2-D porosity of 0.22. Experiments on dense state of Ottawa sand through MTS 858 Table Top System was performed and the results were compared with numerical response through PFC^{2D} for the assembly using a 2-ball clump logic with particles having aspect ratio of 1.25. The 3-D porosity of dense state of the Ottawa sand assembly attained in the laboratory for the experimental analysis was 0.3355 percent. The corresponding dense state porosity for numerical analysis modeled was 0.20. For two ball clump assembly with an aspect ratio of 1.50, the corresponding dense and loose state numerical analysis were performed with PFC^{2D} having approximately similar porosity values of 0.21 representing a dense and 0.23 representing loose state. Similarly, the numerical analysis for perfectly circular particle assembly (i.e. aspect ratio = 1.00) were conducted having 2-D porosity values of 0.16 and 0.18 respectively for the dense and a comparatively loose state. The above mentioned porosity criteria for the circular and clump particle assembly with an aspect ratio of 1.50 were chosen based on the porosity calibration of the clump assembly having particle aspect ratio of 1.25 and by performing several simulations on the given assembly and analyzing the particles in contact. The dense state of a given assembly with a specific particle aspect ratio is finally chosen based on minimum void ratio achievable with

minimal particle overlapping. The comparatively loose state was chosen with a difference of approximately two percent in porosity from the dense state so as to capture the packing effect with such slight departure of porosity from its dense state as well as to maintain similarity of the two different porosity states of the calibration material such as Ottawa sand.

Normal and Shear Contact Stiffness parameters for modeling

In PFC^{2D}, Particle-particle contact is characterized using a soft-contact approach in which a finite stiffness is taken to represent the measurable stiffness that exists at a contact. The relation at the level of a single particle-particle contact can be derived by comparing the behavior of the contact to that of an elastic beam with its ends at the particle centers. The beam can be considered to be loaded at its ends by the corresponding force and moment vectors acting at each particle center. The beam is characterized by: (1) the geometric parameters of length (L), cross-sectional area (A) and moment of inertia (I); and (2) the deformability parameters of Young's modulus (E) and Poisson's ratio (v). The Young's modulus of a particle-particle contact is designated by E_c. In addition, it is assumed that all particles in PFC^{2D} are being treated as disks of thickness t. If we designate the two particles at the particle-particle contact as A and B, then the beam radius can be expressed as the average of the two particle radii:

$$\tilde{R} = \frac{R^{[A]} + R^{[B]}}{2} \tag{7.19}$$

and the beam length can be expressed as

$$L = 2\tilde{R} = R^{[A]} + R^{[B]}. \tag{7.20}$$

The beam cross-sectional area and moment of inertia can be expressed using Equations 7.21 and 7.22.

$$A = 2\tilde{R}t, \quad \text{(for 2-D representation)} \tag{7.21}$$

$$I = \frac{1}{12} t(2\tilde{R})^3, \quad \text{(for 2-D representation)} \tag{7.22}$$

Deformability of Granular material in contact:

The deformability of an un-bonded (granular) material is described by the relations as discussed herein. The deformability relations described here pertain to a general particle-particle and particle-wall contact. For pure axial and pure shear loading, the normal and shear behaviors are uncoupled, and the contact normal and shear stiffness can be expressed as [17]:

$$k^n = \frac{AE_c}{L} \tag{7.23}$$

$$k^s = \frac{12IE_c}{L^3} \tag{7.24}$$

where E_c is the "contact Young's modulus". For the linear contact model, the contact stiffness, k^{ξ}, is computed assuming that the stiffness of the two contacting particles, $k_{\xi}^{[A]}$ and $k_{\xi}^{[B]}$, act in series such that

$$k^{\xi} = \frac{k_{\xi}^{[A]} k_{\xi}^{[B]}}{k_{\xi}^{[A]} + k_{\xi}^{[B]}} \tag{7.25}$$

where $\xi = \{n, s\}$ (PROPERTY: normal stiffness, $kn = k_n$; shear stiffness, $ks = k_s$). If the two particles have the same normal and shear stiffness,

$$k_n = k_n^{[A]} = k_n^{[B]} \tag{7.26}$$

$$k_s = k_s^{[A]} = k_s^{[B]} \tag{7.27}$$

then the relation between these stiffness and the modulus at a contact is found by substituting Equations 7.20 , 7.21 and 7.22 into Equations 7.23 and 7.24 to obtain

$$k_n = k_s = 2E_c t \tag{7.28}$$

The fact that the Poisson's ratio of the elastic beam is not present in Equation 7.28 demonstrates the lack of relation between Poisson's ratio and particle stiffness at the micro level. However, the value of the macroscopic Poisson's ratio can be related to the ratio, k_n/k_s , of normal to shear stiffness. This ratio also affects the proportion of load that is carried in the shear and normal modes at the contacts in an arbitrary assembly, and will thereby influence the macroscopic failure mechanisms. Thus, a consistent means of setting the deformability micro-parameters is to specify: (1) the Young's modulus at each particle-particle contact, E_c; and (2) the ratio of particle normal to shear stiffness, k_n/k_s.

Using nanoindentation technique a precise measurement of modulus for individual particle of Ottawa sand was obtained as 105 GPa [18] and is used to estimate the normal and shear contact stiffness of the particles for the simulation. Using Equation 7.28 and considering the ratio of k_n/k_s to be 1, the normal and shear contact stiffness for particles with thickness equivalent to particle diameter (0.74 mm) was found to be 1.554

e8 N/m. Considering the walls of the model are representing the experimental cell wall that is made up of stainless steel (with reported modulus ~ 200 GPa), the estimated normal and shear contact stiffness for walls used for simulation correspond to 1.0 e9 N/m.

Thus, the geometry of the model consists of square cell i.e. bounded by four walls to simulate the laboratory 1-D compression test, which was randomly filled with circular/arbitrary shaped particles. The constitutive contact law used in the simulation consists of two parts: the stiffness model – providing a linear elastic relation between contact force and contact relative displacement in normal and shear directions - and a slip model – which is defined by the friction coefficient (μ) at the contact, where μ is taken to be the minimum friction coefficient of the two contacting entities. The friction coefficient equal to 0.5 has been assigned for particles/particle and particle/walls in this simulation. However, the side walls of the model were represented as frictionless using interface property. The top wall of the model represents the loading platen, and the left, right and bottom wall acted as rigid cell walls. By applying a numerical subroutine (FISH function) that ramps up the velocity of the top wall (here treated as platen) in a controlled fashion, a strain controlled loading path to a maximum stress of 100 MPa was applied and the micromechanical behavior of the granular material with varying shape and packing were analyzed as below.

During simulation, the stress is computed by taking the out-of-balance force (*y*-component) acting on the top wall whereas the strain is measured using the relation

$$\varepsilon = \frac{L - L_0}{\frac{1}{2}(L_0 + L)}, \tag{7.29}$$

where, L is the current sample length in y-direction, and L_0 is the original sample length in that direction. The current sample height and width are used in both the stress and strain calculations.

RESULTS AND DISCUSSION

The simulation results in terms of macroscopic stress-strain behavior in 1-D compression under confined state for the clump particle assembly in loose state (i.e. porosity 22% in PFC^{2D}) with particle aspect ratio 1.25 is presented in Figure 7.6 and the data are compared with the experimental results on Ottawa sand (equivalent loose state with a 3-D measured porosity of 37.13%) as well as with the results obtained by using larger cell size on the same sand. It is noticed that the trend of the load path obtained under stress control using larger compression cell (63.5 mm in diameter and 20 mm in height) matches well with the experimental results performed in this study using strain control loading with smaller compression cell (19 mm in diameter with 19 mm in height). Strain control loading on smaller volume showed slightly higher fraction of volumetric strain compared to larger diameter specimen for vertical stress from 1 to 40 MPa. Typical repeatability of experimental results on Ottawa sand using specimen dimension 19 mm by 19 mm with load applied through MTS 858 under deformation control boundary condition is shown in Figure 7.7.

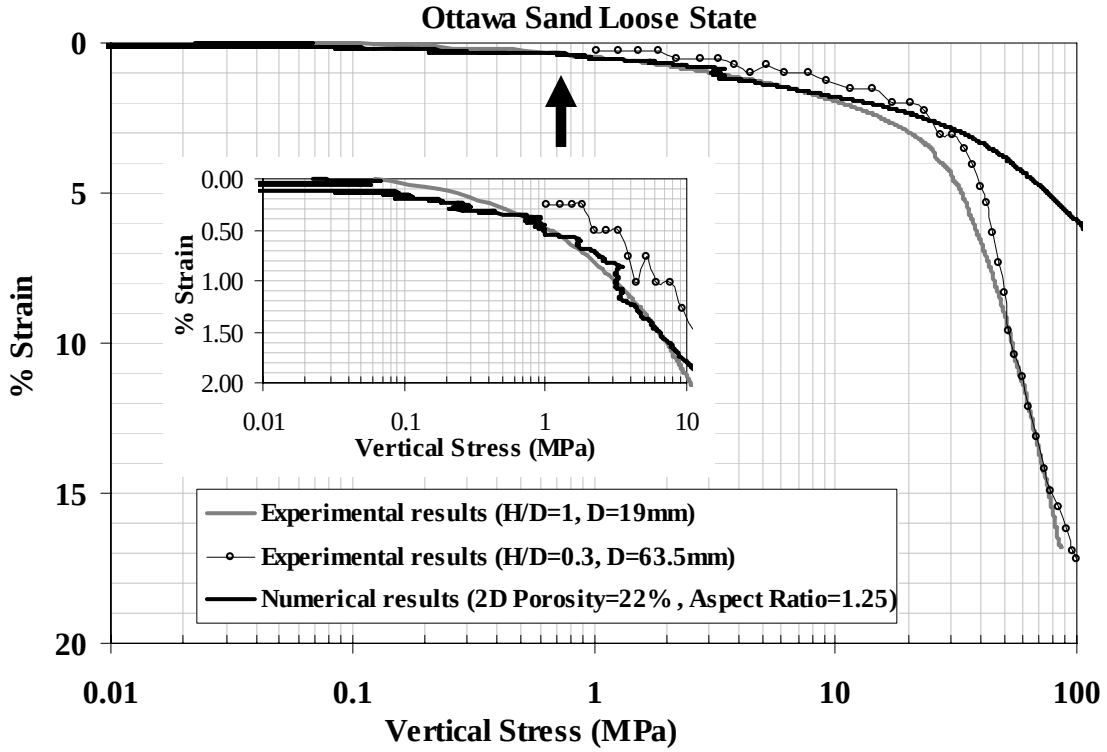

Figure 7.6: Comparison of numerical data with experimental results on Ottawa sand at loose packing state (with equivalent porosity of 37.13%). For numerical analysis Ottawa sand was represented using a 2-ball-clump logic with aspect ratio of 1.25.

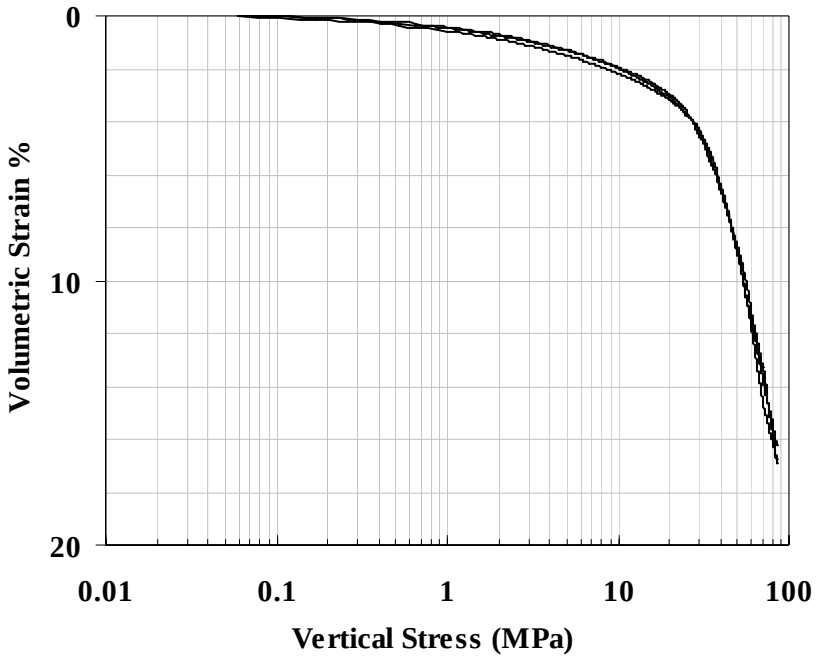

Figure 7.7: Plot showing stress-strain behavior for three repeatability tests performed on Ottawa sand (porosity, n_i = 37.13%) using specimen dimension 19 mm by 19 mm with load applied through MTS 858 under deformation control.

From Figure 7.6 it is also noticed that the stress path for the numerical analysis closely follows the experimental stress-strain behavior until the applied vertical stress of 9 MPa and beyond that stress level, the numerical analysis exhibits a stiffer behavior than the experimental one. It is to be noted that in simulation through PFC^{2D}, the particles are assumed rigid bodies and their mechanical interaction is characterized by using the so-called soft-contact approach where deformation of particle is allowed to take place at the contacts. But it does not allow particle breakage. Thus, the numerical analysis response shows the behavior of the particles at the elastic region and the higher strain in the experimental results is mainly due to the particle breakage. The comparative analysis of stress-strain behavior between experimental and numerical analysis in Figure 7.6 thus suggests that the particle breakage initiated at 9 MPa applied vertical stress. Figures 7.8a through 7.8f show the force distribution chain of the assembly at different vertical stress along with the maximum compressive force experienced by a particle at a given stress level. The black lines represent the resultant forces at contacts and thickness of these lines is proportional to the magnitude of the contact force. It is observed that the maximum force on a particle at 9 MPa applied vertical stress (when the particle breakage is interpreted to initiate) is 673 Newton for initially loose state of packing (porosity, n_i = 22 %) and for an assumed thickness of 19 mm for disks.

Figure 7.9 illustrates the experimental behavior of Ottawa sand assembly at an initially dense state of porosity (35.7 %), and the results are compared with the numerical analysis data of such assembly (equivalent PFC^{2D} porosity of 20 %) with clump particles having aspect ratio of 1.25. The comparison of stress path between numerical and

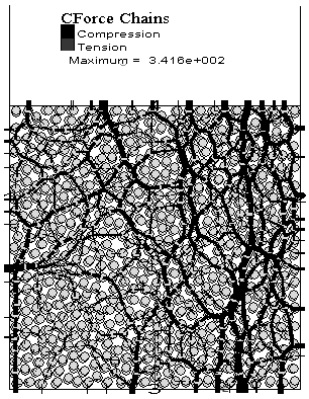

Figure 7.8a: Stress 5 MPa

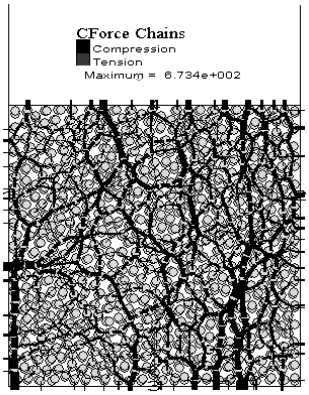

Figure 7.8b: Stress 9 MPa

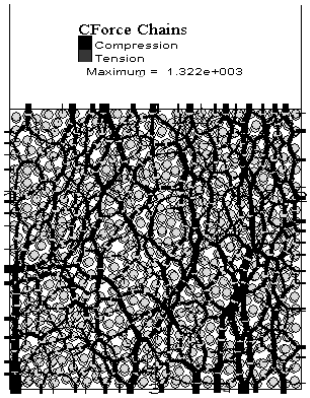

Figure 7.8c: Stress 25 MPa

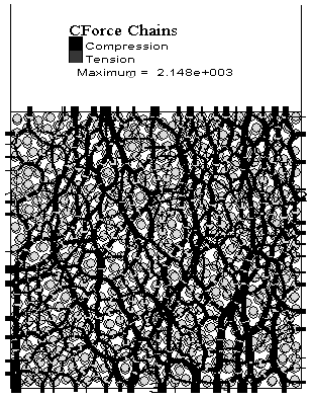

Figure 7.8d: Stress 50 MPa

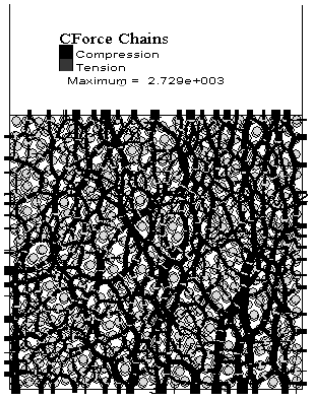

Figure 7.8e: Stress 75 MPa

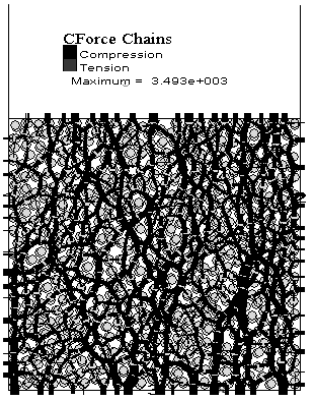

Figure 7.8f: Stress 100 MPa

Figure 7.8: Behavior of contact force distribution for 2-ball clump (aspect ratio 1.25) particle assembly at loose state (PFC^{2D} porosity 22%) with different applied stress level; (a) 5 MPa stress, (b) 9 MPa stress, (c) 25 MPa stress, (d) 50 MPa stress, (e) 75 MPa stress and (f) 100 MPa stress.

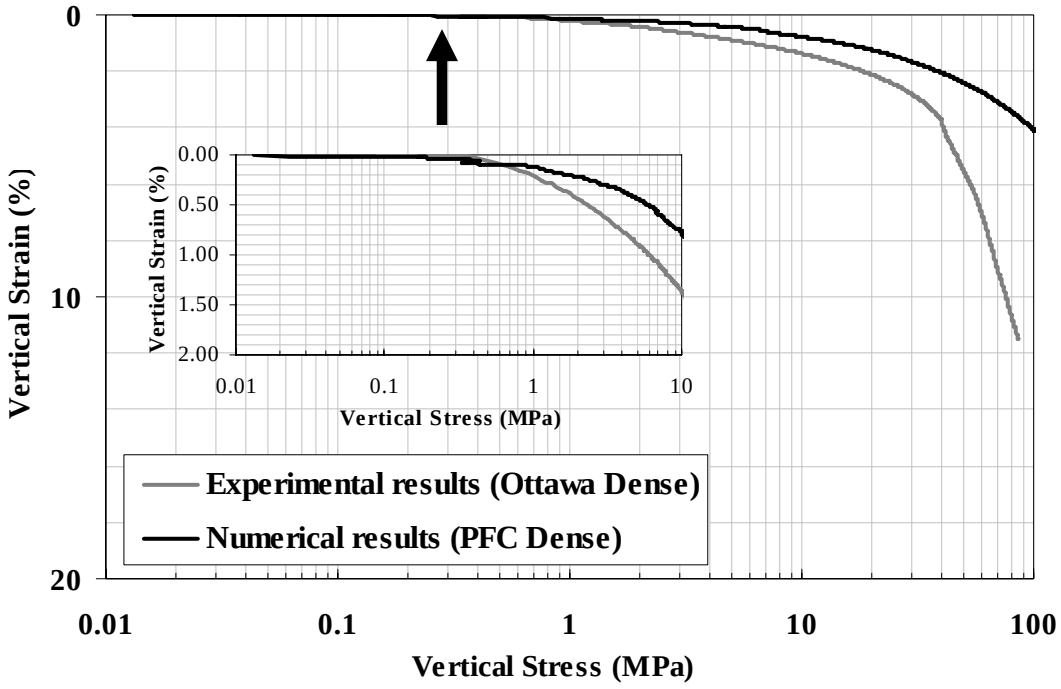

Figure 7.9: Comparison of numerical data with experimental results on Ottawa sand at dense packing state (with equivalent porosity of 35.66%). For numerical analysis Ottawa sand was represented by 2-ball-clump particle assembly with particle aspect ratio 1.25.

experimental analysis suggests that the particle breakage for the dense state initiated at 1 MPa applied vertical stress. The corresponding contact force distributions within the assembly at different applied stress level are shown in Figure 7.10. It is noticed that the maximum contact force at 1 MPa applied stress when particle breakage starts for this dense assembly is 268 Newton. From the foregoing discussion on stress path for the dense and loose assembly, it is seen that the particle breakage for dense assembly was initiated at much lower stress level (approximately at 1 MPa stress) compared to the loose state based on differences between PFC^{2D} and experimental results. The maximum compressive force a particle experienced at that state (dense assembly) was 268 N compared to the maximum compressive force of 673 Newton at the loose state. However, Figures 7.6 and 7.9 also illustrate that for the dense assembly though particle breakage initiated at lower compressive force, the overall volumetric strain is smaller than the corresponding loose assembly at a given stress level. The particle breakage phenomena for the two different assemblies discussed here can be explained by the number of particle contacts (coordination number) in the assemblies. With discrete contacts existing at particle-particle contacts, the contact stress is an order of magnitude higher than the applied global stress which is evident from the contact force distribution shown for the different assemblies in Figures 7.8 and 7.10. In the loose state, due to the presence of higher void space in the assembly the particles are reoriented constantly with applied stress and consequently maintain higher coordination number and thus higher compressive force needed for initiation of particle breakage. In contrary to the loose state, the particles in the dense state have little space for rearranging their position with a given applied stress level and thus particle failure initiates with lower compressive force for

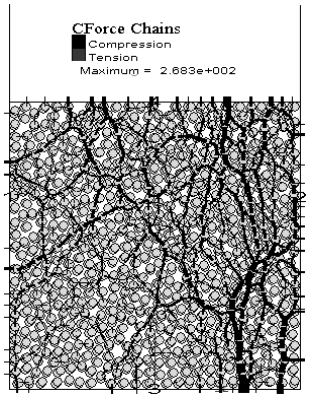

Figure 7.10a: Stress 1 MPa

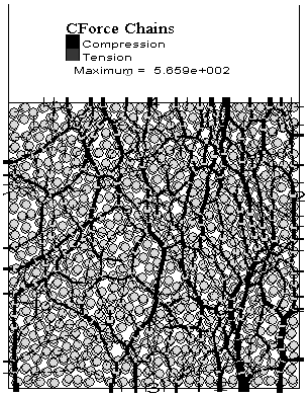

Figure 7.10b: Stress 5 MPa

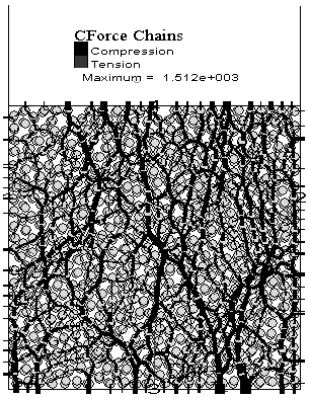

Figure 7.10c: Stress 25 MPa

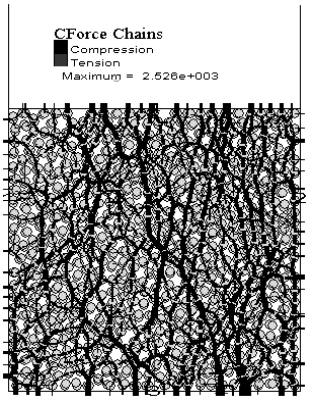

Figure 7.10d: Stress 50 MPa

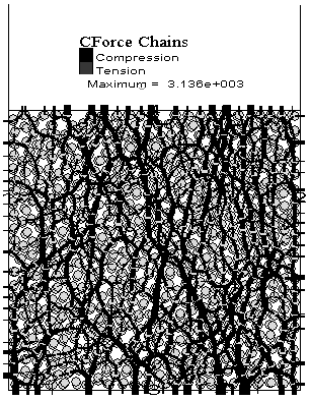

Figure 7.10e: Stress 75 MPa

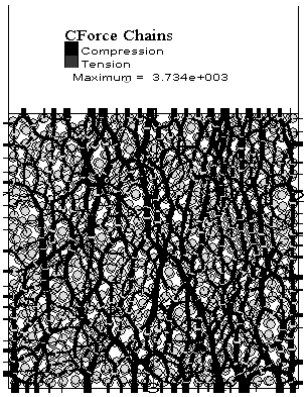

Figure 7.10f: Stress 100 MPa

Figure 7.10: Behavior of contact force distribution for 2-ball clump (aspect ratio 1.25) particle assembly at Dense state (PFC^{2D} porosity 20%) with different applied stress level; (a) 1 MPa stress, (b) 5 MPa stress, (c) 25 MPa stress, (d) 50 MPa stress, (e) 75 MPa stress and (f) 100 MPa stress.

those particles that has lower coordination number. However, owing to smaller void ratio in the dense assembly, the overall number of particle contacts increases, which results in a more stable structure that has greater resistance to crushing. Therefore, higher overall straining is noticed for the loose state in contrary to the dense state at any given stress level. The average coordination number of the assembly for the loose and dense state at different stress level is shown in Figure 7.11. The definition of coordination number adopted here is

$$C.N. = \frac{2N_C}{N_p} \tag{7.30}$$

where N_C is the number of contacts and N_p is the number of clumps/particles. For simulations, the particles are considered rigid, the coordination number at different stress level shown in Figure 7.11 is the resultant response of the elastic behavior of the clump particles at the respective stress magnitude. It is seen that at lower stress level (up to 5 MPa) the coordination number for the loose assembly increases at higher rate than the corresponding dense state. An increase of approximately 20% of the coordination number is noticed for the stress level increases from 1MPa to 5MPa stress for loose state of assembly, whereas for the same stress level change the dense state coordination number increases only about 6%. This justifies that the particles at the loose state are reoriented at the initial stage of applied stress due to the availability of higher void space and attain a higher coordination number that requires initiation of particle breakage at higher compressive force, whereas the particles at dense state has little room for reorientation and consequently a smaller increase of coordination number and initiation of particle breakage at lower compressive force. It is also observed from Figure 7.11 that the

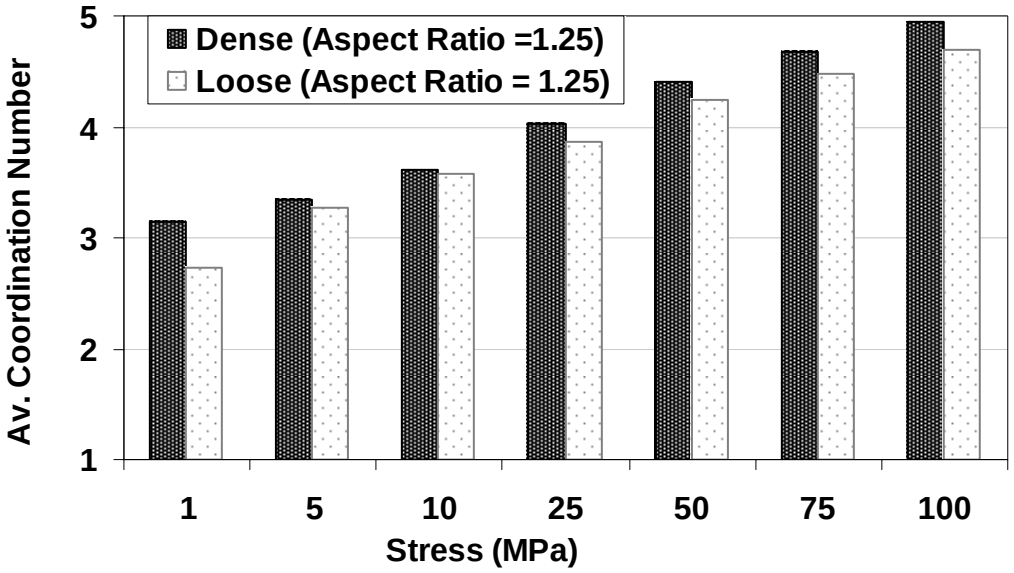

Figure 7.11: Variation of average coordination number at different applied vertical stress level for the loose and dense assembly of the clump particles with particle aspect ratio of 1.25.

coordination number for dense state is comparatively higher than the loose state at any given stress level suggesting greater material strength and smaller overall strain for the dense assembly with applied stress.

The maximum compressive force a particle experienced when particle splitting occurs thus observed by simulation in this study is 268 Newton and 673 Newton for dense state and loose state assembly respectively. In a previous study Nakata et al. [15] estimated the single particle strength of similar type of sand material based on experimental study. For silica sand with diameter range 1.4 to 1.7 mm, the maximum peak load, where major splitting of the particle occurred was reported as approximately 70N. From the particle crushing strength behavior described by Nakata et al. [15], the failure load for particles with a diameter of 0.75 mm can be estimated as 160 Newton

approximately. It is to be noted that the experimentation performed by Nakata et al. were conducted by placing the particle between hardened platens and then moving the lower platen at a constant rate of displacement to crush the particle. So, in their study the particle failure can be correlated with force application at two contact points, i.e. a coordination number equal to 2. In comparison to the experimental results by Nakata et al., the higher contact forces estimated for particle breakage through simulation in this study captured the actual particle behavior in the assembly and from Figure 7.11, it is clear that in both the dense state and loose state condition when particle breakage initiates, the corresponding average particle coordination number was over 3. The higher average coordination number thus justifies the higher contact forces needed for the initiation of particle breakage in two different porosity states.

Evaluation of particle shape effect (and corresponding packing state) on stress-strain behavior under one dimensional compression in a confined state was determined using simulations of assemblies comprising of circular (particle aspect ratio = 1.00) and clump particles having aspect ratios of 1.25 and 1.50 at two initial packing states (a dense and a comparatively loose) of the clumps as shown in Figure 7.12. The differences in strength as a function of packing are clearly seen here. It is noticed that the higher the packing, the stiffer the material assembly behavior. Figure 7.12 also clearly captured the shape effect of different particle assembly. The lowest vertical strain is observed for the circular particle assembly (particle aspect ratio 1.00) and highest strain percentage is noticed for the loose particle assembly having aspect ratio 1.50. The variation of the average coordination number with increasing vertical stress level for the respective

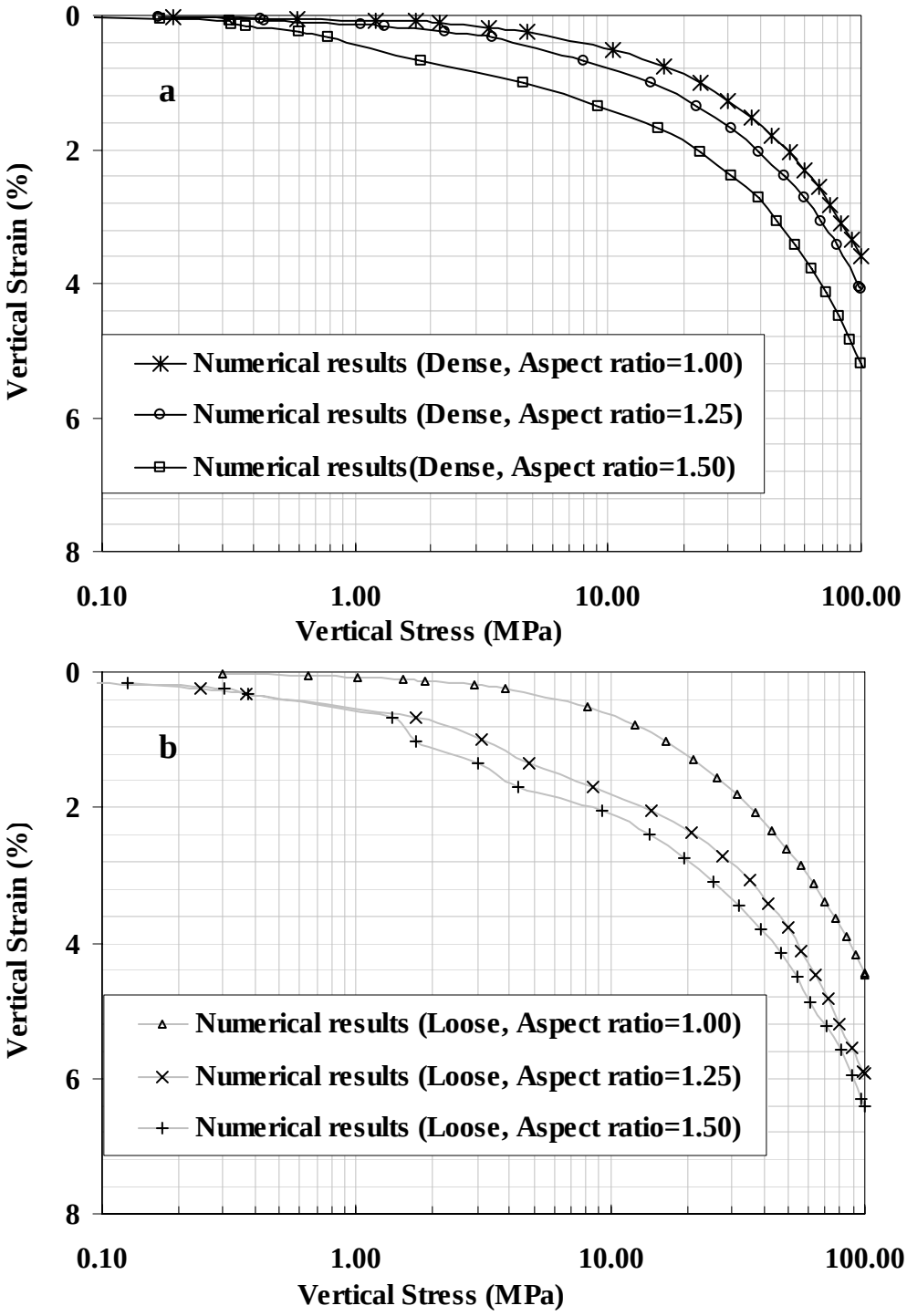

Figure 7.12: Variation of Stress-Strain distribution through numerical analysis on a (a) dense and (b) a comparatively loose particle assembly with particle aspect ratios of 1.0, 1.25 and 1.50.

assembly (dense and loose state) with different particle aspect ratios are shown in Figure 7.13. The repeatability of the average coordination number at different packing state of the assembly was checked based on three repeating simulations performed on the granular assembly at two different applied vertical stress i.e. at 5MPa and 75MPa stress level. Since PFC^{2D} produces identical results for a given assembly with same porosity, to check the repeatability, a 0.05% porosity variation was artificially introduced for respective dense and loose state of assembly. For example, the dense state was simulated with three different porosities like 15.95%, 16% and 16.05%. Figure 7.14 shows the variation of the average coordination number at 5 MPa and 75 MPa applied stress level along with error bars. Considering ± 0.05% porosity variation in the assembly for a particular packing state, the results in Figure 7.14 shows acceptable repeatability.

As expected, Figure 7.13 shows that the average coordination number at the dense state is comparatively higher than the corresponding loose state for any types of assembly. However, the interesting point to note is that the differences of the coordination number for the two porosity states of the respective assembly is reduced gradually as the particle shape changes from circular to higher aspect ratios and in case of particle aspect ratio 1.50, this difference is almost negligible. Using the theory of contact force distribution based on macroscopic state of the stress [19], an average value of the normal contact forces (F_n) in the assembly can be obtained such that

$$F_n = \frac{\pi \sigma D^2}{6 N_c \rho}, \tag{7.31}$$

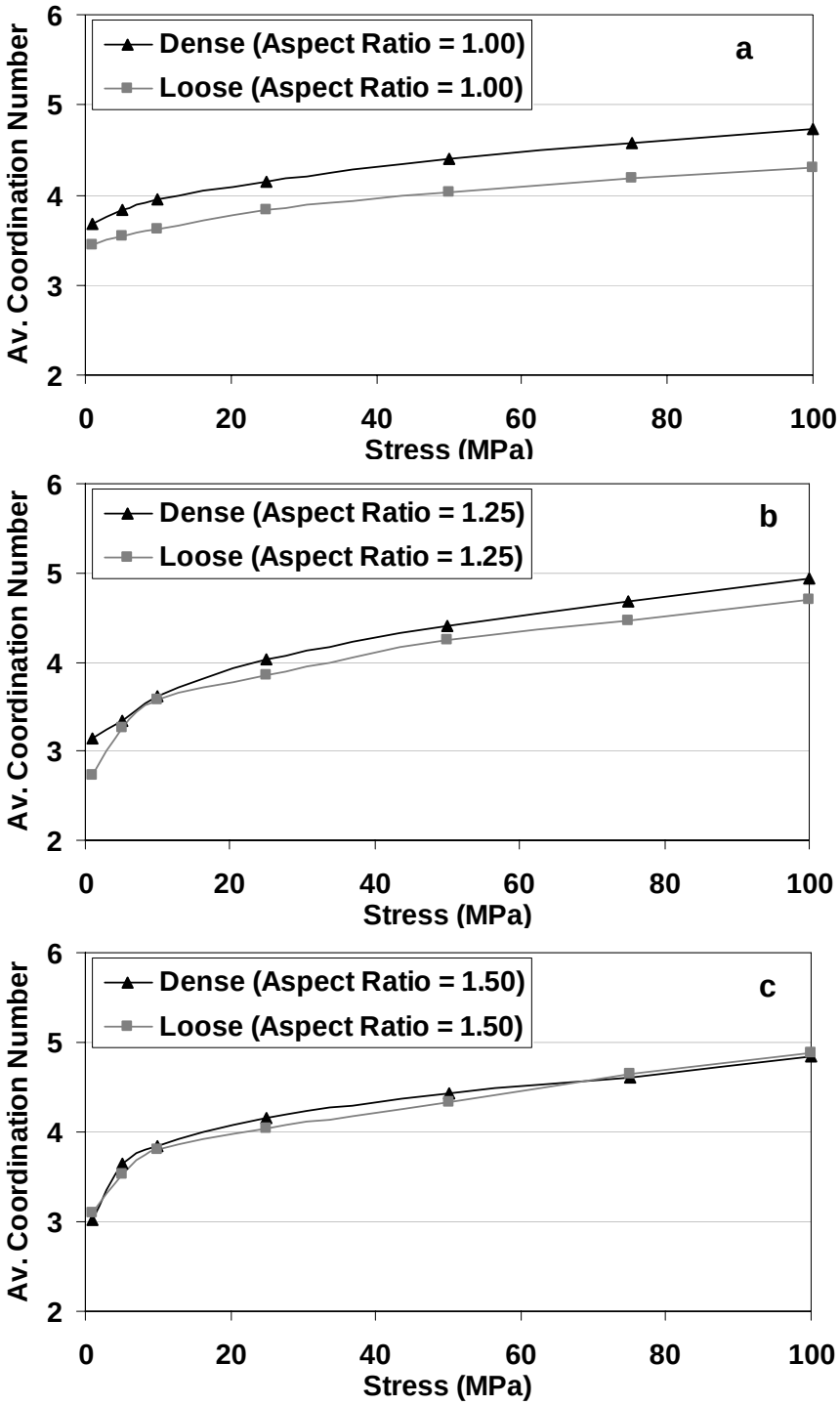

Figure 7.13: Variation of average coordination number at different applied vertical stress level for the loose and dense assembly with (a) circular particle (aspect ratio of 1.0), (b) particle aspect ratio of 1.25 and (c) particle aspect ratio of 1.50.

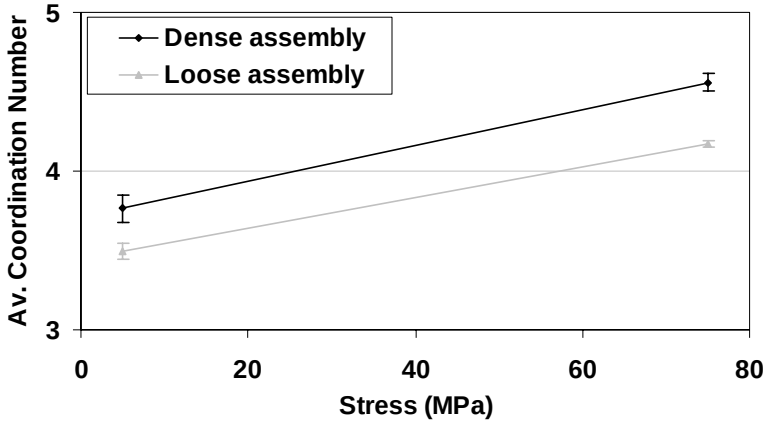

Figure 7.14: Variation of average coordination number at dense and loose state of circular particle assembly (Particle aspect ratio 1.00) at the applied vertical stress of 5MPa and 75MPa. The error bars shown here incorporates the ±0.05% porosity variation around the respective dense and loose state of assembly.

where, σ is the normal pressure acting on the assembly, D is the particle diameter, N_c is the particle coordination number and ρ is the packing fraction. Equation 7.31 implies that other parameters being constant, the average normal contact force will decrease with increasing coordination number and therefore provide greater strength to the assembly. So, for an assembly consisting of rounded particles, the dense state will provide greater strength than the corresponding looses state due to the higher coordination number and consequently higher contact forces needed for particle failure. In contrast, for assemblies with particles having aspect ratio larger than 1.0, for example those with aspect ratio of 1.50, the average value of coordination number is not sufficient to explain the breakage behavior of the different assembly packing. In such cases, given other parameters are same, the angle and direction of contact force vectors, nature of rearrangement of particles at every step of global stress change, and the corresponding coordination number at particle level will be more important for particle failure to initiate. Asperity

breakage is more likely to initiate first before a complete particle failure occurs for such types of assemblies with particles having higher aspect ratio.

CONCLUSION

DEM simulations were conducted in similar samples of granular material in order to compare results with experimental response and analyze the crushing behavior of particles. The effect of initial packing (a dense state and a comparatively loose state), and particle shape (with three different particle aspect ratios: 1, 1.25 and 1.50) were evaluated using numerical simulations. For generating the model in numerical analysis, true particle micro-properties were assigned from nanoindentation and elastic beam theory. The contact stiffness of the particles assigned for the numerical simulations were obtained from the measured values of the elastic modulus through nanoindentation technique. Particles with different shape were generated using clump logic and the details of the logic were described.

A comparative stress-strain analysis of Ottawa sand subjected to one dimensional compression under confined state through DEM and laboratory experimentation revels that the particle breakage which is initially dense, initiates when the applied vertical stress reaches 1 MPa where as particle breakage in a comparatively loose state of assembly did not initiate till the stress reached a value of 9 MPa. The maximum contact force a particle experienced for failure to occur at dense state obtained from numerical analysis is approximately 268 Newton. The corresponding maximum compressive contact force for the loose state is measured approximately as 673 Newton. Though the

breakage of the dense assembly starts at much lower stress level than the loose state, the overall volumetric strain for dense state of packing is lower than the corresponding loose state. The reason behind this phenomenon is described quantitatively through numerical analysis from the view point of average coordination number of particles in different state of the assembly. In the loose state, due to the presence of higher void space in the assembly the particles are reoriented constantly with applied stress and consequently maintain higher coordination number and thus higher compressive force needed for initiation of particle breakage. In contrary to the loose state, the particles in the dense state has little space for rearranging their position with a given applied stress level and thus particle failure initiate with lower compressive force for those particles that has lower coordination number. However, owing to smaller void ratio in the dense assembly, the overall number of particle contacts increases, which results in a more stable structure that has greater resistance to crushing. Therefore, higher overall straining is noticed for the loose state in contrary to the dense state at any given stress level.

Evaluation of particle shape effect and corresponding packing state on stress-strain behavior under one dimensional compression in a confined state was determined using simulations of assemblies comprising of circular particle (aspect ratio of 1.0) and clump particles having aspect ratios of 1.25 and 1.50 at two initial packing states (a dense and a comparatively loose) of the clumps. The comparison of stress-strain distribution for assemblies with varying particle shape demonstrates increasing volumetric strain (at any given stress level) as the particle shape changes from circular to higher aspect ratios. The differences of strength as a function of packing were also explored through simulation

and it was noticed that higher the packing, the stiffer the material assembly behavior due to higher coordination number of particles.

REFERENCES

1. Herrmann, H.J.; Hovi, J.-P.; and Luding, S., "*Physics of dry granular media",* Balkema, Dordrecht, 1998.
2. Wood, D.M., "*Soil behaviour and critical state soil mechanics",* Cambridge University, Cambridge, England, 1990.
3. Calvetti, F.; Combe, G.; and Lanier, J., *"Experimental micromechanical analysis of a 2D granular material: relation between structure evolution and loading path",* Mechanics of Cohesive-Frictional Materials, 1997, 2, 121–163.
4. Rothenburg, L. and Bathurst, R.J., *"Micromechanical features of granular assemblies with planar elliptical particles",* Geotechnique, 1992, 42(1), 79-95.
5. Ruistuen, H., *"An experimental and numerical study of mechanical behavior of weakly cemented reservoir sandstones through development of a micromechanical model",* PhD thesis, NTNU, Trondheim, 1997.
6. Preece, D.S.; Jesen, R.P.; Perkins E.D.; Williams, J.R., *"Sand production modeling using superquadratic discrete elements and coupling of fluid flow and particle motion",* In: Amadei B, et al., editors. Rock mechanics for industry. Rotterdam: Balkema, 1999, 161-167.
7. Cundall, P.A. and Strack, O.D.L., "*The development of constitutive laws for soil using the distinct element method",* Numerical methods in geomechanics, 1979, 1, 289-317.

8. Cundall, P.A. and Strack, O.D.L., "*A discrete numerical model for granular assemblies",* Geotechnique, 1979, 29**,** 47-65.

9. Cundall, P.A., "*Formation of a three-dimentional distinct element model-part I. A Scheme to detect and represent contacts in a system composed of many polyhedral blocks",* Int. J. Rock Mech. Min. Sci. Geomech Abstr, 1988, 25(3), 107-116.

10. Hart, R.; Cundall, P.A.; Lemos, J., "*Formulation of a three-dimentional distinct element model-Part II. Mechanical calculations for motion and interaction of a system composed of many polyhedral blocks",* Int. J. Rock Mech. Min. Sci. Geomech Abstr, 1988, 25(3), 117-125.

11. Itasca Consulting Group Inc. PFC2D (Particle flow code in 2 dimension), Version 3.1, Minneapolis, MN:, 2004.

12. Jason, T. D.; Christoph, G. G*., "Relation of initial specimen state and particle properties to the breakage potential of granular soils",* in 57th Canadian Geotechnical Conference; 5th Joint CGS/IAH-CNC Conference, Geo Quebec, 2004.

13. McDowell, G. R. and Bolton, M. D*., "On the micromechanics of crushable aggregates",* Geotechnique, 1998, 48, 667-679.

14. Nakata, Y.; Hyodo, M.; Hyde, A. F. L.; Kato, Y.; and Murata, H., *"Microscopic particle crushing of sand subjected to high pressure one-dimensional compression",* Soils and Foundations, 2001, 41(1), 69-82.

15. Nakata, Y.; Kato, Y.; Hyodo, M.; Hyde, A. F. L.; and Murata, H., *"One-dimensional compression behavior of uniformly graded sand related to single particle crushing strength",* Soils and Foundations, 2001, 41(2), 39-51.

16. Deresiewicz, H., "*Mechanics of granular material",* Adv. in Appl. mech., ed. Dryden, H.L.et al. Eds. New York: Academic Press Inc., 1958, 5, 233-306.

17. McGuire, W. and Gallagher, R. H., "*Matrix Structural Analysis",* New York: John Wiley & Sons, 1979.

18. Dutta, A.K. and Penumadu, D., *"Evaluation of particle level mechanical property changes due to induced stress in granular sand using nanoindentation",* J. of Material Research, in press.

19. Kanatani, K., *"A theory of contact force distribution in granular materials"*, Powder Technology, 1981, 28, 167-172.

PART 8: CONCLUSION AND FUTURE RESEARCH

CONCLUSION

The major goals of this study were: 1) to characterize the evolution of morphological features of granular materials subjected to one dimensional compression and 2) evaluate the effects of macroscopic stress on individual particle response by exploring the mechanical properties at particle scale using a novel technique of instrumented nanoindentation. Using different new techniques, particle crushing behavior in one dimensional compression under confined state was analyzed by pre and post test characterization of particle size and morphology at macro (> 75 μm) and micro (< 75 μm) particle length scales. Two types of silica sand (Ottawa sand and Q-Rok sand obtained from US Silica, Berkeley Springs, WV) having similar particle size, but different shape were used in this research to evaluate the role of initial particle morphology on the physical properties of its assemblage and its mechanical response.

In this study, the grain size distribution and shape characteristics were analyzed by various experimental procedures and techniques including Particle Shape Distribution Analyzer (PSDA), laser light scattering by Malvern Mastersizer-S, image processing through Flow Particle Imaging Analyzer (FPIA-2100), and using the traditional Sieve Analysis. Experimental results indicates that with applied intermediate and higher vertical stress, macro level sub-angular Q-Rok sand produces higher percentage of finer particle for all size ranges as compared to the sub-rounded Ottawa sand implying that Q-Rok sand undergoes more particle breakage relative to Ottawa sand due to a combined effect of particle morphology (namely particle asperities and angularity). In contrast to the particle breakage behavior at macro level, the analysis of the micro level particles

(particles smaller than approximately 75 microns) showed that Ottawa sand produces a higher volume fraction of finer particles compared to Q-Rok sand under similar imposed stress levels. The particle shape is suggested to be the principle governing factor that controls such particle breakage behavior for the two types of sand analyzed in this research.

This study proposed a new technique, depth sensing nanoindentation, which has emerged recently as a powerful tool for precise measurements of mechanical properties of materials and has the potential to play a significant role in elucidating the mechanisms associated with many particulate mechanics issues of relevance to geotechnical engineering. Using nanoindentation technique, an extensive study was performed to analyze the characteristics of the scale dependent mechanical properties such as hardness, modulus, and time dependent creep properties for both geomaterials and advanced composites. Application of this technique on blended nanocomposites prepared using a low-viscosity, liquid epoxy resin and purified single-wall carbon nanotubes (SWCNT) revealed a steady and modest increase of modulus and hardness as a function of SWCNT content. The variation in modulus and hardness as a function of indentation depth on SWCNT composites were also analyzed and the problem related to the contribution from nanotube to the failure tensile strength was justified. Plausible recommendations were made to improve the overall strength and modulus of the composite. The comparison of time dependent creep properties for these composite materials demonstrates noticeable variation of creep displacements with small changes in SWCNT content in the composite and established the viability of the instrumented indentation technique for measuring the

time-dependent mechanical properties of materials based on small sample volume. Creep exponents for these composites were also evaluated based on indentation strain rate versus hardness, which showed the beneficial effects of reduced creep deformation with increasing nanotube content.

Using depth sensing nanoindentation instrumentation technique, an attempt was made in this research to characterize the micromechanical properties including hardness, Young's modulus and time dependent creep parameters for individual granular sand particles. This study is the first of its kind to use nanoindentation technique to study mechanical properties of small particles individually. In addition, authors used nanoindentation technique in this research to evaluate the micromechanical property changes due to the applied stress for varying particle shape under confined conditions. Two types of silica sand (Ottawa sand and Q-Rok sand) having similar mineralogy and size (individual particles smaller than 1 mm) but very different morphology, were used for studying the particle level mechanical properties. Confined compression tests were performed on their assemblage, and selected particles were characterized to study the effects of confining stress level on particle-scale response. Appropriate experimental and interpretation procedures developed to obtain hardness, modulus, and time dependent creep properties though nanoindentation technique were also demonstrated in this study.

A key observation on comparative results of mean modulus and mean hardness with the depth of indentation for two types of silica sand particles at two stress levels (unstressed and at 100 MPa) revealed that the general trend of elastic modulus and

hardness values for Ottawa sand particles were higher than Q-Rok sand particles at a given stress level. In addition, it was also evident from the nanoindentation study that the mechanical response of those two types of materials changed due to the application of 100 MPa of vertical stress in 1-D compression. Under stressed conditions, the elastic modulus of Ottawa sand particles increased from their unstressed condition, whereas Q-Rok sand particles showed a decrease in modulus with applied stress.

In this study, the variations of particle level time-dependent creep behavior of the two types of silica sand were analyzed and the changes in stress exponents on unstressed and 100 MPa stressed particles (i.e. particles subjected to 100 MPa global stress in the assembly) were explored. The indentation creep strain was observed to be higher for Ottawa and Q-Rok particles at unstressed condition when compared to 100 MPa stressed condition. This suggests that induced stress affects the time dependent properties of granular materials and may have important implications to fault rupture and earthquake studies. Two different approaches, one using hardness based approach and the second procedure of using curve fitting method were explored in this work for evaluating the creep stress exponents of individual sand particles, and good agreement between the results were observed. The measured creep stress exponents for Ottawa sand particles showed very little changes in stress exponent values in its unstressed and stressed conditions. Whereas, noticeable increase in creep exponent for 100 MPa stressed Q-Rok particles was observed compared to unstressed particles implying that the effect of stress was much more pronounced for initially angular shaped Q-Rok particle when compared to well rounded Ottawa sand.

This study also demonstrated the application of a recently developed numerical analysis program (PFC^{2D}) which is based on Distinct Element Method (DEM) was used to evaluate the micromechanics associated with 1-D compression on granular particle assemblage with different particle shape and packing. The study also focused on the evolution of particle breakage behavior by validating experimental and simulated assembly of granular media subjected to one dimensional compression under confined state.

In the numerical analysis, actual particle level micro-properties were used for generating the model, where the contact stiffness of the particles used in the numerical simulations were directly obtained from the measured values of the elastic modulus of single particle through nanoindentation technique. Particles with different shape were generated using clump logic and the details of the algorithm developed for the study were described. The numerical results with laboratory data corresponding to 1-D compression tests on Ottawa sand for two initial porosity values were compared. The global stress required for the initiation of particle breakage and the corresponding maximum compressive contact force experienced by a particle in the assembly at a loose and dense state of packing were determined and could lead to improved understanding of yielding behavior for granular assembly using co-ordination number and individual particle contact force chain structure. The variation of stress-strain distribution with varying particle shape was simulated, and the differences of material strength in the assembly as a function of packing were also explored using PFC^{2D}.

FUTURE RESEARCH

In this research, several techniques/processes were used for the characterization of particles at macro and micro levels. Imaging based particle sizing technique were found to be effective for measuring two-dimensional particle size and shape information for particles larger than 1.5 μm in size. However, these techniques have drawbacks on the measurement of weight-based particle size distribution, which is often used as a reference and defining the three-dimensional shape information. Suitable procedures need to be developed that combine the particle size and shape information from 2-D digital image analysis and develop its relationship with standard weight based techniques for size information. In addition, advance particle shape characterization parameters (for example FFT based approach) should be implemented to have a better insight about the shape aspects of the particles.

In this study, the application of nanoindentation technique to evaluate particle level mechanical properties were performed by using the sand particles with particle diameter less than 1mm mounted within polymer matrix. Owing to the large differences in mechanical properties between the indenting sample (particle) and substrate (mounting material), substrate effect may be an important issue and needs further research for evaluating the mechanical properties for such type of smaller particles using nanoindentation. The verification of experimental accuracy and determination of area function coefficients for nanoindentation were made by applying the same procedures on the amorphous fused silica (standard material) of finite size. It would be interesting to perform a series of indentation tests on fused silica particles with varying shape and size

embedded within polymer matrix, and correlate the responses with the results obtained from indentation on fused silica of finite size.

Though particle level creep properties were analyzed, the quantitative creep effect of assemblies with varying packing states were not performed and this could be interesting future work that should be explored. Suitable procedures and analytical approaches should be developed to establish the particle level creep dependencies on the global creep behavior of the material assembly with a starting state of initial packing (void ratio). This could have a large impact in gaining insight about mechanisms associated with many geotechnical engineering situations where time dependent behavior of an assemblage of particles is still largely unresolved.

The numerical simulation of particle assembly through distinct element method does not allow the particle breakage and in this study the stress-strain behavior of the assemblies were analyzed considering the particles as elastic bodies. However, new subroutines can be developed using FISH code in PFC^{2D} to allow particle crushing and should be the focus of future research. This would help in developing theoretical particulate mechanics model for realistically modeling of complex issues such as the relationship between initial morphology, state of packing, particle properties, stress level, and time dependency.

Vita

Amal K. Dutta was born in Calcutta, India on January 2, 1965. He lived in Bankura, West Bengal where he attended both grade school and high school. He graduated with honors from Bankura Zilla School in June 1981. He joined the Jadavpur University ,Calcutta; a premier institute that ranked among the top five universities in India and earned his BS degree in Geology and MS degree in Applied Geology with a major in Geophysics. Upon completion of graduate studies he worked as professional Mining Geologist for over nine years with various multinational organizations like Indian Aluminium Company Limited (INDAL) and Hamco Mining and Smelting Limited (HAMCO). He entered the doctoral program in Civil Engineering at the University of Tennessee, Knoxville in August of 2001 and pursuing his research in Geotechnical Engineering. Amal is happily married to his wife Pampa from whom he got a lovely son Arpam. His research during the Ph.D program involved the mechanical property characterization of geometerials and composites using nanoindentation and modeling of granular material micromechanics using distinct element method. He officially received his doctoral degree in civil engineering in August, 2006.